


AFRL-AFOSR-UK-TR-2016-0014

# Development of Thermally Actuated, High-Temp Composite Morphing Concepts 140063

**Paul Weaver**
**THE UNIVERSITY OF BRISTOL**

**05/11/2016**
**Final Report**

**DISTRIBUTION A: Distribution approved for public release.**

Air Force Research Laboratory
AF Office Of Scientific Research (AFOSR)/ IOE
Arlington, Virginia 22203
Air Force Materiel Command

# REPORT DOCUMENTATION PAGE

Form Approved OMB No. 0704-0188

Public reporting burden for this collection of information is estimated to average 1 hour per response, including the time for reviewing instructions, searching existing data sources, gathering and maintaining the data needed, and completing and reviewing the collection of information. Send comments regarding this burden estimate or any other aspect of this collection of information, including suggestions for reducing the burden, to Department of Defense, Washington Headquarters Services, Directorate for Information Operations and Reports (0704-0188), 1215 Jefferson Davis Highway, Suite 1204, Arlington, VA 22202-4302. Respondents should be aware that notwithstanding any other provision of law, no person shall be subject to any penalty for failing to comply with a collection of information if it does not display a currently valid OMB control number.
**PLEASE DO NOT RETURN YOUR FORM TO THE ABOVE ADDRESS.**

| 1. REPORT DATE *(DD-MM-YYYY)* | 2. REPORT TYPE | 3. DATES COVERED *(From – To)* |
|---|---|---|
| 31 March 2016 | Final Report | 01 Feb 14 – 01 Feb 16 |

**4. TITLE AND SUBTITLE**

**Development of Thermally Actuated, High-Temperature Composite Morphing Concepts**

**5a. CONTRACT NUMBER**

**EOARD 14-0063**

**5b. GRANT NUMBER**

**FA9550-14-1-0063**

**5c. PROGRAM ELEMENT NUMBER**

61102F

**6. AUTHOR(S)**

Prof. Paul Weaver

**5d. PROJECT NUMBER**

**5d. TASK NUMBER**

**5e. WORK UNIT NUMBER**

**7. PERFORMING ORGANIZATION NAME(S) AND ADDRESS(ES)**

ACCIS
University of Bristol, United Kingdom M13 9PL
UK

**8. PERFORMING ORGANIZATION REPORT NUMBER**

N/A

**9. SPONSORING/MONITORING AGENCY NAME(S) AND ADDRESS(ES)**

EOARD
Unit 4515
APO AE 09421-4515

**10. SPONSOR/MONITOR'S ACRONYM(S)**

AFRL/AFOSR/IOE (EOARD)

**11. SPONSOR/MONITOR'S REPORT NUMBER(S)**

**12. DISTRIBUTION/AVAILABILITY STATEMENT**

**Distribution A: Approved for public release; distribution is unlimited.**

**13. SUPPLEMENTARY NOTES**

**14. ABSTRACT**

A thermal bimorph is a thin laminate which develops curvature upon heating on account of being constructed from layers of mismatched thermal expansion coefficients. However, current bimorphs are generally limited to benign temperatures and linear temperature displacement relationships. This work develops modelling techniques and fabrication methods that facilitate the use of nonlinear-response thermal bimorphs in high-temperature morphing structures. Successful application of this work may yield morphing hot structures in extreme environments. A particularly appealing set of applications exists in gas turbine engines, which stand to benefit greatly from aerodynamic control in their combustors, turbines, and nozzles. The overarching goal of this project wass to develop the techniques and understanding necessary to fabricate high-temperature, thermally actuated morphing structures that operate with a tailored, nonlinear response to temperature change; that is, actuators whose displacement can be either concentrated at a triggering temperature, or spread out over a given temperature range.

**15. SUBJECT TERMS**

EOARD, Materials, thermal management, vascular network

| 16. SECURITY CLASSIFICATION OF: | | | 17. LIMITATION OF ABSTRACT | 18, NUMBER OF PAGES | 19a. NAME OF RESPONSIBLE PERSON |
|---|---|---|---|---|---|
| a. REPORT | b. ABSTRACT | c. THIS PAGE | | | Matthew Snyder |
| UNCLAS | UNCLAS | UNCLAS | SAR | 103 | 19b. TELEPHONE NUMBER *(Include area code)* +44 (0)1895 616420 |

# EOARD/AFOSR Final Report

Grant Number: FA9550-14-1-0063

Research Title: Development of Thermally Actuated, High-Temperature Composite Morphing Concepts

Reporting Period: 01 February 2014 - 01 February 2016

Principle Investigator: Paul Weaver, University of Bristol, Queen's Building, Bristol, BS8 1TR, United Kingdom

31st March 2016



**Distribution A: Approved for public release; distribution unlimited.**

# Contents

**1 Introduction** **11**

1.1 Overview . . . . . 11

1.2 Problem and Motivation . . . . . 11

**2 Composite Bimorph Development** **15**

2.1 A Bimorph's Maximum Blocked Moment . . . . . 15

2.2 The Material Performance Index . . . . . 17

2.3 Hybrid CFRP/Aluminium Laminates: Manufacture and Test . . . . . 20

2.4 Hybrid Bimorphs using Angle-Ply Laminates . . . . . 23

2.4.1 Theoretical Performance . . . . . 23

2.4.2 Manufacturing Considerations . . . . . 26

**3 Multistability Modelling Development** **27**

3.1 Mechanics . . . . . 28

3.1.1 Achieving Snap-Through Behaviour by Exploiting the Geometrically Nonlinear Flexural Response of Thin, Initially Curved Shells . . . . . 28

3.2 Modelling Methodology . . . . . 32

3.2.1 Description of Thermal Curvature . . . . . 33

3.2.2 Model Development . . . . . 34

3.3 Experimental Verification of Model . . . . . 35

3.3.1 Fabrication of Hybrid Laminate Shell and Strip Specimens . . . . . 35

3.3.2 Measurement of Thermal Curvatures and Snap-Through Behaviour of Hybrid Laminate Shells . . . . . 38

3.4 Modelling Results and Discussion . . . . . 39

3.4.1 Experimental Measurements of Thermal Curvature . . . . . 39

3.4.2 Model Predictions Regarding the Influence of Initial Curvature . . . 40

3.4.3 Model Predictions of the Laminate's Response to Thermal Loads . . 43



**Distribution A: Approved for public release; distribution unlimited.**

3.4.4 Experimental Results . . . . . 44
3.4.5 Comparison of model predictions with experimental results . . . . . 45
3.4.6 Observations Regarding Stability Near Snap-Through Temperatures . 46

**4 Thermally Driven Morphing With High-Temperature Composites 47**

4.1 Metal Matrix Composites: Materials and Processing . . . . . 48
4.1.1 MMC-Ti Bimorphs . . . . . 49
4.1.2 MMC-304SS Bimorphs . . . . . 52
4.2 Ceramic Matrix Composites: Materials and Processing . . . . . 55
4.2.1 Ceramic Matrix Composite Manufacturing at The University of Bristol 55
4.2.2 CMC-Metallic Bimorph Joining at NASA Glenn Research Centre . . 65
4.2.3 CMC-Metallic Flap Section . . . . . 68
4.3 Experimental Procedures . . . . . 70
4.3.1 Results and Discussion . . . . . 74
4.3.2 MMC-Ti Bimorphs . . . . . 74
4.3.3 MMC-304SS Bimorphs . . . . . 77
4.3.4 CMC-Metallic Flap Section . . . . . 79

**5 Outcomes 83**

5.1 Outcome 1: Improved Modelling of the Nonlinear Thermostructural Response of Composite Bimorph Shells . . . . . 83
5.2 Outcome 2: Demonstrate Thermally Driven Snap-Through With a Composite Bimorph . . . . . 84
5.3 Outcome 3: Develop and Demonstrate Composite Bimorphs Suitable for High-Temperature Use . . . . . 85

**6 Impact 87**

6.1 Impact of Modelling Developments . . . . . 87
6.2 Impact of Snap-Action Bimorph Development . . . . . 87
6.3 Impact of High-Temperature Bimorphs . . . . . 89



**Distribution A: Approved for public release; distribution unlimited.**

**7 Future Research Opportunities** **91**

7.1 Collapsible Stiffeners for Lockable Morphing Structures . . . . . 92

7.2 Geometrically Linear Behaviour For Arbitrary Planforms Despite Large Displacements . . . . . 93

7.3 Beyond Bimorphs: More Efficient Thermal Morphing Structures . . . . . 95

**8 Dissemination** **97**



**Distribution A: Approved for public release; distribution unlimited.**

# List of Figures


1 The mechanism approach towards variable geometry gas turbine components. 12

2 Flexure usage in turbine engines. . . . . 12

3 Weight-specific performance of various actuation techniques. . . . . 13

4 Potential gas-turbine applications of thermally driven morphing structures. 14

5 Thickness-specific bimorph material performance indices for the pairs of candidate materials listed in Table 1. . . . . 18

6 Weight-specific bimorph material performance indices for the pairs of materials listed in Table. 1. . . . . 19

7 The CFRP/5251Al chevron-shaped laminate mounted in the dial-gauge test fixture. . . . . 21

8 Tip displacement results for the CFRP/5251Al chevron-shaped laminate. . . 22

9 A time-lapse image sequence of the CFRP/5151Al chevron-shaped laminate cooling from 160°C to 50°C. . . . . 23

10 A sketch of a hybrid bimorph using an angle ply laminate as the low-expansion layer. . . . . 24

11 Principle thermal expansion coefficients of a homogenised angle-ply CFRP laminate. . . . . 24

12 Principle moduli of a homogenised angle-ply laminate. . . . . 25

13 Weight specific bimorph performance index of a CFRP/Al laminate. . . . . 26

14 A 2x2 twill woven fabric sheared to $[\pm 23_{wv}]$, and the same fabric in its unsheared configuration, $[\pm 45^{\circ}_{wv}]$. . . . . 27

15 Response of curved shell to applied internal bending moment perpendicular to initial curvature direction. . . . . 29

16 A bistability phase diagram for three classes of bimorph laminates. . . . . 31

17 Hybrid laminate specimens cured upon a flat tool. . . . . 36

18 Hybrid laminate oven test setup. . . . . 39

19 Experimentally measured thermal curvatures of the strip specimens described in Table 3. . . . . 40




**Distribution A: Approved for public release; distribution unlimited.**

20 Phase diagram showing combinations of thermal curvatures $\kappa_{\mathrm{T}x}$ and $\kappa_{\mathrm{T}y}$, and initial curvatures $\hat{\kappa}_y$ which yield bistable behaviour. . . . . 42
21 Analytical results showing predicted effect of initial curvature upon hybrid laminate response to thermal loading. . . . . 43
22 Experimental results of shell curvatures compared to model predictions. . . . 46
23 Manufacturing process used to create the MMC-Ti and MMC-304SS bimorphs. 50
24 Metal matrix composite bimorph laminate as it emerged from the HIP process and after wire-EDM cutting. . . . . 51
25 False-colour SEM micrograph of MMC-Ti laminate cross-section. . . . . 51
26 Partial debond of the MMC-304SS interface. . . . . 53
27 False-colour SEM micrograph of MMC-304SS laminate cross-section. . . . . 54
28 SEM micrograph and overlaid EDX K-shell emission densities of the MMC-304SS interface. . . . . 55
29 The polymer infiltration and pyrolysis process. . . . . 56
30 SEM imagery of PyC-coated carbon fibres. . . . . 57
31 Dry carbon NCF fabric in the post-heat-treated state. . . . . 58
32 Three fabrics with progressively greater weave bias. . . . . 59
33 The wet lay-up workspace. . . . . 59
34 Laminates stacked using ceramic separators and 310 stainless steel plates. . . 61
35 The polymer reinfiltration procedure. . . . . 63
36 C/SiC panels immediately after pyrolysis and removal of SiC particulate matter. 64
37 Stress-strain curve obtained by 3-point flexural testing of C/SiC composite with PyC-coated fibres. . . . . 65
38 The braze application process. . . . . 66
39 SEM micrograph of C/SiC CMC and Incoloy 800H joined with a fully wetted brazed interface. . . . . 67
40 Photograph of debonded braze interface and successfully joined laminate. . . 68
41 Drawing of the flap section thermal actuator concept. . . . . 69
42 MMC bimorph and CMC-metallic flap-section test articles mounted on the test fixture. . . . . 70



**Distribution A: Approved for public release; distribution unlimited.**

43 Experimental setup showing optical tracking and thermal cameras positioned in front of furnace. . . . . 72
44 Thermal imagery data showing several MMC bimorph and CMC-metallic flap section thermal morphing test articles. . . . . 73
45 Thermally induced curvature of MMC-Ti bimorphs. Solid lines link data points measured during heating, dotted lines link cooling data points. . . . 74
46 Thermally induced curvature of MMC-304SS bimorphs. Solid lines link data points measured during heating, dotted lines link cooling data points. . . . 78
47 Thermally induced tip displacement of CMC-metallic flap section. . . . . 81
48 CMC-metallic flap section at $\sim 1000°C$. . . . . 82
49 The camera and experimenter's view of the furnace at roughly 1000°C. . . . 82
50 Fan and core exhaust chevrons present opportunities for thermally driven morphing structures. . . . . 88
51 Bistable reeled composite in partially deployed state. . . . . 89
52 Turbine stator nozzle morphing. . . . . 90
53 Collapsible stiffeners joined to a skin. . . . . 93
54 Methods of achieving a linear curvature response to internal moments for both developable and doubly curved surfaces. . . . . 95
55 Advanced thermal morphing laminate concepts. . . . . 96

# List of Tables

1 Candidate material pairs for bimorph actuators. . . . . 17
2 Manufacturing specifications for a chevron-shaped hybrid laminate. . . . . 21
3 Test article manufacturing parameters for hybrid fibre-metal laminates. . . 37
4 Thermoelastic material data for AS7/M21 UD composite and 5251 aluminium alloy. . . . . 37
5 Thermoelastic material properties for the MMC-Ti and MMC-304SS bimorphs. 49
6 Manufacturing specifications for MMC bimorphs. . . . . 52
7 Pyrolysis temperature schedule. . . . . 62



**Distribution A: Approved for public release; distribution unlimited.**

8 Nominal sample dimensions for 3-point bend tests. . . . . 64
9 Thermoelastic material properties for the composites and metals used in the morphing flap section. . . . . 69
10 Manufacturing specifications for CMC-metallic flap sections. . . . . 70

# List of Symbols, Abbreviations, and Acronyms

| Symbol(s) | Respective Definition(s) |
|---|---|
| $M_{\mathrm{T}i}$ | Laminate thermal moments |
| $Q_{ij}$, $\overline{Q}_{ij}$ | Lamina constitutive constants in ply and laminate coordinate systems |
| $A_{ij}$, $B_{ij}$, $D_{ij}$ | Laminate constitutive constants |
| $\epsilon_i$, $\epsilon_{\mathrm{M}i}$, $\epsilon_{\mathrm{T}i}$ | Total, mechanical, and thermally induced strain components |
| $\sigma_i$, $\sigma_{\mathrm{T}i}$ | Mechanical and thermal stress components |
| $\kappa_i$ , $\hat{\kappa}_i$, $\hat{\kappa}_{\mathrm{T}i}$ | Current, initial, and thermally induced curvature components |
| $\boldsymbol{\epsilon}^0$ | Midplane strain vector |
| $\Delta\boldsymbol{\kappa}$ | Curvature change vector |
| $h$, $L_x$, $L_y$ | Laminate thickness and length in $x$ and $y$ directions |
| $\Pi$ | Total potential energy |
| $\alpha_i$ | Thermal expansion coefficient components |
| $T$, $T_0$, $T_{ref}$ | Current, initial, and reference temperatures of a laminate sublayer |
| $\xi$ | Optimum ratio of bimorph layer thickness for maximum thermal moment |
| $P_{\mathrm{h}}$ | Thickness-specific bimorph material performance index |
| $P_{\mathrm{w}}$ | Weight-specific bimorph material performance index |
| $V_{\mathrm{f}}$ | Fibre volume fraction |
| AHPCS | Allyl hydrido polycarbosilane polymer |
| CLT | Classical laminate theory |
| C/SiC | Carbon fibre, silicon carbide matrix |
| CTE | Thermal expansion coefficient |
| HIP | Hot isostatic press |
| MMC-Ti | Bimorph with MMC and titanium layers |
| MMC-304SS | Bimorph with MMC and 304 stainless steel layers |
| PIP | Polymer infiltration and pyrolysis |
| PMC, MMC, CMC | Polymer matrix, metal matrix, and ceramic matrix composite |
| PyC | Pyrolytic carbon |



**Distribution A: Approved for public release; distribution unlimited.**

# Foreword

This report catalogs the research outputs of work performed under EOARD grant number FA9550-14-1-0063, spanning Feb. 2014 - Feb. 2016. This work carries on from prior EOARD grant, FA8655-11-1-3063, which ran Oct. 2011 - Oct 2013. The collected outputs of both grants are contained in the PhD thesis given in Section 8

# Abstract


### Background

A thermal bimorph is a thin laminate which develops curvature upon heating on account of being constructed from layers of mismatched thermal expansion coefficients. However, current bimorphs are generally limited to benign temperatures and linear temperature-displacement relationships. This work develops modelling techniques and fabrication methods that facilitate the use of nonlinear-response thermal bimorphs in high-temperature morphing structures. Successful application of this work may yield morphing hot structures in extreme environments. A particularly appealing set of applications exists in gas turbine engines, which stand to benefit greatly from aerodynamic control in their combustors, turbines, and nozzles.

### Objectives

The overarching goal of this project is to develop the techniques and understanding necessary to fabricate high-temperature, thermally actuated morphing structures that operate with a tailored, nonlinear response to temperature change; that is, actuators whose displacement can be either concentrated at a triggering temperature, or spread out over a given temperature range. This main goal can be broken up into components as follows:

1. Extend prior multistability models to better predict the response of initially curved fiber-metal laminates. Extract insight from these models to create design rules useful to future engineers.




**Distribution A: Approved for public release; distribution unlimited.**

2. Design, manufacture, and test novel methods of thermal actuation. This effort will mostly focus on the development of the fiber-metal laminate concept.

3. Develop methods of achieving high-temperature thermal actuation. Essentially, this involves using our fundamental knowledge of thermal morphing to implement our concepts with high-temperature materials systems, such as MMCs, CMCs, and high-temperature alloys.

### Modelling Approach and Results

Existing analytical equations used to predict the optimum thermal moment performance of isotropic thermal bimorphs have been adapted for composite materials. These equations are used to show that the weight-specific thermal moment of certain composite thermal bimorphs can exceed that of today's metallic bimorphs by a factor of 15.

Improvements have been made to prior shell multistability models, which allow for the accurate prediction of snap-through behavior of thermal bimorph shells. The main modelling advance is to specify input loads in terms of thermally induced curvatures, rather than thermal moments as is the classical approach. These curvatures are experimentally measured using beam specimens. Separate measurement of $x$, $y$, and twist curvatures of these simple 1D structures are combined to predict the behavior of more complex 2D shells. This method essentially amounts to measuring the laminate material's thermal expansion properties flexurally, rather than axially as is the norm. The chief advantage is that manufacturing-induced pre-strains such as resin cure shrinkage are automatically accounted for, which we found to be critical for accurate prediction of the thermomechanical response of multistable shells.

### Experimental Approach and Results

CFRP-Aluminium hybrid laminate shells have been fabricated which have successfully demonstrated snap-through behavior purely driven by temperature change. To our knowledge, this is the first instance of such behavior occurring without the assistance of boundary conditions (e.g. prestressed beams as used in circuit breakers). Shell curvatures were measured between 20-180°C using digital image correlation. The results compare well with modelling predictions.

High-temperature bimorphs have been fabricated from metal matrix and ceramic matrix composites. The metal matrix composite bimorphs were manufactured with existing fabrication methods and were found to exhibit repeatable thermal responses up to roughly 500°C. Ceramic matrix composites presented manufacturing challenges, however efforts eventually



**Distribution A: Approved for public release; distribution unlimited.**

yielded a bimorph-like device which showed elastic thermal responses at temperatures up to 600°C. Thermal actuation at temperatures in excess of 1000°C was demonstrated, albeit associated with a departure from elastic material behaviour.

# 1 Introduction

## 1.1 Overview

The drive for improved air and space vehicle capability has been punctuated by investigations into complex, active control systems based on smart material actuators such as piezoelectrics and shape memory alloys. However, for situations where a desired shape or actuation command correlates to structural temperature, a powerful, yet relatively simple alternative is proposed. Operating in a passive manner, thermally-driven structures exploit differential thermal expansion to drive structural morphing. Thermally driven structures are characterized by their ability to exhibit a shape change in response to thermal loading. We focus on the bimorph concept, whereby two or more constituent materials of mismatched coefficient of thermal expansion (CTE) are joined in a laminate such that each material's thermally induced tensile and compressive stresses act remote from the neutral axis, thus generating bending moments, usually in a biaxial manner. This behaviour is observed in the common bimetallic strip, and has found applications in thermostats, circuit breakers, and spacecraft passive thermal management systems.

## 1.2 Problem and Motivation

Variable geometry structures have been identified as a technology which can enable performance improvements in gas turbine aero-propulsion applications [1, 2]. Conventionally, variable geometry has been achieved using electromechanical or hydraulic linear actuators acting upon mechanisms of linkages, bearings, and hinges. Examples of such include variable geometry inlet guide vanes and afterburner exhaust nozzles, as shown in Fig. 1. This conventional approach has so far been restricted to applications outside the engine combustor and turbine sections on account of the challenges presented by such a hot and corrosive environment. In particular, variable geometry mechanisms are challenged by large temperature excursions, which present difficulties in maintaining close tolerances while avoiding seizure or galling. Meanwhile, current hydraulic and servo-electric actuators are limited to roughly 200°C ambient temperature [3], and thus restricted to locations outside the engine core.



**Distribution A: Approved for public release; distribution unlimited.**



Figure 1: Two examples of the mechanism approach towards variable geometry gas turbine components. Pratt & Whitney F100 variable exhaust nozzle (left), and Pratt & Whitney J58 variable inlet guide vane (right, silver blade), which pivots aft of the black-coloured static guide vane. Images after [4] and [5].

Morphing structures may present a viable alternative to the conventional mechanism-based strategies. A flexural hinge, for example, is free from the lubrication requirements of a conventional hinge, does not develop free-play, nor is susceptible to thermally or chemically induced seizure. In addition, the smooth-deformation nature of morphing structures is generally more advantageous than rigid body rotations or displacements for applications in aerodynamic surfaces. In fact, flexures are already common features on gas turbine engines. Figure 2 shows a number of hot-section structures which are designed to accommodate differential thermal expansion via flexural displacement.

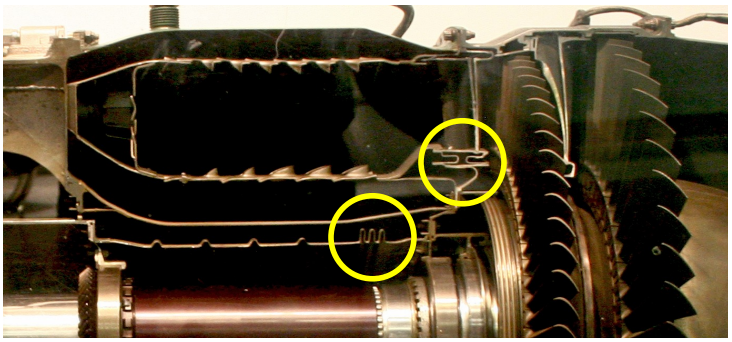


Figure 2: This J85 turbojet uses a number of flexure elements, highlighted by yellow circles, which are designed to accommodate differential thermal expansion between components. Image from [6].



**Distribution A: Approved for public release; distribution unlimited.**

A morphing-based strategy may also allow mechanically simple solutions to the high-temperature actuation problem. Strain-based actuation concepts such as shape memory alloys (SMAs), piezoelectrics, and thermal-expansion driven systems present the opportunity to combine actuator and structure into one, a trait which may be particularly beneficial in applications where packaging of traditional actuation systems would be impractical. This feature is well exemplified by active turbine tip clearance control, a thermal expansion-based technology employed on most modern civil turbofans [7]. While much progress has been made towards improving the high-temperature properties of SMAs and piezoelectrics, this study focuses on evaluating the feasibility and flexural performance of thermal expansion systems. Given a sufficient temperature change, these sorts of systems are competitive with SMAs in terms of specific actuation performance, as shown in Fig. 3.

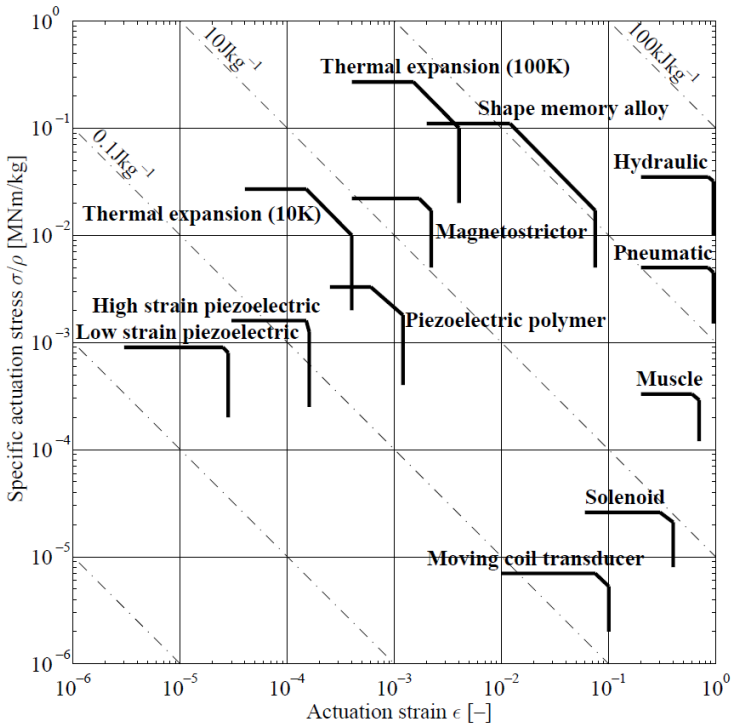



Figure 3: The weight-specific performance of various actuation techniques. From Huber *et al.* (1997) [8].

Some examples of potential thermal morphing applications in gas turbine engines are given in Fig. 4. As long as the desired shape of combustor, nozzle vane, etc. at each operating condition can be correlated to a unique gas temperature at that condition, a thermal



**Distribution A: Approved for public release; distribution unlimited.**

morphing structure can adapt its shape in a purely passive manner. Specific applications may include variable control of cooling flow, combustor dilution, nozzle vane geometry, and core exhaust chevron geometry. For most of these applications, the displacements induced by thermal strains must be amplified by some means, such that they are large enough to serve some practical purpose. This problem is approached using the bimorph concept, and is discussed in the following section.

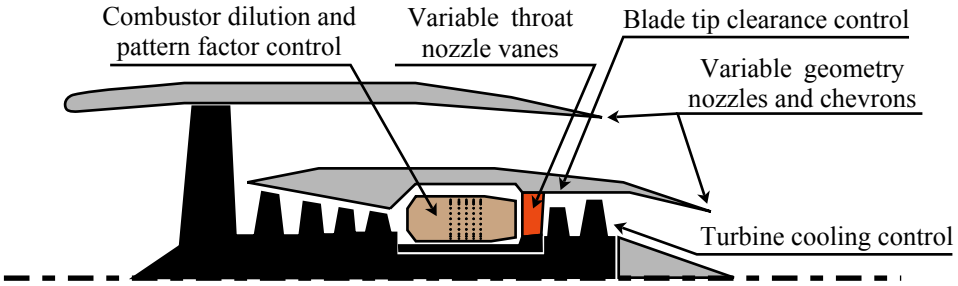



Figure 4: Potential gas-turbine applications of thermally driven morphing structures.

Conventional bimorphs, such as the common bimetal strip, are constructed from isotropic materials. This feature limits the acceptable range of bimorph geometries available to the designer, a problem which may be overcome through the use of composite materials. Mansfield [9] has shown that because the bending stiffnesses and thermal moments are equal in all directions for an isotropic plate, the energetically preferable direction of bending is determined instead by the plate's geometry and boundary conditions, with curvature preferring to develop along the major axis of free elliptical plates, for example. Analogous results have been found for rectangular planforms [10]. Bending deformation perpendicular to a laminate's long axis, such as that required for a trailing edge airfoil control surface, would be untenable without the use of directional stiffening mechanisms such as stringers or corrugations. The use of composite materials opens the possibility to create thermal bimorphs which are anisotropic in terms of both stiffness and thermal moments. As a result, this work has developed bimorph actuators which exhibit bending action in a direction determined by material orientations, thus allowing the designer freedom to specify general planform geometries.

Free-standing thermal bimorph beams exhibit approximately linear bending response to temperature change, yet for many applications, the designer may instead want to specify a highly nonlinear response, such as displacement concentrated within a temperature window, or perhaps even a step-change response. This behavior is currently achievable with isotropic bimorphs using various permutations of either the end-constrained beam [11] or shallow



**Distribution A: Approved for public release; distribution unlimited.**

dome approaches [12]. However, the limited geometrical design space restricts them from general actuation and morphing applications, particularly where the actuator skin is to be employed as an aerodynamic surface. While shape memory alloys may be employed to give nonlinear displacement response to thermal loading, this project has demonstrated that the geometrically nonlinear response of thin shells subject to bending loads may be exploited to induce a nonlinear response to temperature change. This sort of behavior includes near-step-change responses, as well as snap-through, quasi-hysteretic, and multistable behavior. Because these nonlinear features owe themselves to geometric nonlinearity (as opposed to material nonlinearity), the designer is free to construct them from conventional engineering materials, particularly those with favorable properties such as high specific modulus and high-temperature durability.

# 2 Composite Bimorph Development

Timoshenko's seminal analysis of bimorphs [11] showed that maximum thermal moment was achieved by maximizing both the CTE mismatch between layers, as well as the modulus of each layer. Modern bimetals are made from austenitic stainless steel joined to Invar, a low-expansion iron-nickel alloy. Although the CTE mismatch and modulus of these materials compares favourably with most conceivable pairs, they are very dense, both roughly $8\,\mathrm{g/cm^3}$. On the other hand, the CFRP $[0_n/90_n]$ unsymmetric laminates that formed the basis of multistability research (see for example, [13]) have relatively low density and high CTE mismatch. Unfortunately, that material's $E_2$ is relatively low, on the order of one tenth that of engineering alloys. As a result, CFRP generates relatively weak thermal stresses in the $90^\circ$ direction. With these competing factors, a formal analysis is needed in order to assess which material pairs generate the highest weight-specific thermal moment.

## 2.1 A Bimorph's Maximum Blocked Moment

In order to sort out which pairs of materials yield the maximum weight-specific thermal moment, this work builds upon results obtained by Prasanna and Spearing [14], who found closed form solutions for the maximum blocked moment that can be achieved from a given pair of materials. Their work was directed at micro-electromechanical applications, and therefore does not appear to have received much attention in composite structures publications, however the cleverness of their approach should not go unmentioned. Early and contemporary works approached this optimisation problem by assuming a fixed ratio of layer thicknesses, and finding an expression for moment or curvature in terms of each layer's material properties. The resulting expressions were very complex, but this complexity turns



**Distribution A: Approved for public release; distribution unlimited.**

out to be due to the fact that these works overconstrained their optimization. Prasanna and Spearing found that if the ratio of layer thicknesses was not held fixed, but rather allowed to take on the optimum ratio for achieving maximum blocked moment, the resulting expression for blocked moment reduced to a remarkably simple expression.

Their solutions were found in terms of blocked moment, $M_{\text{blk}}$, which is the internal mechanical moment developed when a bimorph is restrained flat along the direction of interest while subject to a temperature change. In other words, if we wished to determine $M_{\text{blk}}$ in the $x$-direction, then we set $\kappa_x = 0$, but allow all other membrane strains and bending curvatures to remain unconstrained. The mechanical moment which is developed in reaction to the constraint is $M_{\text{blk}}$. This approach eliminates all Poisson coupling terms from the resulting solutions, contributing to their simplicity.

Their solutions were developed for isotropic-layered bimorphs, however they still hold true for composite-layered bimorphs as long as we assume that the material properties are taken to be those of the direction in question. In other words, if we wish to find the $M_{\text{blk}}$ in the $x$-direction, then we take $E = E_x$ for example. This shortcut is only allowable due to the approach described in the preceding paragraph. If we also constrained $\kappa_y, \kappa_{xy} = 0$, a much more complex CLT-based approach would be necessary. That said, for materials with $\nu \approx 0.3$, the resulting $M_{\text{blk}}$ would diverge by no more than roughly 10%, as $1/\left(1-\nu^2\right) \approx 1.10$.

Prasanna and Spearing found that the ratio of layer thicknesses that maximises $M_{\text{blk}}$ is given by

$$\xi = \frac{h_{\text{b}}}{h_{\text{t}}} = \sqrt{\frac{E_{\text{t}}}{E_{\text{b}}}}, \tag{1}$$

where $h_{\text{b}}$ and $h_{\text{t}}$ are the respective bottom and top layer thicknesses, while $E_{\text{b}}$ and $E_{\text{t}}$ are the respective bottom and top layer moduli.

Prasanna and Spearing's solution for maximum $M_{\text{blk}}$ attainable from a laminate of total thickness $h$ is simply

$$M_{\max} = h^2 \Delta T \left[\frac{E_{\text{b}}(\alpha_{\text{b}} - \alpha_{\text{t}})}{2\left(1 + 1/\xi\right)^2}\right], \tag{2}$$

where $\alpha_{\text{b}}$ and $\alpha_{\text{t}}$ are the respective bottom and top layer CTEs. Eq. (2) shows that $M_{\max}$ scales proportional to the CTE mismatch, in agreement with the result found by Timoshenko [11]. Perhaps the true value of this equation is to show, via Eq. (1), that $M_{\max}$ is penalised whenever $E_{\text{b}}/E_{\text{t}} \neq 1$. In other words, the bottom and top layers should be matched in terms of modulus, and consequently thickness, in order to maximise $M_{\max}$. Clearly, this objective is missed by $[0_n/90_m]$-type laminates, where for CFRP construction,



**Distribution A: Approved for public release; distribution unlimited.**

$E_b/E_t \approx 14$.[1] A CFRP/aluminium laminate would have a much improved $E_b/E_t \approx 1.9$ in the fibre direction, while a CFRP/stainless steel laminate would feature an even more impressive $E_b/E_t \approx 0.7$ in the fibre direction.

## 2.2 The Material Performance Index

In the preceding section, $M_{max}$ varied in proportion to the material constants in brackets. Separating out this term, we arrive at the thickness-specific bimorph material performance index:

$$P_h = \frac{E_b(\alpha_b - \alpha_t)}{2\,(1 + 1/\xi)^2}. \tag{3}$$

The subscript h denotes that $P_h$ is a thickness-specific performance index, as opposed to weight, cost, or any number of other parameters we could normalise against. Various candidate pairs of bimorph materials are listed in Table. 1, along with the typical bimetal arrangement of Invar/stainless steel. Using this data as input into Eq. (3), the thickness-specific material performance indices of these materials are shown in Fig. 5. The results from this section suggest that the performance of the common Invar/304SS bimetal is surpassed only by a CFRP/304SS laminate.

Table 1: Candidate material pairs for bimorph actuators. All properties given at room temperature.

| Bottom Layer (Low Exp.) | Top Layer (High Exp.) | $E_b$ [GPa] | $E_t$ [GPa] | $\alpha_b$ $[\frac{10^{-6}}{°C}]$ | $\alpha_t$ $[\frac{10^{-6}}{°C}]$ | $\rho_b$ [g/cm$^3$] | $\rho_t$ [g/cm$^3$] | $\xi = \frac{h_b}{h_t}$ [-] |
|---|---|---|---|---|---|---|---|---|
| Invar | 304 Stainless Steel | 141 | 195 | 1.0 | 17.1 | 8.1 | 8.0 | 1.176 |
| IM CFRP, 0° | IM CFRP, 90° | 130 | 9 | 0.0 | 30.0 | 1.6 | 1.6 | 0.263 |
| IM CFRP, 0° | 6061 Al * | 130 | 70 | 0.0 | 24.0 | 1.6 | 2.8 | 0.734 |
| IM CFRP, 0° | 304 Stainless Steel | 130 | 195 | 0.0 | 17.1 | 1.6 | 8.0 | 1.225 |
| IM CFRP, 0° | Ti-6Al-4V | 130 | 113 | 0.0 | 9.0 | 1.6 | 4.4 | 0.932 |
| IM CFRP, 0° | 8090 Al-Li | 130 | 77 | 0.0 | 21.4 | 1.6 | 2.5 | 0.770 |
| IM CFRP, 0° | AZ31 Mg * | 130 | 45 | 0.0 | 26.0 | 1.6 | 1.8 | 0.588 |

* These properties apply to most other aluminium and magnesium alloys, respectively.

[1] Recall that $E_b$ and $E_t$ are taken in the $x$ direction, so for $[0_n/90_m]$-type laminates, $E_b = E_1$ and $E_t = E_2$.



**Distribution A: Approved for public release; distribution unlimited.**

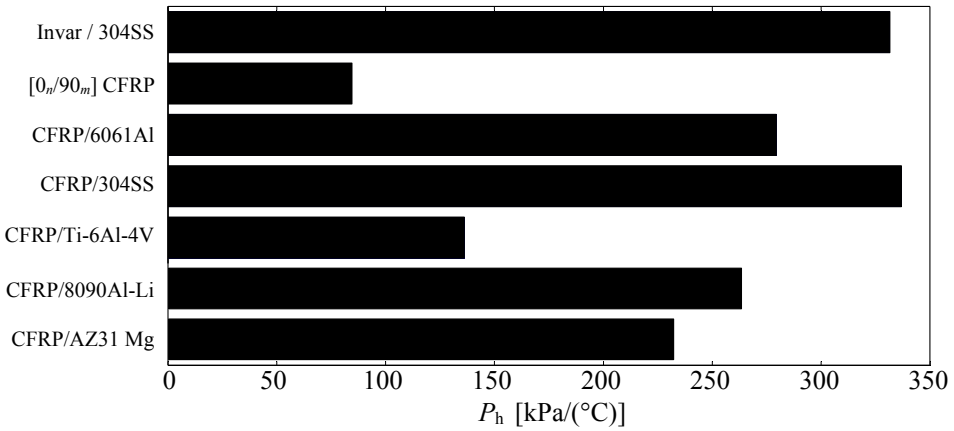



Figure 5: Thickness-specific bimorph material performance indices for the pairs of candidate materials listed in Table 1.

Yet, there remains the unsettled matter of the laminate's weight. After all, a less dense material could be made thicker for the same weight, and since $M_{\max}$ scales with $h^2$, the improvement in $M_{\max}$ would be relatively large. Because of this quadratic scaling, we must turn to Ashby's work in materials selection using performance indices [15]. The procedure for generating a weight-specific performance index is to find a geometrical parameter common to both the laminate's weight and $M_{\max}$, and use this common parameter to write $M_{\max}$ in terms of material density. In this case, the common geometrical parameter is the total thickness $h$. The areal density $w'$ of the laminate is

$$w' = \rho_{\text{avg}} h, \tag{4}$$

where $\rho_{\text{avg}}$ is the average density of the laminate, and is found by a weighted average of the bottom and top layer densities, $\rho_{\text{b}}$ and $\rho_{\text{t}}$, respectively:

$$\rho_{\text{avg}} = \frac{\rho_{\text{b}}\xi + \rho_{\text{t}}}{\xi + 1}. \tag{5}$$

Solving Eq. (4) for $h$ and substituting the result into Eq. (2) gives

$$M_{\max} = \frac{\Delta T}{\rho_{\text{avg}}^2}\left[\frac{E_{\text{b}}(\alpha_{\text{b}} - \alpha_{\text{t}})}{2\left(1 + 1/\xi\right)^2}\right]. \tag{6}$$

Thus, our weight-specific material performance index for a given pair of materials is found by factoring off $\Delta T$, yielding

$$P_{\text{w}} = \frac{1}{\rho_{\text{avg}}^2}\left[\frac{E_{\text{b}}(\alpha_{\text{b}} - \alpha_{\text{t}})}{2\left(1 + 1/\xi\right)^2}\right]. \tag{7}$$



**Distribution A: Approved for public release; distribution unlimited.**

From this equation, we can see that $P_{\mathrm{w}}$ is more sensitive to density than modulus or CTE mismatch. In other words, it is preferable to select less dense materials, even if there is a reasonable penalty to be paid in terms of modulus and/or CTE mismatch. This hypothesis is confirmed upon plotting $P_{\mathrm{w}}$ for the candidate materials, see Fig. 6. Here, we can plainly see that the high density of the Invar/304SS laminate has made it completely uncompetitive when weight is factored in. Perhaps surprisingly, the $[0_n/90_m]$ CFRP laminate exceeds the performance of two other hybrid fibre-metal laminates, mostly on account of its relatively low density. That said, experimental experience with such $[0_n/90_m]$ laminates shows that despite their impressive $P_{\mathrm{w}}$, their limited flexural strength and self-destructive manufacturing tendencies disqualify them from serious consideration.

The standout performer is the CFRP/AZ31 magnesium alloy laminate. This material combination exceeds the $P_{\mathrm{w}}$ of CFRP/304SS by a factor of 4.7, while the commonly used bimetal of Invar/304SS is outperformed by a factor of 15.4. The advantages of this pairing do not stop with a superior $P_{\mathrm{w}}$. Because the $\alpha$ of AZ31 is closely matched to the $\alpha_2$ of CFRP, deleterious tensile stresses in the composite's 90° direction are minimised.

Unfortunately, magnesium alloys are difficult to safely machine, have limited formability, and are expensive to source. For the purposes of this work, it was not necessary to choose the absolute optimum-performing material at all costs, financial or otherwise. As a result, CFRP/aluminium bimorphs were chosen for further study instead. This material system is also nearly CTE-matched in the 90° direction, and thus shares the aforementioned advantages of CFRP/magnesium bimorphs while being superior in terms of cost and schedule risk for the purposes of this research.

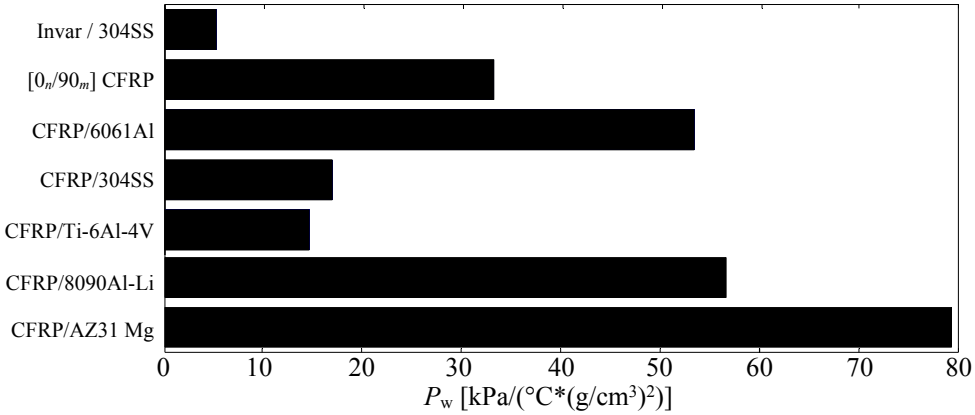



Figure 6: Weight-specific bimorph material performance indices for the pairs of materials listed in Table. 1.



**Distribution A: Approved for public release; distribution unlimited.**

## 2.3 Hybrid CFRP/Aluminium Laminates: Manufacture and Test

Although hybrid laminates were forecast to show excellent performance as bimorphs, the question of whether they could be manufactured remained open. Industry experience with glass-fibre aluminium composites indicated that the thermal stresses of cool-down from cure would not be particularly problematic as long as care was taken to ensure a good bond between composite and metal. The key is to ensure that the metal surface is free from contaminates, and ideally free from surface oxidation as well. With aluminium, this requirement demands that the metal be either chemically etched or mechanically abraded to remove the natural oxide layer shortly before bonding is to take place. Sandblasting was found to be the most reliable method of achieving a strong bond, however unfortunately this process induces residual compressive stress on the metal's surface,[2] which in turn induces curvatures. This unintended curvature can be addressed by using sheet metal rollers to reform the sheet to the desired initial shape, or simply by sandblasting both sides of the sheet so that the moments induced by each surface's residual stresses cancel.

Hand sanding with coarse sandpaper was usually an acceptable method of surface prep, however the bond strength was not as good as with sandblasting. This result was qualitatively determined with simple, uninstrumented peel tests, which showed that the hand-sanded laminate failed by delamination at the metal-composite bondline, while the sandblast-prepared laminate instead delaminated between two plies of the composite, indicating a strong metal-composite bond.

Although it would be readily possible to bond cured composite to metal, the manufacturing process can be simplified by bonding the laminate and curing the composite in the same autoclave cycle, using the native prepreg epoxy to form the metal-composite bond. Post-cure bonding of composite and metal is still an alluring idea, as it allows the designer freedom to choose the structure's stress-free temperature, however such a luxury was not necessary for this work.

A CFRP/Al hybrid laminate was manufactured to the specifications of Table 2 upon a flat tool. After curing, the laminate was cut to a chevron-shaped planform using a diamond saw and hand file. A single 6 mm hole was drilled along the chevron's centreline, through which an M6 fastener mounted the chevron to a steel post. As shown in Fig. 7, a dial gauge was located 10 mm from the chevron's tip. The rig was placed in an oven, and the temperature

[2]The mechanics of this residual stress generation are presumed similar to that of shot peening, in which a surface is bombarded with high-speed steel balls in order to induce a state of residual compressive stress, which in turn delays fatigue crack initiation. It appears that the grit used in the sand-blaster was large and fast enough to give a similar residual stress field.



**Distribution A: Approved for public release; distribution unlimited.**

ramped up to 180°C at a rate of 1°C/min, with displacement measured at 5°C intervals.

Table 2: Manufacturing specifications for a chevron-shaped hybrid laminate.

| Layup<br>Al = 5251H22 aluminium alloy<br>Composite = AS7/M21 UD Prepreg | $[\mathrm{Al}/0_4]$ |
|---|---|
| Aluminium layer thickness [mm] | 1.20 |
| Composite layer ply thickness [mm] | 0.260 |
| Outer dims $L_x \times L_y$ | $175 \times 270$ |
| Cure temperature | 180°C |

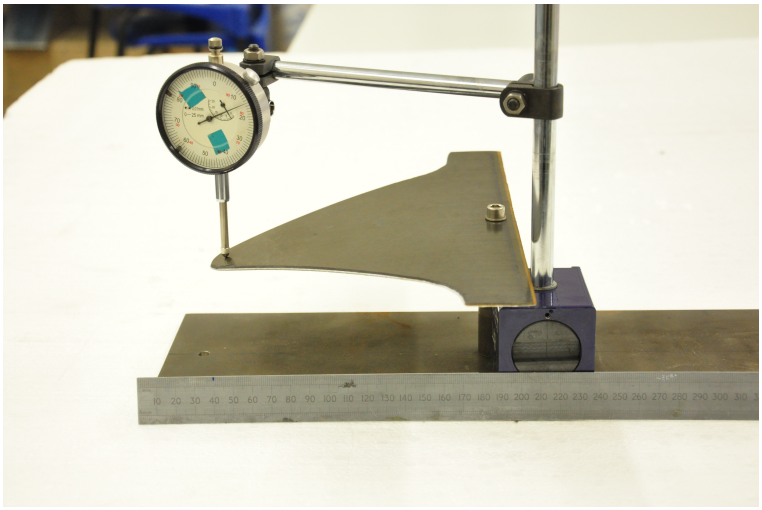


Figure 7: The CFRP/5251Al chevron-shaped laminate mounted in the dial-gauge test fixture. The fibre direction is parallel to the steel rule in the image.

The resulting displacements are plotted in Fig. 8. The temperature-displacement relationship is essentially linear, with no evidence of geometric nonlinearity. This result is to be expected, as this laminate develops nearly unidirectional thermal moments, and as it was cured on a flat tool, it preferentially develops curvature in the fibre direction with little competition from the perpendicular direction's small thermal moments.

A time-lapse image sequence of the laminate undergoing cool-down is shown in Fig. 9. Note that a small degree of curvature change in the transverse direction can be observed on the



**Distribution A: Approved for public release; distribution unlimited.**

extreme edges of the laminate, on account of the fact that the composite's $\alpha_2$ is not perfectly matched to the aluminium's CTE.

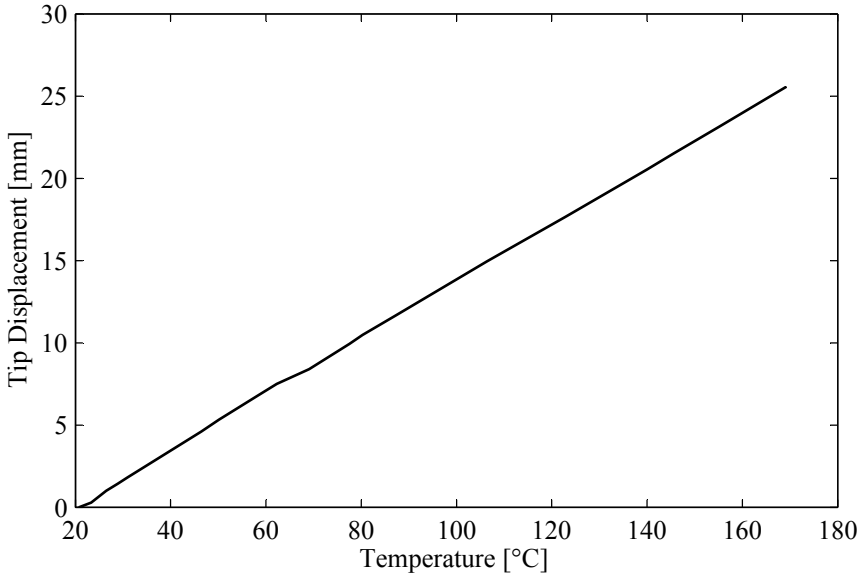



Figure 8: Tip displacement results for the CFRP/5251Al chevron-shaped laminate.



**Distribution A: Approved for public release; distribution unlimited.**

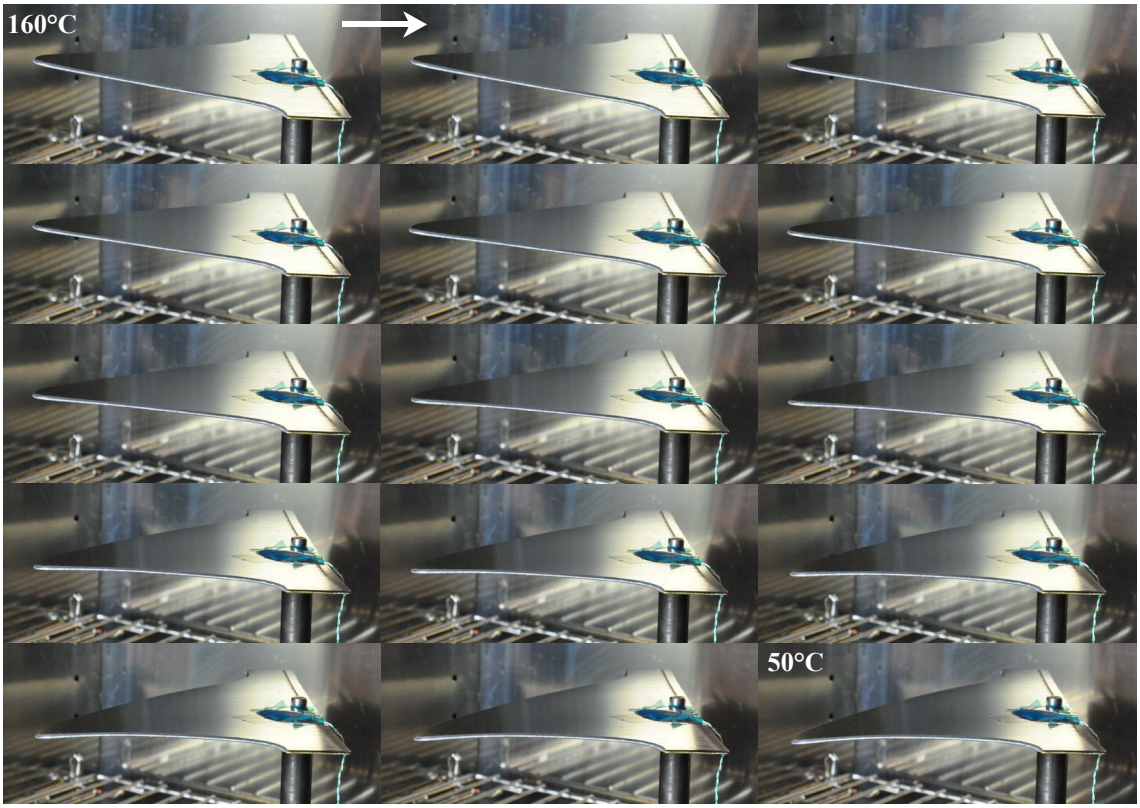



Figure 9: A time-lapse image sequence of the CFRP/5151Al chevron-shaped laminate cooling from 160°C to 50°C.

## 2.4 Hybrid Bimorphs using Angle-Ply Laminates

### 2.4.1 Theoretical Performance

CFRP makes a near-ideal low-expansion layer, as it has very high modulus, very low CTE, and low density. Despite these very favourable properties, there is still some scope for improvement. Halpin and Pagano [16] noted that composites with low-expansion fibres in a high-expansion matrix, when laminated in an angle-ply pattern $[(+\theta/-\theta)_n]$, can exhibit a CTE in the 0° direction that is less than both the fibre and matrix CTEs, given a suitable choice of $\theta$. Perhaps this behaviour can be exploited to further improve the performance of CFRP-metallic hybrid bimorphs. A laminate which uses an angle-ply laminate as the low-expansion layer is proposed, as shown in Fig. 10.



**Distribution A: Approved for public release; distribution unlimited.**

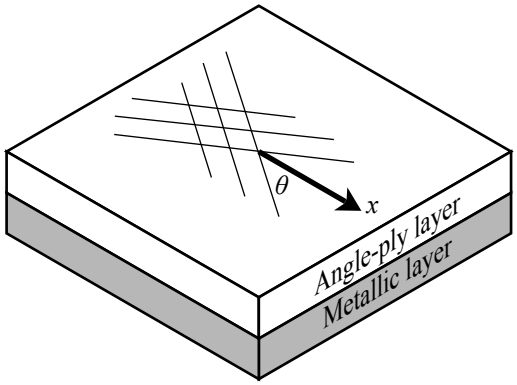



Figure 10: A sketch of a hybrid bimorph using an angle ply laminate as the low-expansion layer.

The effective CTEs and moduli of angle-ply laminates can be found in a straightforward manner using CLT, and are plotted over various $\theta$ values in Figs. 11-12, using typical intermediate modulus UD CFRP ply properties, namely $\alpha_1 = 0/^\circ\text{C}$ and $\alpha_2 = 30 * 10^{-6}/^\circ\text{C}$. The minimum $\alpha_x$ achievable using an angle ply laminate is $-3.34 * 10^{-6}/^\circ\text{C}$, which occurs at $\theta = 29.5^\circ$.

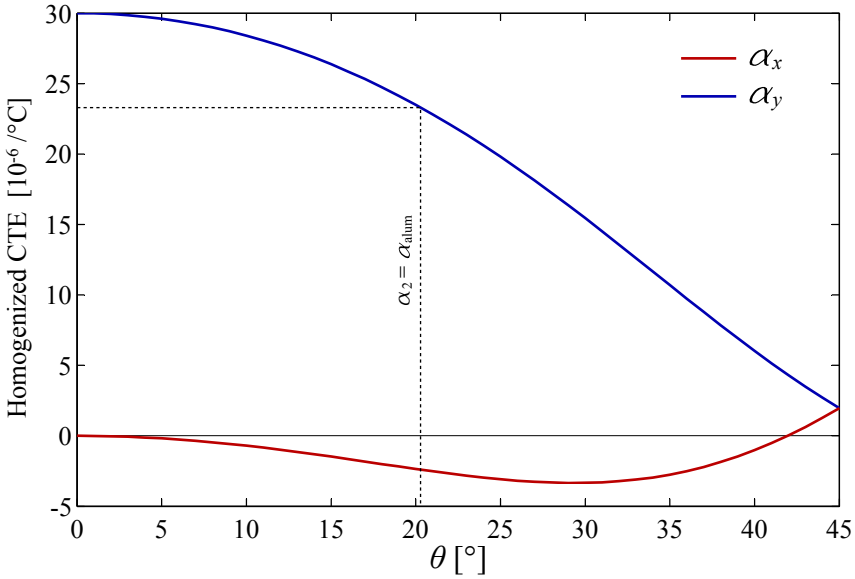



Figure 11: Principle CTEs of a homogenised angle-ply CFRP laminate of form $[(+\theta/-\theta)_n]$. The dashed line indicates the $\theta$ which gives matched CTEs in the $y$-direction when using aluminium alloy as the high-expansion layer.



**Distribution A: Approved for public release; distribution unlimited.**

This negative $\alpha_x$ of an angle-ply laminate can be explained by the fact that these laminates can have a very high Poisson's ratio, and thus if the angle-ply laminate has a high CTE in the $y$-direction, Poisson effects drive an opposite strain in the $x$-direction. If the material's $\alpha_1$ is already low to begin with, as is the present case, then the resulting $\alpha_x$ can be driven well into negative territory. The utility of this result is that shallow angle-ply laminates can have a greater CTE mismatch with the metallic high-expansion layer than is possible using a unidirectional layup.

Halpin and Pagano also noted that the $y$-direction CTE of angle-ply layups can be tailored based on fibre orientation angle, thus it is possible to create an angle-ply layup whose $y$-direction CTE is matched to the high-expansion layer's CTE. When the high-expansion layer is aluminium alloy, $\theta \approx 20°$ yields matched CTEs in the $y$-direction. With this orientation angle, it is likely feasible to create composite bimorphs which generate completely unidirectional thermal moments along the $x$-direction, i.e., there would be no thermal moments in the $y$-direction. This feature could be useful if the designer wished to avoid generation of transverse curvature, or to create a composite bimorph with completely unidirectional actuation moments and displacements, regardless of planform shape. Serendipitously, the orientation angles which yield matched $y$-direction CTEs with most engineering alloys (Al, Mg, Ti, etc.), happen to fall within the range of orientation angles which yield negative $\alpha_x$ in the composite layer. Thus, completely unidirectional actuation may be displayed while simultaneously extracting the benefits of increased CTE-mismatch in the $x$-direction.

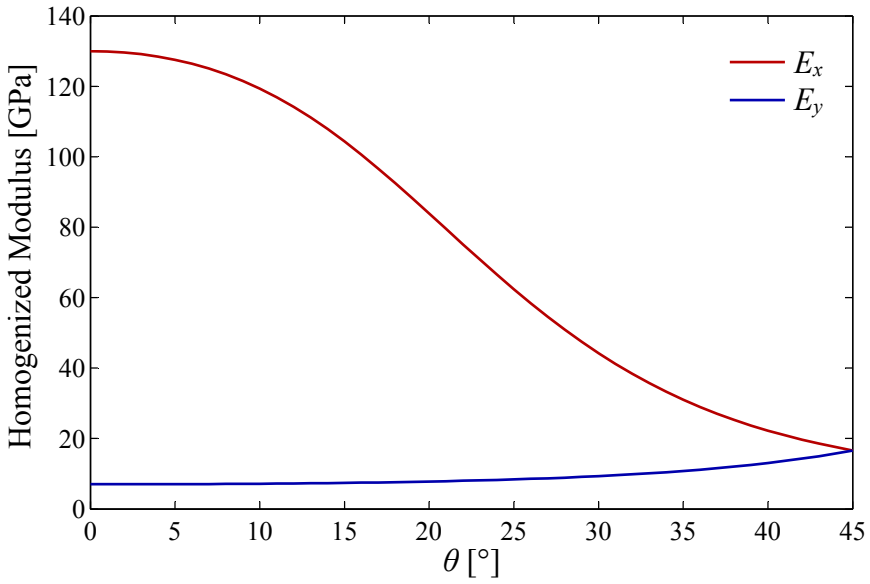



Figure 12: Principle moduli of a homogenised angle-ply laminate of form $[(+\theta/-\theta)_n]$.



**Distribution A: Approved for public release; distribution unlimited.**

There is of course a price to be paid in terms of the angle-ply laminate's effective $E_x$ as the orientation angles increase, as shown in Fig. 12. Recalling that our goal is to maximise $P_{\mathrm{w}}$, it is not immediately obvious whether the benefit of greater CTE mismatch attainable with angle-ply laminates is negated by a lesser $E_x$ compared to 0° UD layups. As it turns out, *small orientation angles do in fact yield a small net benefit in terms of weight-specific performance index,* as shown in Fig. 13. The maximum $P_{\mathrm{w}}$ is attained at $\theta \approx 8.5°$ for the presently studied CFRP/Al laminate. Perhaps the true value of Fig. 13 is to show that there is little penalty applied to $P_{\mathrm{w}}$ for $\theta < 20°$. In fact, the aforementioned CFRP/Al laminate with $\theta \approx 20°$ and matched $y$-direction CTEs, sees a decrease in $P_{\mathrm{w}}$ by only 5.1% relative to maximum, and only 4.7% relative to the $\theta = 0°$ case. This penalty is well justified in light of another benefit to the angle-ply approach, which is discussed in the following section.

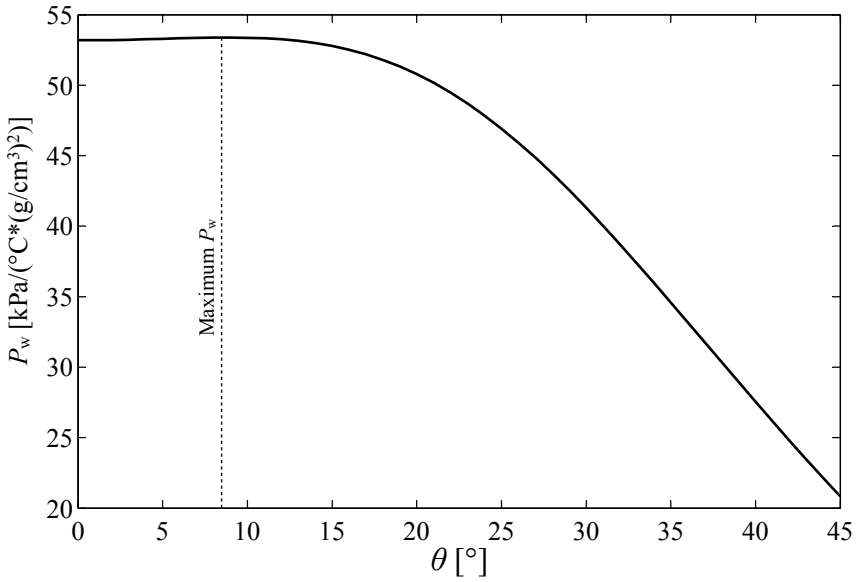



Figure 13: Weight specific bimorph performance index of a CFRP/Al laminate, with an angle-ply layup of form $[(+\theta/-\theta)_n]$.

### 2.4.2 Manufacturing Considerations

There is one more benefit of an angle-ply layup in fibre-metal bimorphs. In our experience, thick CFRP/Al bimorphs using more than about four consecutive 0° plies sometimes developed matrix cracks during manufacturing and testing. A composites manufacturing rule-of-thumb is to avoid stacking more than four plies of the same orientation for this very reason, and thus the angle-ply concept offers a solution to this matrix-cracking issue.



**Distribution A: Approved for public release; distribution unlimited.**

Woven fabrics are often preferred to UD plies on account of their easier handling qualities, greater impact tolerance, and resistance to gross matrix cracking. With the use of a picture-frame fabric shear rig, it is possible to modify woven fabric to take on the material properties of the aforementioned shallow angle-ply laminates. A woven ply, oriented at $\pm 45°$ degrees to our $x-y$ axes, has similar homogenised properties to an angle ply of form $[(+45/-45)_n]$. This woven orientation is denoted as $[\pm 45_{\text{wv}}]$. However, it is quite easy to shear woven fabric such that its orientation angle is reduced to as little as $[\pm 20_{\text{wv}}]$. A fair amount of tow distortion is introduced by this shearing, therefore it is difficult to say without further analysis how well this sheared woven ply matches the properties of a $[(+20/-20)_n]$ angle ply laminate. A close-up image of this laminate's sheared weave is given in Fig. 14, with an adjacent comparison to an unsheared fabric.

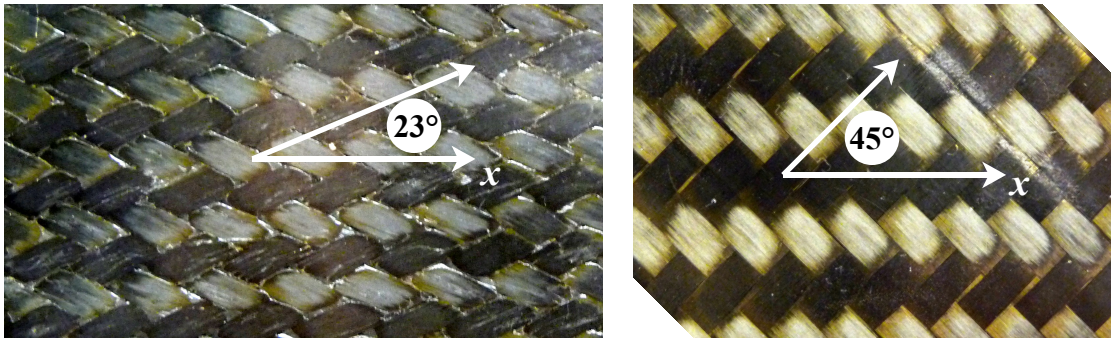



Figure 14: A 2x2 twill woven fabric sheared to $[\pm 23_{\text{wv}}]$ , left, and the same fabric in its unsheared configuration, $[\pm 45^{\circ}_{\text{wv}}]$, right.

The development of angle-ply fibre-metal laminates turned out to be more fruitful than expected, especially with regard to the practical benefits of woven laminates. Although time constraints prevented further exploration of such concepts, the author believes there are many interesting opportunities for future research in this domain.

# 3 Multistability Modelling Development

The goal of our modelling efforts is to build and refine tools which predict the curvature-temperature relationship of thin, initially curved bimorph laminates.

We begin by stating our modelling assumptions:

1. Material properties are linear elastic, but may vary with temperature.



**Distribution A: Approved for public release; distribution unlimited.**

2. Temperature may vary through the thickness of the laminate.

3. Strains are small, rotations are moderate, though displacements may be large. (von Karman plate theory)

4. Plane sections remain normal to the midplane, i.e., transverse shear is assumed negligible.

5. Thermal expansion in the thickness direction is neglected.

6. The plate may have constant initial curvature. Although our model is an extension of von Karman plate theory, the inclusion of initial curvature leads to shell behavior, thus the structure is henceforth referred to as a shell.

7. The plate is square or rectangular in planform, and not constrained by boundary conditions.

## 3.1 Mechanics

### 3.1.1 Achieving Snap-Through Behaviour by Exploiting the Geometrically Nonlinear Flexural Response of Thin, Initially Curved Shells

Thin shells with initial curvature display nonlinear bending response when loaded with moments which act to induce curvature perpendicular to the initial curvature direction [17]. Consider the shell shown in Fig. 15, with an applied internal bending moment (perhaps from thermal loading) along the $x$-direction, $M_{\mathrm{T}x}$. From a beam-mechanics perspective, the effective bending stiffness of the structure as a whole along this direction is a function of not only the laminate's constitutive relations, but also the geometric stiffness granted by the curvature in the $y$-direction, $\kappa_y$. The latter stiffens the plate in the same manner that an extended carpenter's tape measure is stiffened by its transverse curvature. Alternatively, one can view the problem from a shell mechanics perspective, whereby a singly curved surface initially resists development of Gaussian curvature through storage of membrane strain energy. When $M_{\mathrm{T}x}$ exceeds some critical value, it becomes energetically favourable for this thin-walled structure to accommodate load with bending strain energy instead, manifested by curvature generation in the $x$-direction. As shown in Fig. 15b-c, this increase of $\kappa_x$ is accompanied by loss of $\kappa_y$ as required to minimise Gaussian curvature change and its associated membrane strain energy. Returning to the beam perspective, the geometric bending stiffness granted by transverse curvature is lost upon Brazier collapse [18] of the section to



**Distribution A: Approved for public release; distribution unlimited.**

a flat strip,[3] allowing the beam to deform in the direction of moment application. This behaviour can be observed by bending a carpenter's tape measure until it snaps into a kinked shape.

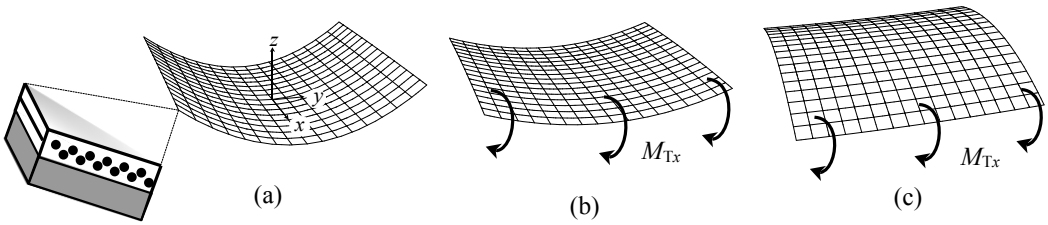



Figure 15: Response of curved shell to applied internal bending moment perpendicular to initial curvature direction.
a) A laminate is constructed from fibre-composite and metallic layers, with the fibres oriented perpendicular to the direction of initial curvature.
b) Upon cooling from its stress-free temperature, thermally induced moments develop within the laminate, which are primarily oriented along the fibre direction.
c) When a critical internal moment is reached, the initial curvature is overcome, and the resulting loss of stiffness allows the laminate to snap to a new shape.

The addition of internal bending stresses can allow a curved shell to take on multistable properties [19], a property which has found application in deployment systems [20]. By controlling the magnitude and direction of internal bending stresses, perhaps via a thermal bimorph arrangement, it is possible to engender a shell structure with highly nonlinear curvature response to temperature change. This behaviour may include a rapid, but not necessarily instantaneous, change in shape over a certain temperature range, or in more extreme cases, may include snap-through and multistable behaviour.

Figure 16 provides a generic example intended to illustrate the role of initial curvature in enabling snap-through behaviour triggered by internal moments, such as those arising due to thermal loads. It was created using the multistability model presented in Eckstein *et al.* [21], and describes the stability of a flat plate and two cylindrically curved shells subject to internal moments arising from various bimorph types. The white "background" region represents combinations of internal moments which yield only one stable shape, while the coloured regions represent combinations which yield bistable behaviour. Essentially, the

[3]L.G. Brazier observed that thin-walled beams experience distortions of their cross section under bending loads. Usually, the tendency is for the cross-section to be flattened towards the beam's neutral axis, as would be found by bending a plastic drinking straw until it kinks.



**Distribution A: Approved for public release; distribution unlimited.**

coloured regions represent the overlap of each shape's solution space, and thus within this region, there exist two stable shapes.

Initial cylindrical curvature has the effect of shifting the region of bistability by an amount negatively proportional to, and along the internal moment axis of the initial curvature direction. This shift in response is exemplified by the green and blue regions in Fig. 16, which corresponds to progressively greater negative cylindrical curvature in the $y$-direction (as illustrated in Fig. 15a). Thus, these regions are shifted along the $y$-axis from the red region by an amount proportional to their initial curvature. This negatively proportional shift applies so long as the initial curvature is cylindrical. A full explanation of this observation is given in Subsection 3.4.2.

A thermally driven snap-through event occurs when the one laminate shape is driven beyond its stable region as a result of thermally induced internal moments, as graphically illustrated by paths (a) and (b) in Fig. 16. Tracing from the origin, both paths enter the bistable region of the initially cylindrical shell, although no snap-through occurs as of yet because the initial shape remains stable. Upon exit of the bistable region, the initial shape becomes unstable, and the laminate snaps to a cylinder at the points indicated by the circular markers. The same process is described by Fig. 15. Reversing the process, snap-through would instead occur at the square markers, as these represent the points where the second shape ceases to be stable, resulting in a snap-through transition back to the initial shape.

The conditions required for snap-through behaviour are now discussed. In the case of a thermally driven bimorph, the internal moments $M_{\mathrm{T}x}$ and $M_{\mathrm{T}y}$ are both proportional to temperature, barring slight variations due to temperature-dependent material properties. Paths (a), (b), and (c) in Fig. 16 demonstrate this proportionality, in that they are straight lines emanating from the origin. Under these circumstances, we can observe that for an initially flat plate, any straight path drawn from the origin may enter, but never exit the red region. That is to say that snap-through is not possible with initially flat plates subject to proportional moments, such as those driven by temperature change. Path (c) represents the special case of curvature bifurcation upon entering the bistable region as described by Hyer [22], however this behaviour is not to be mistaken for a snap-through process as the curvatures are still continuous with respect to temperature. For proportional moments such as those generated by thermal bimorphs, initial curvature is a necessary ingredient for snap-through behaviour, as it allows paths such as (a) and (b) to traverse and exit the blue and green bistability regions. This finding is generalised by stating that any point along the boundary of a bistability region is eligible for snap-through driven by proportional moments, so long as a line drawn between this point and the origin also intercepts another boundary of the same region.



**Distribution A: Approved for public release; distribution unlimited.**

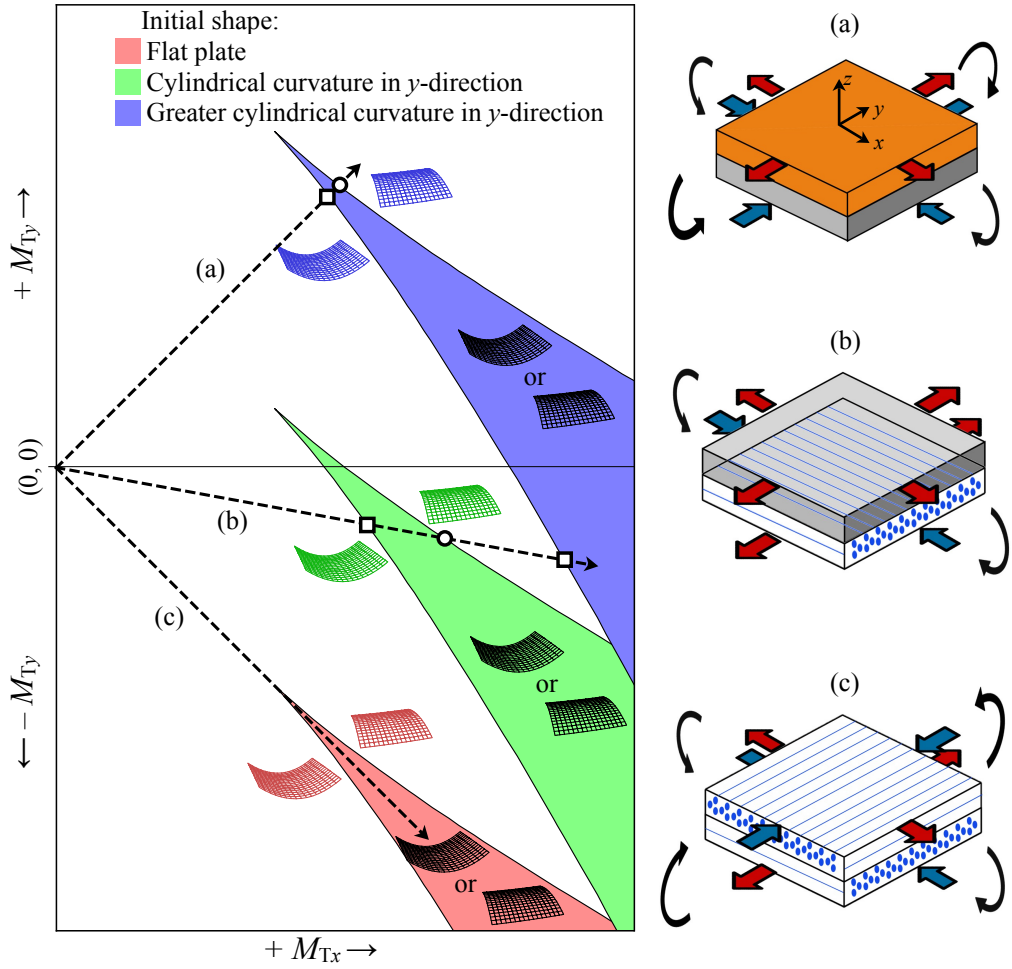



Figure 16: A bistability phase diagram, where coloured regions indicate thermal moment combinations which yield bistability. Circular markers denote snap-through points for increasing moments, while square markers denote the same for decreasing moments. The pairs of surface grids on either side of each region represent the stable shape achieved upon exiting the region's respective side. Moment paths (a-c) are plotted for three classes of bimorph laminates, which are illustrated at right with their respective ply thermal stresses and resulting thermal moments.
a) A bimorph made from isotropic layers, which exhibits equal moments in all directions.
b) A hybrid fibre-metal laminate, which generates moments primarily along the $x$ direction.
c) A $[0_n/90_n]$ unsymmetric composite laminate, which exhibits equal but opposite moments along its principle directions.



**Distribution A: Approved for public release; distribution unlimited.**

In addition, one can also conclude from Fig. 16 that the moments generated cannot be equal and opposite for snap-through behaviour. This conclusion is exemplified by path (c), which even in the case of initial curvature, would only enter a bistable region, but never achieve the necessary exit required for snap-through. This observation implies that the unsymmetric $[0_n/90_n]$ class of laminates popular in the study of bistability are inherently incapable of displaying thermally driven snap-through behaviour, regardless of the laminate's initial curvature.[4] Path (b) achieves snap-through because the magnitudes of $M_{\mathrm{T}x}$ and $M_{\mathrm{T}y}$ are sufficiently unequal. This behaviour can be achieved using the fibre-metal hybrid laminates discussed in Section 2.

One can also observe that with sufficient initial curvature, equal and same-sign moments can also yield snap-through behaviour. This response is exemplified by Path (a) in Fig. 16. This path intersects the bistability region of an initially cylindrical shell, as long as the initial curvature of that shell was sufficiently large. It is also worth noting that if one is not constrained by the proportional internal moments inherent in thermal bimorphs, it would be possible to achieve a moment path which need not be a straight line emanating from the origin. Such a path could criss-cross the bistable region according to the designer's wishes. In other words, the ability to actuate $M_{\mathrm{T}x}$ independently from $M_{\mathrm{T}y}$, perhaps via piezoelectric actuators, would allow snap-through to be achieved in a laminate possessing any degree of initial curvature. This consideration is beyond the scope of the present work, however Fernandes *et al.* [23] have studied this concept in-depth.

## 3.2 Modelling Methodology

*The modelling novelty introduced in this work can be summarised as follows:*

In the present modelling technique, thermally induced curvatures are first measured from representative strips of a laminate across a range of temperatures. The model then uses these measured 1D curvatures to calculate the thermally induced 2D curvatures of a shell constructed from the same layup.[5] The main result is that the model no longer requires CTE material data, nor does it need the laminate's stress-free temperature. In addition, other strain-inducing effects such as resin cure shrinkage are automatically accounted for with this approach.

[4] Although $[0_n/90_n]$ laminates are not isotropic, their stability phase diagrams are qualitatively similar to Fig. 16 on account of their equal bending stiffness and thermal moment magnitudes in the $x$ and $y$ directions.

[5] 1D results can also be scaled according to the laminate's thickness, allowing the experimental results to be generalised to an extent.



**Distribution A: Approved for public release; distribution unlimited.**

### 3.2.1 Description of Thermal Curvature

In most prior multistability studies [22, 24, 25], the loads on the structure were determined via computation of thermal stresses, which were then integrated across the laminate's thickness to find internal moments and stress resultants. The thermal stresses themselves were computed from a prescribed temperature change and known thermoelastic material data, namely CTEs and moduli. The shortcoming of this approach towards calculating thermal loads is that the complete stress state must be known at some reference temperature. Previous workers have generally used the cure temperature as that reference, for which a zero-stress state was assumed [22, 24, 26]. While this approach simplifies calculations and provides convenient comparisons with finite element models, it ignores the presence of non-thermoelastic strains such as plastic deformation, resin shrinkage, or tool-part interactions. Present work with hybrid fibre-metal laminates, as well as congruent research [27], has revealed that non-thermoelastic strains generally cannot be neglected, as they can significantly affect predicted curvatures. Because these strains are highly layup and process-dependent [28], reliably calculating them *a priori* for general cases is presently regarded as impractical.

Instead, a technique is proposed in which the components of the thermally induced curvature vector $\boldsymbol{\kappa}_{\mathrm{T}}$ are each experimentally measured at all temperatures of interest, and the resulting values are utilised directly as loading inputs into the model's total potential energy expression. In the scope of this work, these thermal curvatures are due to thermal expansion strain, however in general cases they may arise from other actuation strain sources such as hygroscopic or shape-memory-induced strain.[6] Thermal curvatures are defined as the curvature change the laminate would achieve in an unrestrained state, i.e., if it were freed from the geometrically nonlinear kinematics which otherwise restrain its deformation. In this state, curvatures are decoupled from membrane strains, and thus any thermally induced internal bending moment translates directly and proportionally to thermal curvature. For this reason, thermal curvatures are in fact coincident to the those that would be predicted by CLT. Thermal curvature along a given direction may be measured by fabricating a long, narrow, beam-like strip of the laminate under investigation, such that the stiffening effects of transverse curvature [17] are negligible. As long as no mechanical loads are applied, the curvature observed in the resulting strip is the thermal curvature of the laminate along the strip's lengthwise direction. This approach of using experimentally measured thermal curvatures as loading inputs effectively amounts to replacing the conventional uniaxial measurement of CTEs with a flexural measurement of CTE mismatch. Besides automatically accounting for non-thermoelastic strains, this approach also avoids the need for the specialised

[6] The model makes no distinction regarding the type or source of expansion strain. It would be perfectly admissible to measure the components of $\boldsymbol{\kappa}_{\mathrm{T}}$ against any number of environmental variables, e.g.,voltage in piezoelectric laminates, or moisture content of biological materials.



**Distribution A: Approved for public release; distribution unlimited.**

instrumentation required for uniaxial CTE measurement, as thermal curvature may instead be quantified with any number of flexural displacement-measuring techniques such as laser metrology or even simple dial gauges. The use of thermal curvature as a loading term is not new, particularly in the field of multistability where it has been referred to generically as *inelastic curvature* or *relaxed curvature*. In particular, this work adopts the original symbology of Mansfield while incorporating prior techniques for computing total potential energy in terms of thermal curvatures. [12, 29, 30].

### 3.2.2 Model Development

The general theory, assumptions, and solution procedures of the presently developed model are shared with the model presented in Eckstein *et al.* [21]. The main difference is the replacement of thermal stresses and moments with thermal curvature terms. First, the expression for total potential energy in terms of total and thermal strains is given as

$$\Pi = \int_{\frac{-L_x}{2}}^{\frac{L_x}{2}} \int_{\frac{-L_y}{2}}^{\frac{L_y}{2}} \int_{\frac{-h}{2}}^{\frac{h}{2}} \frac{1}{2} \left(\epsilon_i - \epsilon_{\mathrm{T}i}\right) \overline{Q}_{ij} \left(\epsilon_j - \epsilon_{\mathrm{T}j}\right) \, dz \, dy \, dx, \tag{8}$$

where $\epsilon_i$ are total strain components, and $\epsilon_{\mathrm{T}i}$ are thermal strain components, with $i$, $j = x$, $y$, $xy$. Assuming transverse shear effects are negligible, the total and thermal strains are decomposed into midplane extension and curvature components as

$$\epsilon_i - \epsilon_{\mathrm{T}i} = \left(\epsilon_i^0 - \epsilon_{\mathrm{T}i}^0\right) + z \left(\Delta\kappa_i - \kappa_{\mathrm{T}i}\right), \tag{9}$$

where $\epsilon_i^0$ and $\epsilon_{\mathrm{T}i}^0$ represent membrane (i.e. midplane) total and thermal strains, respectively; while $\Delta\kappa_i$ and $\kappa_{\mathrm{T}i}$ are the curvature changes from the initial state and thermal curvatures, respectively. Next, Eq. (9) is substituted into Eq. (8), and the integral is evaluated through the thickness. The evaluation of this integral yields terms identical to the classical definitions of the $\boldsymbol{A}$, $\boldsymbol{B}$, and $\boldsymbol{D}$ laminate constants, and thus they are substituted into the result to give

$$\Pi = \int_{\frac{-L_x}{2}}^{\frac{L_x}{2}} \int_{\frac{-L_y}{2}}^{\frac{L_y}{2}} \left( \frac{1}{2} \begin{bmatrix} \boldsymbol{\epsilon}^0 - \boldsymbol{\epsilon}_{\mathrm{T}}^0 \\ \Delta\boldsymbol{\kappa} - \boldsymbol{\kappa}_{\mathrm{T}} \end{bmatrix}^{\top} \begin{bmatrix} \boldsymbol{A} & \boldsymbol{B} \\ \boldsymbol{B} & \boldsymbol{D} \end{bmatrix} \begin{bmatrix} \boldsymbol{\epsilon}^0 - \boldsymbol{\epsilon}_{\mathrm{T}}^0 \\ \Delta\boldsymbol{\kappa} - \boldsymbol{\kappa}_{\mathrm{T}} \end{bmatrix} \right) dy \, dx. \tag{10}$$

Note that the tensorial notation has been dropped for vector representation, while the superscripted symbol $\top$ denotes transpose.

Further simplifications are possible if we restrict ourselves to uniform thermal strain in the $x$-$y$ directions. Fernandes *et al.* [23] have shown that for plates and shells with free boundary conditions, midplane strains due to in-plane material growth only contribute to



**Distribution A: Approved for public release; distribution unlimited.**

the total potential energy of the plate when they vary at equal to or greater than second order with respect to the spatial dimensions, on account of the second order differential nature of Gauss' *Theorema Egregium*. In other words, the growth due to thermal midplane strain is not resisted mechanically in any manner when thermal midplane strains vary spatially at less than second order, thus there can be no storage of strain energy on account of it. The direct result is that if we assume the distribution of thermal strain is invariant across the planform of the laminate, we may neglect the thermal midplane strain terms $\boldsymbol{\epsilon}^0_{\mathrm{T}}$. Nonetheless, we must still retain the total midplane strain terms in order to account for membrane strain energy arising due to change in the laminate's Gaussian curvature. The final form of our total potential energy expression is thus:

$$\Pi = \int_{\frac{-L_x}{2}}^{\frac{L_x}{2}} \int_{\frac{-L_y}{2}}^{\frac{L_y}{2}} \left( \frac{1}{2} \begin{bmatrix} \boldsymbol{\epsilon}^0 \\ \Delta\boldsymbol{\kappa} - \boldsymbol{\kappa}_{\mathrm{T}} \end{bmatrix}^{\top} \begin{bmatrix} \boldsymbol{A} & \boldsymbol{B} \\ \boldsymbol{B} & \boldsymbol{D} \end{bmatrix} \begin{bmatrix} \boldsymbol{\epsilon}^0 \\ \Delta\boldsymbol{\kappa} - \boldsymbol{\kappa}_{\mathrm{T}} \end{bmatrix} \right) dy\, dx. \tag{11}$$

The loading terms contained within $\boldsymbol{\kappa}_{\mathrm{T}}$ are sourced by experimental measurement in this work, however they may be calculated from material data using CLT if desired. The procedure is outlined by Collier [31], whereby the author also describes how thermal curvatures may be modelled in an FE implementation. The remainder of the solution procedure is identical to the method described in Eckstein *et al.* [21].

## 3.3 Experimental Verification of Model

### 3.3.1 Fabrication of Hybrid Laminate Shell and Strip Specimens

Hybrid laminates were constructed according to the parameters given in Table 3. These laminates were fabricated from a layer of 5251 aluminium, bonded to a layer of Hexcel AS7/M21 unidirectional prepreg carbon composite. Prior to curing, the 5251Al layer was prepared for bonding by scuffing with P200 silicon carbide sandpaper.[7] The epoxy contained within the prepreg material was used as the bonding agent, and thus the curing of the composite layer and bonding to the aluminium layer was carried out simultaneously during autoclave processing.

Thermal curvature $\boldsymbol{\kappa}_{\mathrm{T}}$ was measured using beam-like strip specimens. These specimens were cut from a $230 \times 230$ mm hybrid laminate plate, which was autoclave cured upon a flat tool.

[7] Sandblasting was also found to be an effective method of surface preparation from a bond strength standpoint, however as mentioned in Section 2.3, this process creates residual compressive stresses upon the surface of the aluminium sheet similar to the mechanics of shot-peening. As long as the same preparation method is used for both strip and shell specimens, the curvature induced by these residual stresses are fully accounted for within the analytical model.



**Distribution A: Approved for public release; distribution unlimited.**

Autoclave pressure was relieved prior to cool-down. This procedure allows the laminates to develop curvature during cool-down without being held constrained against their tool, which a prior experiment had shown was responsible for a small degree of yielding of the aluminium layer. The resulting panels, prior to cutting to strips, are shown in Fig. 17. Strips of 230 mm length and widths between 10 mm and 50 mm were cut both parallel and perpendicular to the fibre direction. Observation of the room temperature curvature of these strips showed that the stiffening effects of transverse curvature were insignificant for strip widths of less than 30 mm, and thus strips of 20 mm width were judged to yield accurate measurements of $\kappa_{\mathrm{T}x}$ and $\kappa_{\mathrm{T}y}$. Due to the nature of the laminate, no twist curvature $\kappa_{\mathrm{T}xy}$ was anticipated. This assertion is supported by results from the testing described in the following section. The layup and final strip dimensions are given in Table. 3.

An initially curved CFRP/Al hybrid laminate was autoclave cured on a cylindrically curved aluminium tool, with layup and dimensions as given in Table. 3. The aluminium layer preparation was identical to that for the flat plates discussed above, however for this case, the aluminium layer was also roll-formed to match the tool curvature.



Figure 17: Hybrid laminate specimens cured upon a flat tool. The lower-left and upper-left panels were cut into 0° and 90° strip specimens, respectively. The right-most two panels were not used in the course of this experiment.



**Distribution A: Approved for public release; distribution unlimited.**

Table 3: Test article manufacturing parameters for hybrid fibre-metal laminates.

| | 0° strip cut from $230 \times 230$ mm plate for measurement of $\kappa_{\mathrm{T}x}$ | 90° strip cut from $230 \times 230$ mm plate for measurement of $\kappa_{\mathrm{T}y}$ | Curved shell for evaluation of thermally driven snap-through behaviour |
|---|---|---|---|
| Layup | $[\mathrm{Al}_1/0_4^\circ]$ | $[\mathrm{Al}_1/90_4^\circ]$ | $[\mathrm{Al}_1/0_4^\circ]$ |
| 5251 Al sheet thickness [mm] | 1.20 | 1.20 | 1.20 |
| AS7/M21 ply thickness [mm] | 0.286 | 0.286 | 0.286 |
| Side lengths [mm] | 230 x 20 | 230 x 20 | 230 x 230 |
| Tool curvature $\hat{\kappa}_x[\mathrm{mm}^{-1}]$ | 0 | 0 | 0 |
| Tool curvature $\hat{\kappa}_y[\mathrm{mm}^{-1}]$ | 0 | 0 | $-1/400$ |

Temperature-dependent material data for Hexcel AS7/M21 UD prepreg was obtained by experiment, with results given in Table 4. Material data for 5251 aluminium alloy was sourced from the ESDU Metallic Materials Data Handbook [32], and is also shown in Table 4. Where data at intermediate temperature values was unavailable, data from similar alloys was utilised to aid interpolation.

Table 4: Thermoelastic material data for AS7/M21 UD composite and 5251 aluminium alloy. Although the present model does not require thermal expansion material data, it is provided here nonetheless to aid with the reader's understanding of the results. Thermal expansion coefficients use a reference temperature of 20°C.

| | Hexcel AS7/M21 UD Prepreg | | | | | | Al 5251 | | |
|---|---|---|---|---|---|---|---|---|---|
| Temp. [°C] | $E_1$ [GPa] | $E_2$ [GPa] | $G_{12}$ [GPa] | $\nu_{12}$ [-] | $\alpha_1$ $[\frac{10^{-6}}{^\circ C}]$ | $\alpha_2$ $[\frac{10^{-6}}{^\circ C}]$ | $E$ [GPa] | $\nu$ [-] | $\alpha$ $[\frac{10^{-6}}{^\circ C}]$ |
| 30 | 129.55 | 8.85 | 5.28 | 0.33 | -2.3 | 23.4 | 72.0 | 0.33 | 23.0 |
| 60 | 127.99 | 8.42 | 4.88 | 0.33 | -2.1 | 27.8 | 71.3 | 0.33 | 23.0 |
| 90 | 127.47 | 7.92 | 4.65 | 0.33 | -1.5 | 28.6 | 70.6 | 0.33 | 23.0 |
| 120 | 127.18 | 7.57 | 4.50 | 0.33 | -0.5 | 30.0 | 69.8 | 0.33 | 23.2 |
| 150 | 126.11 | 7.18 | 4.26 | 0.33 | 1.7 | 32.1 | 68.4 | 0.33 | 23.4 |
| 170 | 125.58 | 6.76 | 4.01 | 0.33 | 2.6 | 33.5 | 67.7 | 0.33 | 23.6 |
| 180 | 125.31 | 6.48 | 3.77 | 0.33 | 2.3 | 33.5 | 67.0 | 0.33 | 23.6 |



**Distribution A: Approved for public release; distribution unlimited.**

### 3.3.2 Measurement of Thermal Curvatures and Snap-Through Behaviour of Hybrid Laminate Shells

Shell and strip displacements were measured by digital image correlation (DIC), an optical 3D displacement measurement technique. The test articles were mounted on a steel rig using a single M6 fastener secured to a post, and placed in an oven as shown below in Fig. 18. Thermocouples were adhered to the composite layer with the aid of conductive paste both near and afar from the mounting post. Their readings were compared to ensure that the thermal lag induced by heat conduction to the test rig was minimal. In the course of testing, the thermocouple readings diverged by no more than 4°C. Temperature was ramped from 20°C-180°C at a rate of 2°C/min, then back down to 20°C at an equal rate.

Each DIC frame captures the displacements of approximately 20,000 points across the surface of the shell. Curvatures $\kappa_x$ , $\kappa_y$, and $\kappa_{xy}$ are determined by fitting the measured displacements to a surface of the form $w = \frac{1}{2}\left(ax^2 + by^2 + cxy\right)$. The fitting coefficients $a$, $b$, and $c$ yield the curvatures via the following relations

$$\begin{bmatrix} \kappa_x \\ \kappa_y \\ \kappa_{xy} \end{bmatrix} = \begin{bmatrix} -\frac{\partial^2 w}{\partial x^2} \\ -\frac{\partial^2 w}{\partial y^2} \\ -2\frac{\partial^2 w}{\partial x\, \partial y} \end{bmatrix} = \begin{bmatrix} -a \\ -b \\ -c \end{bmatrix}. \tag{12}$$

An identical temperature profile and curvature measurement procedure is utilised for measuring the thermal curvatures of the strip specimens.



**Distribution A: Approved for public release; distribution unlimited.**

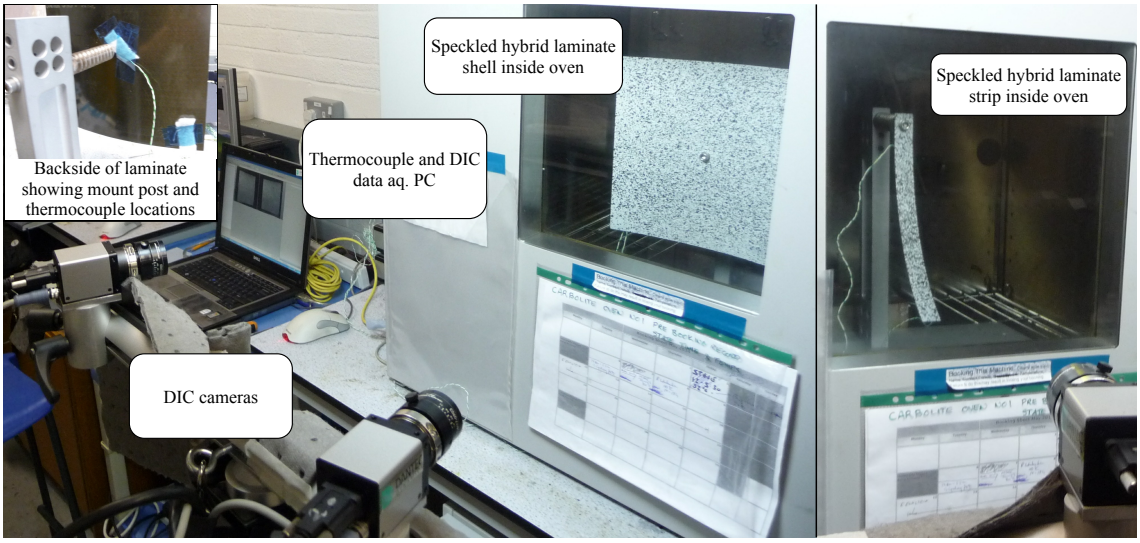



Figure 18: Hybrid laminate oven test setup, showing speckled shell (left) and strip (right) test articles mounted inside oven.

## 3.4 Modelling Results and Discussion

### 3.4.1 Experimental Measurements of Thermal Curvature

The thermal curvatures measured from the strip specimens specified in Table 3 are plotted in Fig. 19. This figure is best viewed from right to left, on account of the fact that thermal strains increase as temperature decreases. This measurement of non-zero thermal curvature at cure temperature (180°C) indicates the presence of non-thermoelastic strains. As mentioned in Subsection 3.2.1, these strains are likely due to resin shrinkage and/or tool-part interactions. Throughout the measured temperature range, $\kappa_{\mathrm{T}x}$ varies linearly with temperature, barring minor perturbations. This trend falls in line with expectations, as both the composite and metallic layers have nearly constant CTE values with respect to temperature, in the direction parallel to the fibres. On the other hand, $\kappa_{\mathrm{T}y}$ shows a slightly nonlinear dependence on temperature, an effect likely due to variation of composite layer's CTE in the direction perpendicular to the fibres. These measured thermal curvatures serve as the loading inputs used to generate modelling results for the following sections.



**Distribution A: Approved for public release; distribution unlimited.**

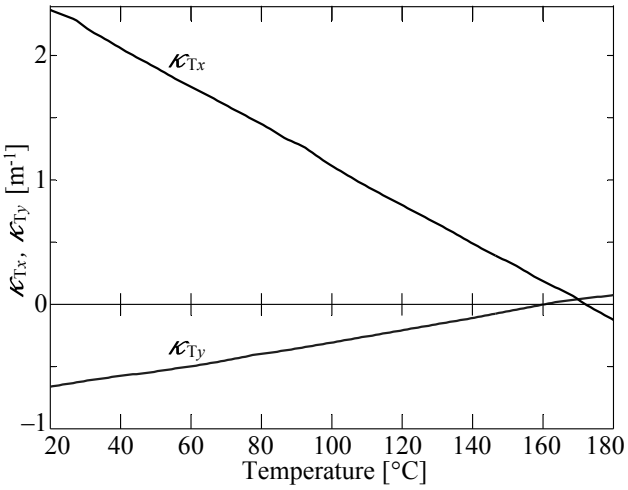



Figure 19: Experimentally measured thermal curvatures of the strip specimens described in Table 3.

### 3.4.2 Model Predictions Regarding the Influence of Initial Curvature

A stability phase diagram is given in Fig. 20 for the laminate specified in Table 3.[8] The results are plotted for various initial curvatures to demonstrate its effects upon the laminate's response to thermal loading. The bistable regions for each initial curvature are simply copies of each-other shifted along the $y$-axis by a value opposite to their corresponding initial curvatures. This interesting feature is only observed when the initial shape is a developable surface. Elaborating upon that statement, for non-developable initial shapes, initial curvature enters Eq. (11) both via the midplane stretching vector $\boldsymbol{\epsilon}^0$ and the curvature change vector $\Delta\boldsymbol{\kappa}$. However, $\boldsymbol{\epsilon}^0$ only contains initial curvature terms in the form of $\hat{a}\hat{b} - \frac{\hat{c}^2}{4}$; see Eckstein *et al.* [21]. This form represents the Gaussian curvature of the initial shape, and thus for the case of developable initial shapes, these terms collectively vanish. Thus, the only remaining avenue for initial curvature to enter Eq. (11) is via $\Delta\boldsymbol{\kappa}$. The curvature terms of Eq. (11) can be expanded as $\Delta\kappa_i - \kappa_{\mathrm{T}i} = \kappa_i - (\hat{\kappa}_i + \kappa_{\mathrm{T}i})$. This form makes it apparent that initial curvature appears in the same term as thermal curvature, and thus we can see that the effect of initial curvature is equivalent to the respective thermal curvature, so long as the initial curvature is developable. It also follows that any potential energy minimum

[8]The stability phase diagram presented in Fig. 20 is similar to that in Fig. 16, however the bistable regions are now specified in terms of thermal curvatures rather than thermally induced internal moments in keeping with the present experimental approach. This change effectively amounts to rescaling each axis proportional to the laminate's respective bending stiffnesses. Thus, the shapes of the bistable regions in Fig. 20 are distorted from their appearance in Fig. 16 due to the laminate's flexural anisotropy.



**Distribution A: Approved for public release; distribution unlimited.**

attained with zero initial curvature can be duplicated exactly for cylindrical initial curvature by offsetting the values of each thermal curvature term by the opposite of the respective initial curvature values. Thus, we see in Fig. 20 that the bistability regions are shifted along a thermal curvature axis by an amount opposite to the corresponding initial curvature.

This observation that initial curvature results in a linear shift of the bistable region concisely explains the effect of initial curvature on a shell's bistable behaviour in a graphical manner. Previously, design of bistable laminates was carried out on a trial and error basis, however this new design tool allows the analyst to tune the stability characteristics of their structure using a fairly simple graphical method.

The experimentally measured thermal curvatures are plotted as the dashed line in Fig. 20. This thermal curvature path starts at a point near the origin, which corresponds to the laminate's cure temperature. The fact that this path does not start coincident with the origin indicates the presence of non-thermoelastic strains at cure temperature. Proceeding to the right along the thermal curvature path, the magnitude of $\kappa_{\mathrm{T}x}$ grows much faster than the magnitude of $\kappa_{\mathrm{T}y}$, by a factor of approximately 3.5. This trend is due to the higher CTE mismatch of the metallic and composite layers in the fibre 0° direction relative to the 90° direction. Upon further cooling, the thermal curvature path intersects the bistability regions for $\hat{\kappa}_y = -2.0\,\mathrm{m}^{-1}$, $-2.5\,\mathrm{m}^{-1}$, and $-3.0\,\mathrm{m}^{-1}$. Snap-through upon cooling is predicted at points b, e, and f, respective to each initial curvature. The temperatures and shell curvatures corresponding to these points are indicated by the matching letters in Fig. 21. Upon re-heating, snap-through is predicted at points a, c, or d, respective to each initial curvature. Laminates of the presently investigated stacking sequence are not predicted to exhibit bistable or snap-through properties when they possess initial curvatures of lesser magnitude than approximately $-1.63\,\mathrm{m}^{-1}$, evidenced by the failure of the purple and dark blue regions to intersect the thermal curvature path. However, it can still be seen from Fig. 21 that even when this behaviour is not predicted, the resulting curvature-temperature relationship may still be highly nonlinear, especially for cases of initial curvature which nearly trigger bistable behaviour, e.g. $\hat{\kappa}_y = -1.5\,\mathrm{m}^{-1}$. Increasing the magnitude of initial curvature increases the magnitude of $\Delta T$ required to trigger snap-through, while also widening the temperature range over which bistability exists. This behaviour can be visualised in Fig. 20, where shifting a given region upwards results in a rightwards shift of the points where the thermal curvature path intersects this region.



**Distribution A: Approved for public release; distribution unlimited.**

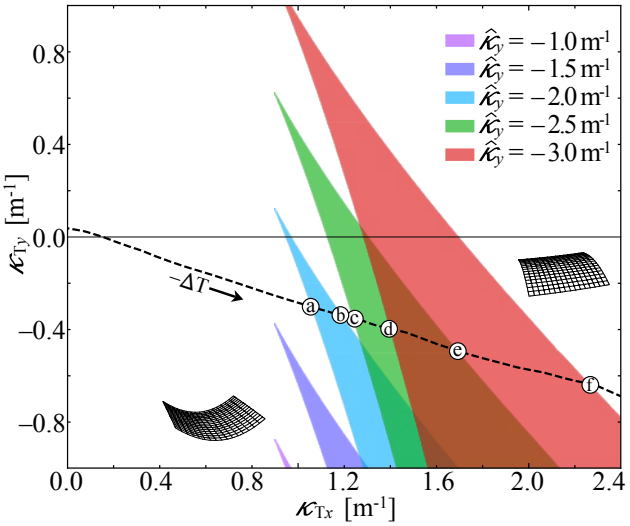



Figure 20: Stability phase diagram showing combinations of thermal curvatures $\kappa_{\mathrm{T}x}$ and $\kappa_{\mathrm{T}y}$, and initial curvatures $\hat{\kappa}_y$ which yield bistable behaviour, denoted by coloured regions. The dashed line represents the path of thermal curvatures plotted in Fig. 19, while the circular markers denote snap-through points passed upon heating or cooling for various initial curvatures. The temperature and curvatures at snap-through initiation are indicated by the corresponding letters in Fig. 21. The shell illustrations adjacent to the regions represent the two stable shapes attained within each region, as well as the monostable shapes which exist outside each respective region boundary.



**Distribution A: Approved for public release; distribution unlimited.**

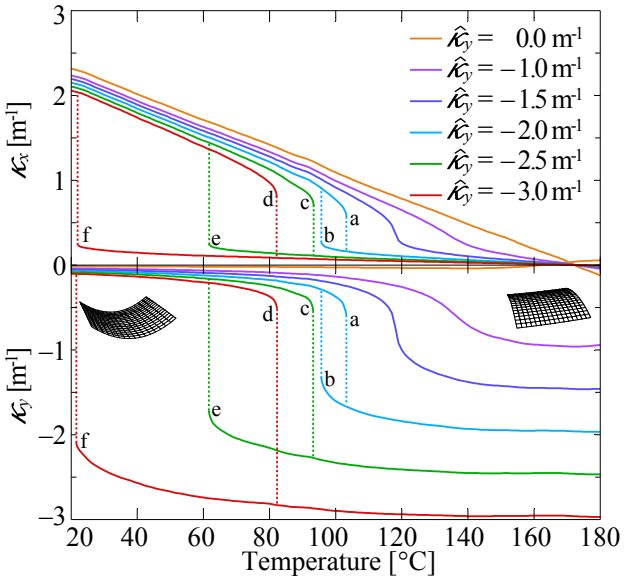



Figure 21: Analytical results showing predicted effect of initial curvature upon hybrid laminate response to thermal loading. Vertical dotted lines represent snap-through paths. The cure temperature is 180°C, and thus the magnitude of thermal loading increases for decreasing temperatures.

### 3.4.3 Model Predictions of the Laminate's Response to Thermal Loads

Results for the fibre-metal hybrid laminated shell and beam specimens described in Table 3 are given in Fig. 22. The thermal curvature changes measured in the 0° and 90° strip specimens are superimposed upon the initial curvatures of the plate in their respective directions to yield the plate's *natural curvatures* $\kappa_{\mathrm{N}i}$, defined explicitly as $\kappa_{\mathrm{N}i} = \kappa_{\mathrm{T}i} + \hat{\kappa}_i$. Thus, the dashed lines indicate the curvature that the initially curved shell would achieve if not for geometric nonlinearity. As our shell has zero Gaussian curvature in its initial state, and because its thinness makes it relatively stiff in membrane stretching relative to bending, it tends to conserve Gaussian curvature as thermal loads are applied. That is to say that in this case, it always tends to have at least one principal curvature be zero, or at least nearly zero. This supposition is verified by both analytical and experimental data, which show that regardless of temperature, at least one of the shell curvatures, $\kappa_x$ or $\kappa_y$, is nearly zero.

As the shell is cooled from its cure temperature to 100°C, the analytical and experimentally predicted $\kappa_x$ quickly diverges from $\kappa_{\mathrm{N}x}$. This response is due to the role of initial curvature, which stiffens the laminate against the internal bending moments via development of membrane strain, as the laminate had to develop nonzero Gaussian curvature in



**Distribution A: Approved for public release; distribution unlimited.**

order to incur a change in $\kappa_x$. Meanwhile, $\kappa_y$ is also nearly constant while cooling to 100°C, despite the increasing magnitude of $\kappa_{\mathrm{N}y}$. The apparent inertness to thermal loading is a result of competition between the thermally induced moments along the $y$-direction, and Brazier loads induced by much greater thermal moments along the $x$-direction. Effectively, the shell's tendency to respond to changes in $\kappa_{\mathrm{T}y}$ with additional curvature magnitude is approximately balanced by the curvature reduction induced by the shell's tendency to collapse towards its neutral axis on account of the much greater bending moment along the $x$-direction. When cooled further, the Brazier loads eventually out-compete the moments induced by $\kappa_{\mathrm{T}y}$, and the result is a snap-through change of shape to a cylinder with principal curvature oriented along the $x$-direction. The analytical model predicted this event to take place upon cool-down through 61°C.

The motivation for a transition to major curvature in the $x$-direction can also be viewed from an energy minimization perspective. By observing Eq. (11), we can see that potential energy scales linearly with the laminate stiffness terms, but quadratically to the mismatch between the terms of the $\Delta\boldsymbol{\kappa}$ and $\boldsymbol{\kappa}_{\mathrm{T}}$ vectors.[9] Thus, we deduce that stable shapes have this curvature mismatch preferentially minimised along the stiffest direction. In other words, we expect that after some degree of thermal loading, the laminate develops curvature in similar orientation and magnitude to the thermal curvature component of greatest magnitude, especially if this component corresponds to the same direction for which flexural stiffness is maximised. This basic explanation neglects the membrane strain terms, and unsurprisingly, we see that it breaks down in the temperature range where the shell's initial curvature restricts curvature development in the orthogonal direction, on account of the significant role that membrane effects play under these conditions.

Below the cooling snap-through temperature, $\kappa_y$ is almost entirely suppressed by dominate $\kappa_x$. With further cooling, $\kappa_x$ continues to grow at an approximately linear rate. Upon heating from room temperature, the shell curvatures initially retrace their cooling paths, however now their heating snap-through temperature is markedly offset from the cooling snap-through temperature. Both experiment and analysis show the heating snap-through to take place at 93°C, at which point the laminate reverts back to its initial shape. Both $\kappa_x$ and $\kappa_y$ remain approximately constant throughout the remaining heating interval.

### 3.4.4 Experimental Results

The experimental results show two separate types of hysteretic behaviour, the first being due to geometrically nonlinear effects, while the second is likely due to material nonlinearity.

[9] This relationship is analogous to the equation for strain energy density stored in a body under uniaxial load, $\Pi = \frac{1}{2}E\epsilon^2$.



**Distribution A: Approved for public release; distribution unlimited.**

With regards to the first, because the heating and cooling snap-through temperatures are separated by a gap of 22°C, the laminate displays clear *deadband hysteresis.* This behaviour is similar to that displayed by prebuckled bimorph beams [11], such as those used in thermostats and circuit breakers. Effectively, our laminate achieves this sort of behaviour by buckling under its own thermal stresses, as opposed to relying upon constraining boundary conditions as is the case for prebuckled beams. This behaviour suggests that snap-through laminates may be particularly useful for passive thermal control applications, where a degree of deadband hysteresis is desirable to avoid chatter behaviour. From a design standpoint, the width of the temperature deadband may be tailored by adjusting the initial curvature, as demonstrated by Fig. 20. The deadband range scales with the length of the intersection between the dashed line and a given bistable region in that figure. Changes to the laminate's constitutive properties and planform shape also impact the deadband range.

The second type of hysteresis occurs at higher temperatures, and is responsible for the mismatch between the heating and cooling values of $\kappa_y$ measured above 93°C. Bearing in mind that the experiment featured a heating ramp followed by cooling, we observe $\kappa_y$ to be slightly higher upon cooling than heating. Some clues to this behaviour are offered if we recall that the $y$-direction internal thermal moment (and its associated thermal curvature) are driven by CTE mismatch between the aluminium and 90° composite layers. Given that the 90° material properties are matrix-dominated, we can hypothesise that viscoelastic stress-relaxation of the polymer matrix, or potentially drying of residual moisture content within the matrix may be at play. The focus on matrix properties is supported by the fact that there is no similar hysteresis observed in $\kappa_x$, whose behaviour is expected to be a result of fibre-dominated properties instead.

Between the heating and cooling snap-through temperatures, the laminate is bistable, and may be snapped from one cylindrical orientation to another by application of external forces.

### 3.4.5 Comparison of model predictions with experimental results

The analytical model showed excellent correlation with experiment below the cooling snap-through temperature. Above the heating snap-through temperature, the model failed to predict the aforementioned material hysteresis, resulting in error of $\kappa_y$ prediction of up to 24%. The model had mixed results predicting the snap-through temperatures of the laminate, with the cooling snap-through prediction diverging from experiment by 9°C, although the heating snap-through was predicted accurately. It is likely that the seemingly accurate prediction of the heating snap-through temperature is at least partly due to coincidence, and that what we are actually observing is a lucky cancellation of errors in both the prediction of the range and midpoint temperature of the bistability temperature range. In other words



**Distribution A: Approved for public release; distribution unlimited.**

the model's deadband hysteresis loop is not only too wide, but also offset slightly in terms of temperature from the experimental results, such that the two heating snap-through temperatures happen to be coincident. The model's overprediction of the deadband range indicates that it is overestimating the thermal loads required for snap-through. This observation is in agreement with the work of Pirrera *et al.* [25] and Lamacchia *et al.* [33], who show that the constant curvature shape functions used in this work overconstrain the laminate's kinematics during snap-through transitions, compared to models with more degrees of freedom.

Should such a class of laminate be implemented as an actuation device, the designer will most likely be concerned primarily with $\kappa_x$ rather than $\kappa_y$ on account of the fact that both stiffness and curvature generation capability of the laminate are maximised along the $x$-direction. In this case, the model's predictions of $\kappa_x$ are generally quite accurate.

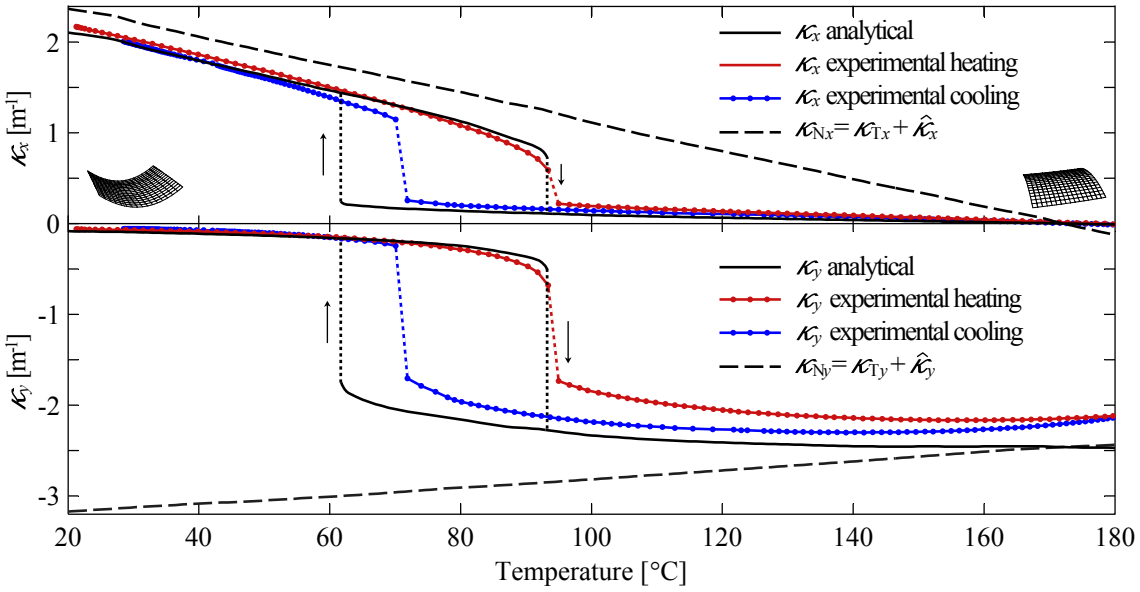



Figure 22: Experimental results of shell curvatures compared to model predictions for the laminate described in Table 3. Vertical dotted lines represent snap-through paths, which proceed along the direction indicated by arrows.

### 3.4.6 Observations Regarding Stability Near Snap-Through Temperatures

When bimorphs were thermally loaded to near their snap-through temperature, even small external loads could trigger a snap-through. This result is not surprising, as a snap-through is triggered by loss of stability, and intuitively, one would expect that a situation of marginal



**Distribution A: Approved for public release; distribution unlimited.**

stability would precede this loss of stability. This observation was made by manually handling composite bimorphs near their snap-through temperature, where it was found that the force required to transition the laminate between stable shapes was very small near each respective snap-through temperature.

# 4 Thermally Driven Morphing With High-Temperature Composites

One of the greatest appeals to thermal morphing concepts is their ability to potentially function in extreme environments, particularly those too hot for conventional actuation systems. To recap, large performance gains in gas turbine engines could be obtained by utilizing variable-geometry hot structures. At present, this goal has proven elusive due to the very hostile environment, which precludes the use of conventional linkages, hinges, and bearings for motion control. Flexure-hinges present a potential solution to this problem, in that they are not susceptible to seizure, galling, or free-play. We would still require an actuator of some sort, and current hydraulic and servo-electric actuators are limited to approximately 200°C [3], well below the ambient temperatures experienced in the hot section of a gas turbine.

Thermal expansion actuation, on the other hand, can be accomplished at much higher temperatures, as it is only limited by thermal degradation of material properties. The use of nickel-based superalloys can theoretically allow operation at temperatures in excess of 1000°C. By utilizing a thermal bimorph arrangement, the actuator and flexure hinge can be combined into one.

A high-temperature bimorph essentially has four materials selection requirements:

1. Two materials must be selected which have mismatched CTEs.
2. These two materials must be joinable by some means.
3. These two materials must not yield or otherwise experience unrecoverable deformations up to the maximum temperature for a particular application. This work seeks materials suitable for use above 500°C.
4. Ideally, at least one of the materials should display anisotropic elastic and expansion properties, such that the directionality of the thermal moments may be controlled.



**Distribution A: Approved for public release; distribution unlimited.**

High-temperature-capable alloys can be selected which meet all but the last requirement. For example, high-CTE austenitic stainless steel can be laminated via cold-welding to ferritic stainless steel, which has a somewhat lower CTE. This material combination is the basis for certain commercially available, high-temperature bimetals, for which a maximum operating temperature of 500°C is specified [34]. Should we wish to satisfy the fourth requirement mentioned above, we need to utilise some sort of high-temperature composite material. Besides allowing us to tailor the thermal moments, the use of composite construction may also allow us to obtain a greater mismatch of CTEs between layers, as composites based on carbon and or silicon carbide fibres generally have much lower CTEs than nearly all engineering alloys.

Polymer matrix composites have been developed to enable continuous use up to 300°C [35], however above this temperature, we must turn to certain varieties of MMCs and CMCs. This work explores methods of creating thermal bimorphs from these high-temperature composites paired with metallic alloys. The main challenge in this work lies in the materials and processing challenges presented by such exotic material systems. The following two sections discuss the development of MMC and CMC-based thermal morphing structures, with later sections addressing experimental testing and results.

## 4.1 Metal Matrix Composites: Materials and Processing

Metal matrix composites come in many varieties, depending on matrix and reinforcement material, form, and processing method. The choice of matrix and reinforcement is highly driven by manufacturing considerations, as it is very challenging to achieve a consolidated, void-free composite while not also damaging the reinforcement, especially in the case of continuous fibre reinforcement. The chief problem is that in order to consolidate the composite, a given matrix metal must be heated to near or above its melting temperature in order to flow around the reinforcement, however at this temperature, the fibres, whiskers, or particles themselves are liable to chemically react with the metal [36]. Casting molten steel around carbon fibres, for example, would merely result in an ingot with localised regions of iron carbide ($Fe_3C$) and graphite inclusions where fibres used to reside. This inherent difficulty can be addressed by choosing low-melting-point matrix metals such as aluminium alloys, however this material choice would limit the useful temperature of such an MMC to less than 300°C, much too low for gas turbine applications. An alternate approach is to adopt a matrix material which can be hot-formed in the solid state around the fibres, such as titanium, which allows the matrix to be consolidated at a temperature less than its melting point, and thus reducing adverse reactivity with the fibres. Reactivity can be further reduced by selecting more chemically stable reinforcements, thus silicon carbide fibres are



**Distribution A: Approved for public release; distribution unlimited.**

often chosen over carbon fibres for high-temperature applications.

Titanium matrix composites reinforced by continuous silicon carbide (SiC) fibres are commercially available in the UK, and possess a number of properties well suited to thermal bimorph construction. In particular, they have a low CTE along the fibre direction ($6.6 * 10^{-6}/°C$), high modulus (205 GPa), and can be readily diffusion bonded to various titanium alloys, thus offering a reliable method of joining the low-expansion MMC layer to a high-expansion metallic layer. In addition, the MMC's CTE perpendicular to the fibres is nearly matched to that of its parent alloy, which ought to result in near-unidirectional moments. This feature may be useful in cases where the designer wishes to generate curvature along one direction only, regardless of the planform shape of the laminate.

Two types of MMC-based bimorphs were fabricated for evaluation. The first, which is described in Section 4.1.1, utilises the aforementioned SiC fibre, titanium matrix MMC as the low-expansion element, and employs a titanium alloy as the high-expansion element. The second concept, described in Section 4.1.2, is similar to the first, but uses a layer of 304 stainless steel as the high expansion element in place of the titanium alloy layer. Selected thermoelastic properties of the materials used for the MMC-based bimorphs are shown in Table 5.

Table 5: Thermoelastic material properties for the MMC-Ti and MMC-304SS bimorphs. Properties are given at room temperature unless otherwise stated.

| | $E_1$ or $E$ [GPa] | $E_2$ [GPa] | $\alpha_1$ or $\alpha$ $[\frac{10^{-6}}{°C}]$ | $\alpha_2$ $[\frac{10^{-6}}{°C}]$ |
|---|---|---|---|---|
| SiC/Ti-3Al-2.5V MMC [37, 38] | 205 | 150 | 6.6 (0-700°C) | 9.3 (0-700°C) |
| Ti-3Al-2.5V [39, 32] | 100 | | 9.6 (0-100°C) | |
| | 80 (230°C) | | 10.0 (0-540°C) | |
| | 55 (500°C) | | | |
| AISI Type 304 SS [32] | 195 | | 17.1 (0-200°C) | |
| | 127 (800°C) | | 19.4 (0-800°C) | |

### 4.1.1 MMC-Ti Bimorphs

The first bimorph type is a laminate in which the low-expansion layer is constructed from a unidirectionally reinforced titanium-matrix composite, and the high-expansion layer is of monolithic titanium alloy. Fabrication was carried out by TISICS Inc., Farnborough, UK. The reinforcing fibres are SM3156 SiC monofilaments, which are produced in-house by



**Distribution A: Approved for public release; distribution unlimited.**

TISICS via chemical vapour deposition of SiC on a tungsten filament.[10] Both the composite matrix and monolithic layer are commercially available Ti-3Al-2.5V alloy. The low-expansion MMC layer was laid up by stacking alternate layers of 140 $\mu$m titanium foils and binder-bound SiC monofilaments, as illustrated in Fig. 23. The high-expansion monolithic layer is formed from the same titanium foils stacked to the required layer thickness. The complete layup was encapsulated in a welded stainless steel canister in preparation for consolidation. The binder was then vaporised, followed by evacuation and sealing of the canister. Consolidation was achieved by hot isostatic pressing (HIP). The exact HIP cycle parameters are propitiatory to TISICS, however publicly available literature indicates that a chamber pressure of 70-90 MPa, temperature of 900°C, and and hold time of 30 minutes is typical for this material system [40]. After completion of the HIP cycle, the compacted canister was cut open and the consolidated laminates extracted and cut into 0° and 90° fibre-orientation beam specimens by wire electro-discharge machining. The HIPed laminate with beam specimens cut from it is shown in Fig. 24, while the dimensions of the specimens and their stacking sequences are shown in Table 6.

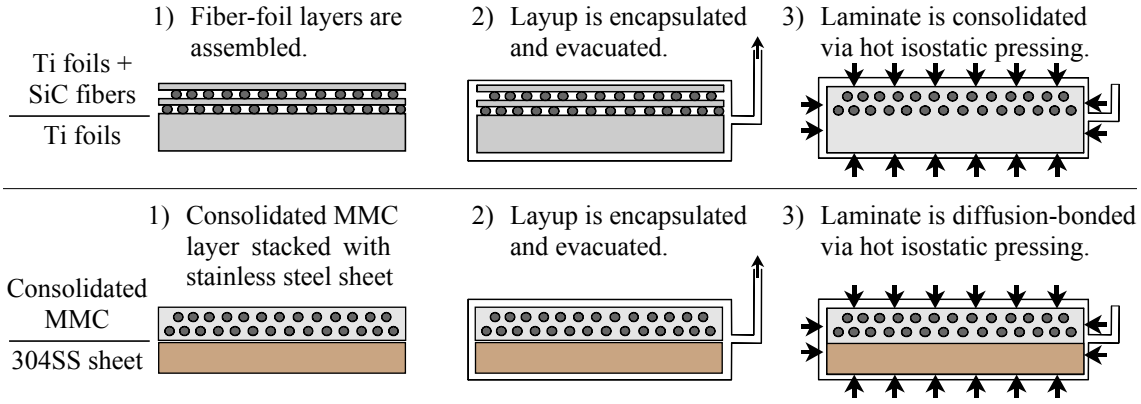



Figure 23: Manufacturing process used to create the MMC-Ti bimorphs (top) and MMC-304SS bimorphs (bottom).

[10]This tungsten filament is available commercially as a standard light-bulb filament.



**Distribution A: Approved for public release; distribution unlimited.**




Figure 24: Metal matrix composite bimorph laminate as it emerged from the HIP process (left), and after wire-EDM cutting into beam specimens (right).

Some specimens were mounted in epoxy and polished for cross-section micrograph analysis. The consolidated MMC-Ti bimorph laminates showed generally uniform fibre distribution and were free of voids, as shown in Fig. 25.

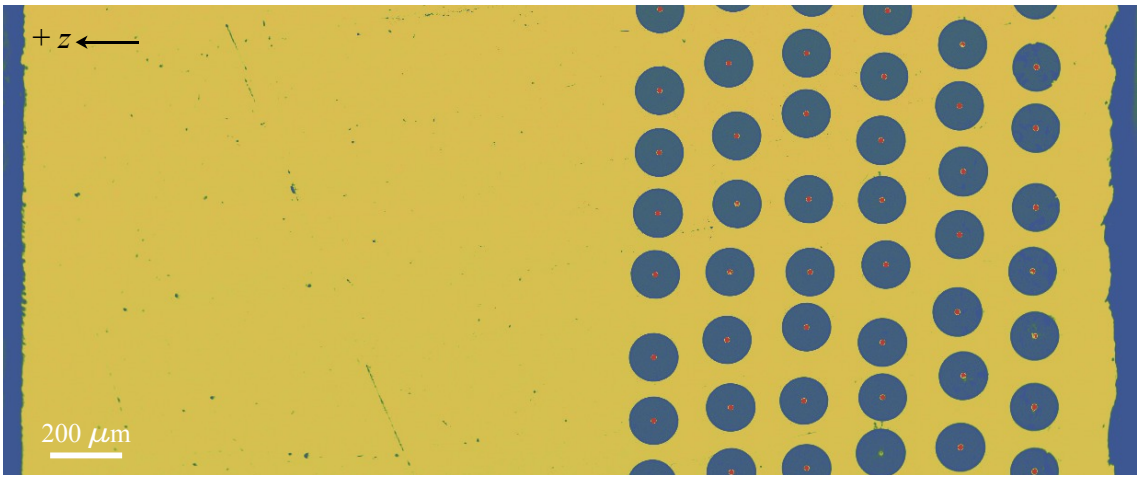



Figure 25: False-colour SEM micrograph of MMC-Ti laminate cross-section. The red dots at the centre of each fibre are the tungsten filaments upon which the fibre is grown. Note that the image is perpendicularly oriented to the sketches in Fig. 23.



**Distribution A: Approved for public release; distribution unlimited.**

Table 6: Manufacturing specifications for MMC bimorphs.

| Test Article Name: | MMC-Ti 0° | MMC-Ti 90° | MMC-304SS 0° | MMC-304SS 90° |
|---|---|---|---|---|
| **Layup**: Ti = Ti-3Al-2V foil SiC($x$°) = SiC fibre ply oriented at $x$° SS = 304SS sheet | [ $Ti_{13}$/ $(SiC(0°)/Ti)_6$] | [ $Ti_{13}$/ $(SiC(90°)/Ti)_6$] | [$SS_1$/$Ti_1$/ $(SiC(0°)/Ti)_6$] | [$SS_1$/$Ti_1$/ $(SiC(90°)/Ti)_6$]] |
| **Planform Dims** [mm] | 90 x 10 | 90 x 10 | 90 x 10 | 90 x 10 |
| **Composite layer total thickness** [mm] | 1.48 | 1.48 | 1.61 | 1.61 |
| **Monolithic layer total thickness** [mm] | 1.67 | 1.67 | 1.44 | 1.44 |

### 4.1.2 MMC-304SS Bimorphs

The second type of MMC bimorph features the same low-expansion MMC layer as the first, while the high expansion layer is a 1.6 mm sheet of AISI 304 stainless steel (304SS). This material choice was motivated by the higher displacements and moments achievable by increasing the CTE mismatch between layers. Austenitic stainless steels provide the highest CTE of heat-resisting engineering metals, and thus the MMC-304SS bimorph possesses a CTE mismatch approximately 3.6 times greater than the MMC-Ti bimorph in the fibre direction. Despite this potential for performance gain, there was still a question of whether 304SS could be reliably joined to the MMC layer. No prior literature could be found on MMC-stainless steel joining methods, however a few publications regarding the joining of titanium alloy to stainless steel were uncovered [41, 42, 43]. These works indicated that diffusion bonding gave satisfactory results, so long as the formation of Fe-Ti intermetallics could be kept in check.

Diffusion bonding is a joining process whereby the surfaces to be joined are pressed together at high pressure and high temperature, such that metallic bonds form between the two on account of interatomic diffusion. This process requires the surfaces to be exceptionally clean and free of oxide contamination, and be close fitting such that the surfaces are in intimate contact with each-other. As long as the atoms of each surface are brought close enough together and heated enough to encourage atomic mobility, a metallic bond is formed, consisting of metallic solid solutions and intermetallic compounds. The formation of the latter is undesirable in the Fe-Ti system, as these intermetallic compounds (FeTi, $Fe_2Ti$, etc.) are brittle and adversely affect the joint strength [43]. In order to minimise intermetallic formation, the diffusion bonding temperature and time duration must be minimised. The



**Distribution A: Approved for public release; distribution unlimited.**

trade-off is that if the bonding temperature and time is too low, the diffusive processes used to form the bond are inhibited such that the bond may not form in the first place. Thus, a balance of diffusion bonding time and temperature is desired [41], for which the cited authors recommend a diffusion bonding temperature of 850°C, held for 60 minutes. These parameters were utilised in the course of the diffusion bonding efforts and found to be generally satisfactory.

Interlaminar peel stresses scale with CTE mismatch at the interface, consequently these deleterious stresses can be reduced by inserting an interlayer material with an intermediate CTE [44]. To that end, an additional 140 $\mu$m titanium foil was inserted between the MMC and 304SS layers in order to reduce the likelihood of delamination due to bond-line peel stresses.

The MMC-304SS laminate was constructed in two HIP cycles. The first cycle consolidates the MMC layer alone using the same HIP cycle as the MMC-Ti bimorph, while the second HIP cycle diffusion bonds the stainless steel layer to the consolidated MMC using the same cycle parameters again, apart from a lower temperature of 850°C. This work also investigated the possibility that the laminate could be consolidated and diffusion bonded in the same HIP cycle, as the two cycles had similar temperature and hold time values. However when this technique was trialled by TISICS, it resulted in partial debonding between the MMC and stainless steel layers, as shown in Fig. 26. Energy dispersive X-ray (EDX) analysis as well as previous literature [42] suggests the $\sim$ 50°C higher HIP temperature needed to achieve complete composite MMC consolidation over that recommended for diffusion bonding, resulted in a degradation of bond strength on account of excessive Fe-Ti intermetallic formation at the bond line. However as previously indicated, diffusion bonding the stainless steel layer in a separate HIP cycle was satisfactory.



Figure 26: Attempting to consolidate the MMC layer and diffusion bond the stainless steel layer simultaneously resulted in a partial debond of the interface.



**Distribution A: Approved for public release; distribution unlimited.**

The resulting MMC-304SS laminates exhibited consistent fibre spacing and void-free bond line, as shown in Fig. 27. An EDX analysis was carried out in order to determine the composition of the diffusion-bonded interfacial layer. The results, shown in Fig. 28, indicate that the interfacial layer comprises Fe-Ti solid solutions and intermetallic compounds. EDX analysis has limited ability to determine the types of intermetallic compounds present, however prior literature suggests that the main constituent compounds are brittle FeTi and $Fe_2Ti$ intermetallics. This brittle layer did not give any trouble in the course of experiments, though prior workers have addressed the brittle interface problem through use of a copper interlayer, which also functions as both a diffusion barrier and a ductile interface [43].

The MMC-304SS specimens were cut by wire-EDM to the orientations and dimensions shown in Table 6.

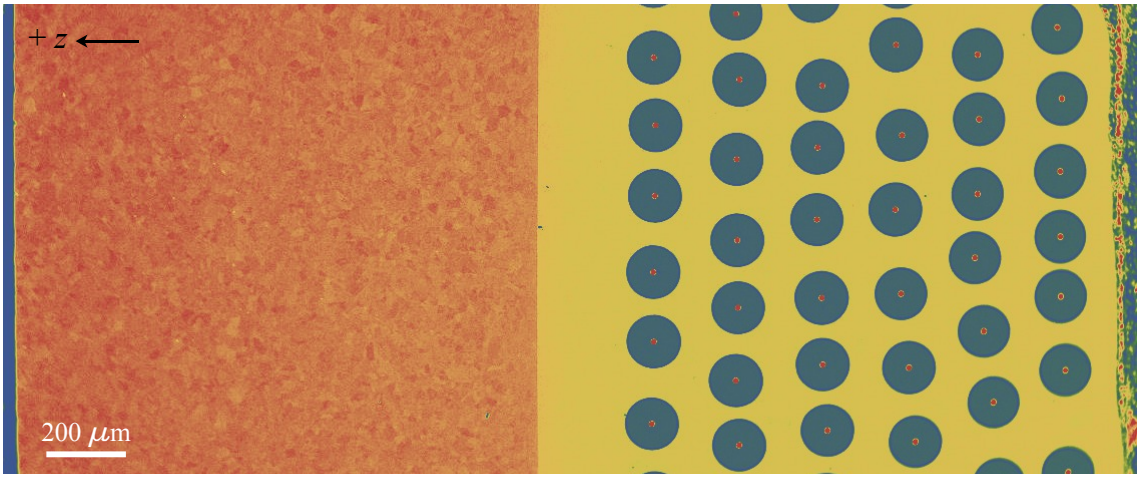



Figure 27: False-colour SEM micrograph of MMC-304SS laminate cross-section. The dark orange volume is the 304SS layer, within which the relatively large grains of austenite can just be discerned.



**Distribution A: Approved for public release; distribution unlimited.**

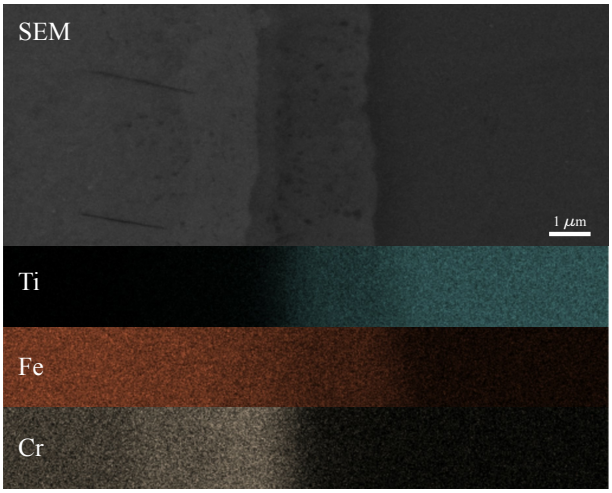



Figure 28: SEM micrograph and overlaid EDX K-shell emission densities of the MMC-304SS diffusion-bonded interface, showing a void-free bond with a reaction layer of Fe-Ti compounds. Other major alloying elements were not present in significant concentrations in the reaction layer. This imagery was obtained by Peter Martin at the University of Bristol Interface Analysis Centre.

## 4.2 Ceramic Matrix Composites: Materials and Processing

Ceramic matrix composites (CMCs) combine strength at elevated temperatures with very low CTEs, which makes them excellent candidates for use as the low-expansion element of a thermal bimorph. The high expansion element could be any number of heat-resisting stainless steels or nickel-based superalloys, either would provide a generous CTE mismatch.

### 4.2.1 Ceramic Matrix Composite Manufacturing at The University of Bristol

Carbon fibre, silicon carbide matrix composite panels were manufactured at the University of Bristol via the polymer infiltration and pyrolysis (PIP) process, which is outlined in Fig. 29.



**Distribution A: Approved for public release; distribution unlimited.**

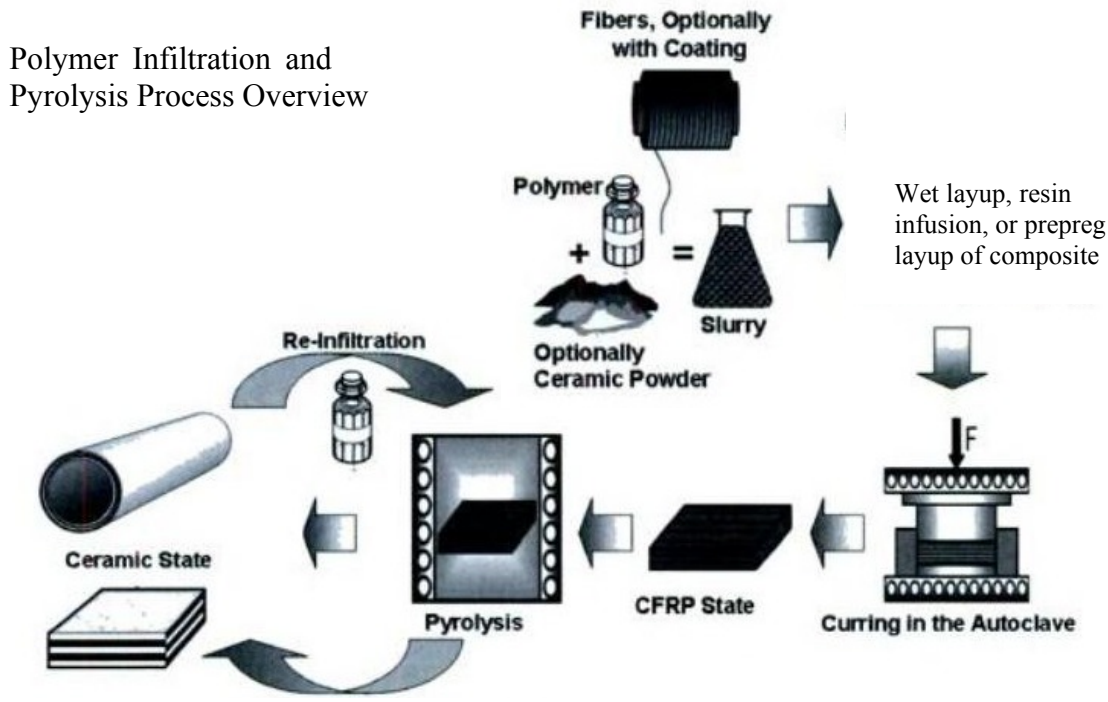



Figure 29: The polymer infiltration and pyrolysis process. Adapted from Krenkel *et al.* [45]

**Raw Materials Selection and Sourcing** A combination of intermediate modulus unidirectional (UD) carbon fibre IM7 and woven T300 6-harness satin fabric was selected for use, with the goal of constructing a laminate with thermoelastic properties as near to UD as practically achievable. In order to obtain a fibre-matrix interface which promotes tough composite behaviour, the fabric was coated with a 0.7 $\mu$m thick layer of pyrolytic carbon (PyC) by Archer Technicoat (High Wycombe, UK). As shown in Fig. 30, the coating thickness distribution was not uniform, instead tending to build up thicker on the outsides of fibre bundles, which presumably were exposed to a greater flow rate of gas during the CVI process. Ideally, one would coat the fibres before they are woven into fabric in order to achieve a uniform coating thickness, however such an approach would have been cost-prohibitive. Nonetheless, the results of fabric coating were found to be satisfactory in that the resulting CMC strength was sufficient for our purposes.



**Distribution A: Approved for public release; distribution unlimited.**

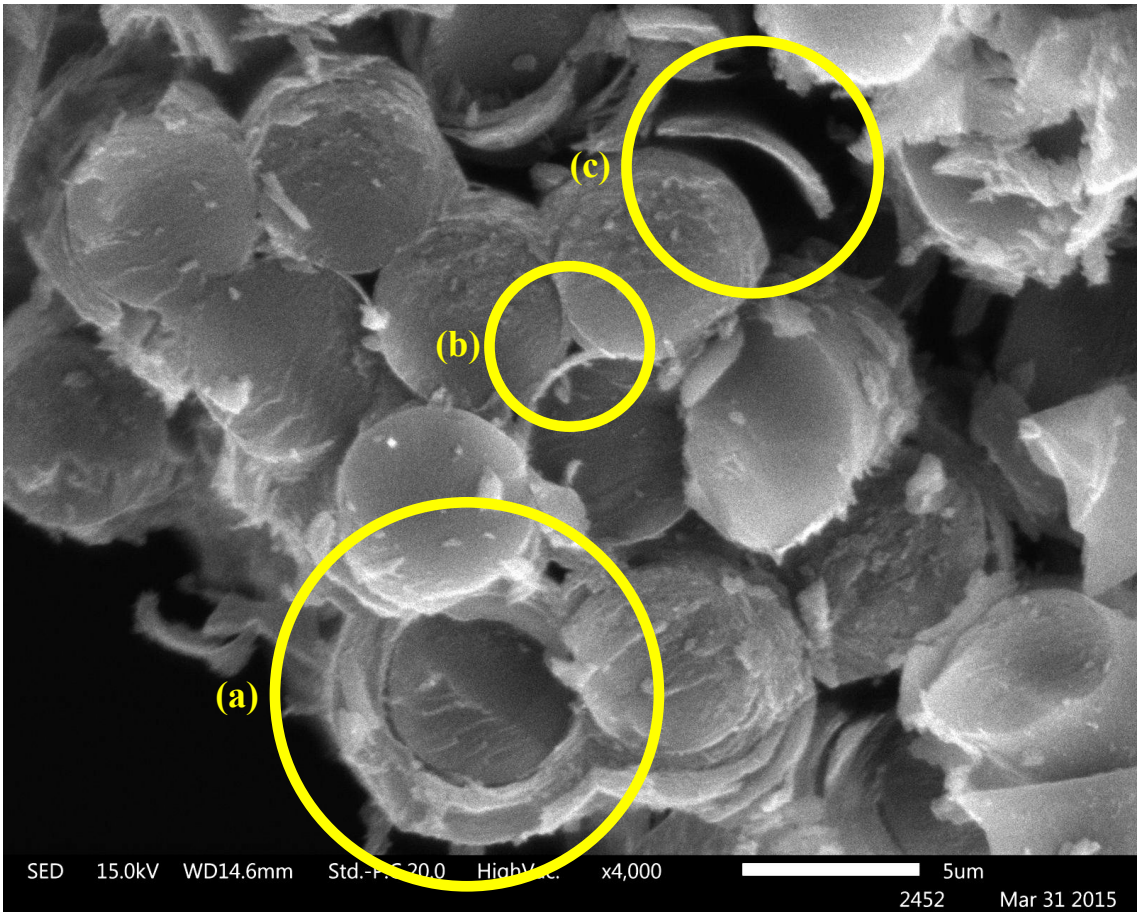



Figure 30: SEM imagery of PyC-coated carbon fibres.
a) Coating thickness was greater on surfaces on the outside of the fibre tow.
b) Coating thickness was lesser on closed-off surfaces.
c) This piece of chipped-off coating is representative of the average coating thickness attained.

SiC matrix precursor polymer was acquired from from Starfire Systems, of Schenectady, NY, USA. Their polymer is allyl hydrido polycarbosilane (AHPCS), which they market under the trade name SMP-10.

**Fibre Desizing** Commercially available dry carbon fibres were used in this work, however such fibres are usually supplied with a size coating intended to aid bonding with polymer matrices. In order to avoid adversely affecting the ceramic precursor polymer chemistry during pyrolysis, it is customary to remove this coating by either chemical washing or heat



**Distribution A: Approved for public release; distribution unlimited.**

treatment [46]. As the heat treatment method only requires an inert gas furnace, this technique was pursued, as the necessary inert gas furnace was already available. The basic procedure is to place the dry fibres in the retort furnace, heat to 600°C, hold for one hour, and cool back to room temperature, a process which vaporises and chars the size coating. Heat treating of dry woven carbon fabric was a straightforward process, with no problems or unexpected issues encountered.

However, in the case of UD carbon non-crimp-fabric (NCF), one minor issue was encountered. While woven carbon fabric is held intact by the mutual binding effect of the interwoven tows, dry unidirectional fibres require some other means of binding. Typically, this is accomplished by weaving in a small number of nylon fibres at 90° to the carbon fibres. This procedure yields a non-crimp fabric, so-called because the fibre-crimping effects of conventional woven fabrics are avoided. Unfortunately, the heat treatment embrittled (or somehow damaged) the nylon tows, such that they fractured under only light manual handling. As seen in Fig. 31, this binder embrittlement resulted in a fabric which tended to fall apart into its individual carbon tows during layup. The workaround solution was to be extremely careful when handling these plies, and when necessary, manually reassemble the separated tows in the course of the layup. In future work, it would likely be preferable to utilise a highly biased fabric such as the 5:1 plain weave depicted in Fig. 32. This type of fabric would approximate UD properties, but would still remain durable and easy-to-handle after heat treatment, as carbon instead of nylon fibres are used to keep the fabric intact.

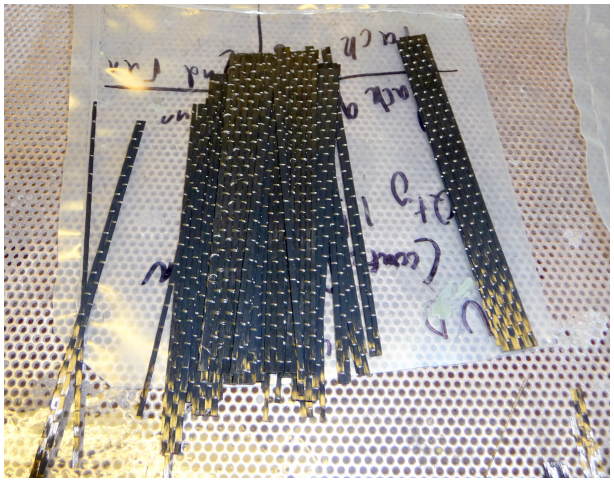


Figure 31: Dry carbon NCF fabric in the post-heat-treated state. The heat treatment process has damaged the nylon weft yarns, such that they no longer are able to hold the fabric intact.



**Distribution A: Approved for public release; distribution unlimited.**

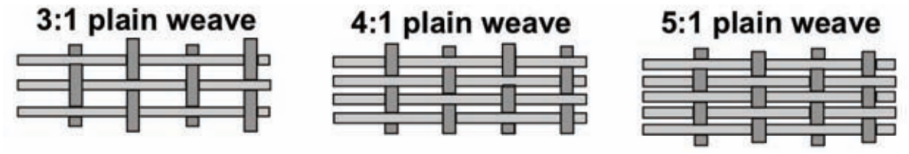



Figure 32: Three fabrics with progressively greater weave bias. Graphics adapted from D Glass, 2008 [47].

**Initial Polymer Infiltration: Wet Layup and Hot Press Cure** The hot-pressing process requires the plies to be wetted out manually as they are stacked. This process, known as wet layup, is common in composite manufacturing, mainly due to its ease of use and flexibility. Figure 33 shows four laminates, having gone through wet lay-up followed by stacking on a tool plate. A second tool plate was placed atop the laminates, and the assembly was hot pressed at 220°C for one hour, with a consolidation pressure of 500 kPa. The resulting green bodies were of superior quality to the VARTM laminates, with no visible porosity. Fibre volume fractions varied between 59-64 % over four panels.



Figure 33: The wet lay-up workspace. The stacked laminates are arranged on the hot press tool plate at left, while additional dry fabric, slurry, and spreading tools occupy the centre of the frame. The grey colour of the laminates is due to SiC particulate filler added to the AHPCS polymer, which was successfully trialed in order to reduce matrix porosity after pyrolysis.

Trials were also undertaken to determine the effect of consolidation pressure on fibre volume



**Distribution A: Approved for public release; distribution unlimited.**

fraction. Usage of 100 kPa tool pressure resulted in a fibre volume fraction of 34-40% over four panels, some 20 % less than the fibre volume fraction achieved with 500 kPa pressure. Interestingly, the effect of fibre volume fraction on strength, as determined by later tests, was not similar to that observed for polymer matrix composites. In general, higher fibre volume fractions did not lead to significantly increased strengths. This finding has been corroborated in a NASA memo [48], however it is not immediately clear what mechanism is at work. It is possible that higher fibre volume fractions hinder effective polymer infiltration after pyrolysis, thus increasing matrix porosity and consequently reducing matrix strength and load transfer ability, which in turn partially cancels the benefit of having more load-bearing fibres present.

**Use of SiC Particulate Filler** Trials were also undertaken to assess the potential benefits of using SiC particulate filler in the matrix polymer.The goal of this filler is to reduce post-pyrolysis matrix porosity by nature of the fact that the SiC particulate is already in ceramic form, and thus does not undergo further shrinkage during pyrolysis. Porosity was calculated by weighing the dry fibres and subsequent green bodies, which established the matrix volume of each laminate. By then weighing the laminates in their post-pyrolyzed state, their porosity could be estimated given an assumed density of the SiC matrix of $3.2\,\mathrm{g/cm^3}$. This is the known density of crystalline $\beta$-SiC, however as the matrix is primarily amorphous, its actual density is somewhat less than this figure. How much less is difficult to say, however as long as we pick a consistent figure, we still compute accurate porosity values in the comparative sense, though perhaps not in the absolute sense. As this work is only concerned with evaluating which process modifications improve porosity, a comparative evaluation is sufficient.

The results of the SiC particulate filler trials showed that the addition of $6\,\mu$m diameter $\beta$-SiC particles, loaded into the AHPCS polymer at 25 wt%, resulted in an average reduction in matrix porosity of 5 % after the first pyrolysis cycle. 3-point bend testing would later show that the filler slightly improved the strength of the CMC as well. In practice, 25 wt% was near the upper limit of filler that could be added before the slurry became difficult to handle. Specifically, the filler would tended to settle to the bottom of the slurry container, and needed to be frequently stirred. At higher than 25 % filler loading, the "cake" of filler that formed on the bottom of the container was quite viscous and difficult to re-mix into suspension. Other workers have found that 25 % filler loading is about the optimal for strength [49], so this seemed the best figure to go forward with.

**Initial Pyrolysis** Green bodies were stacked atop one another using ceramic stilt separators as shown in Fig. 34 and placed in the retort. Because some portion of each laminate is cantilevered off the edge of the ceramic separators, they are subject to a self-weighted



**Distribution A: Approved for public release; distribution unlimited.**

bending load during pyrolysis. Layups with all fibres oriented in the same direction tended to droop down along the direction perpendicular to the fibres. Apparently, the preceramic polymer, in the course of pyrolysis, can be permanently deformed by such small stresses as those imposed by gravitational loading. On the other hand, layups capped off with woven plies were not subject to this drooping issue. Drooping could be combated by stacking the laminates between stainless steel sheets, as shown in Fig. 34. Regardless, this stacking method proved unnecessary going forward, as the all-UD layup was found to be so weak in the off-fibre directions so as to preclude its use in any practical application, and thus was abandoned in favour of layups which featured at least some portion of woven plies.

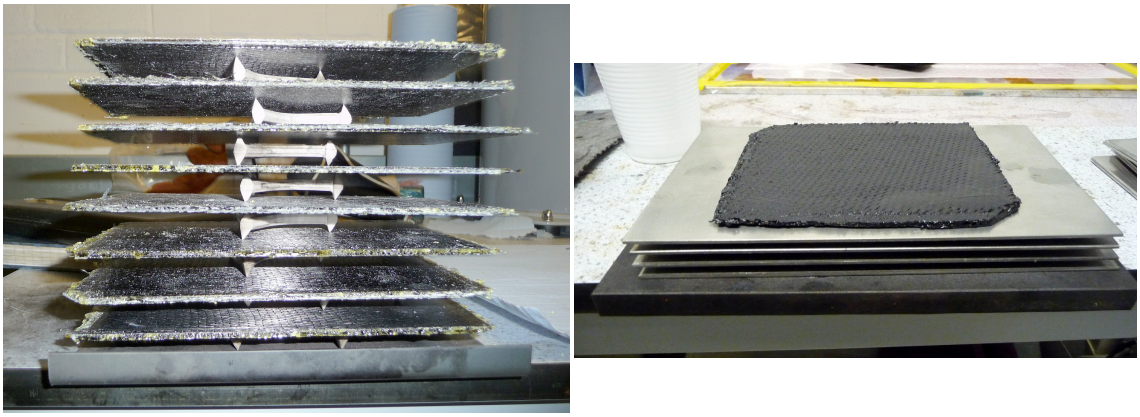


Figure 34: Laminates stacked using ceramic separators (left) and 310 stainless steel plates (right). The left photo shows laminates in green body form, while the right photo shows a pyrolysed laminate.

Pyrolysis was carried out in the aforementioned inert gas retort furnace, according to the temperature schedule given in Table. 7. This schedule, adapted from Starfire recommendations, is intended to allow pyrolysis within the course of the working day (as required by health and safety requirements), while ensuring that the ramp rate during the main pyrolysis stage is kept as low as possible. A low ramp rates is preferred as it minimises the rate at which hydrogen gas is evolved, which in turn reduces explosion risk as well as the risk of delamination due to gas trying to escape from between plies.



**Distribution A: Approved for public release; distribution unlimited.**

Table 7: Pyrolysis temperature schedule.

| Segment | Set Temp. [°C] | Ramp Rate [°C/min] | Total Segment Duration [min] | Comments |
|---|---|---|---|---|
| 1 | 200 | 7 | 26 | Initial rapid ramp until start of pyrolysis |
| 2 | 700 | 2 | 250 | Slow ramp through main pyrolysis temperature window to minimise hydrogen gas generation rate. |
| 3 | 910 | 4 | 53 | Fast ramp to finish pyrolysis |
| 4 | 910 | 0 | 45 | Hold at max temperature |
| 5 | 20 | Variable | Overnight, typ. 16 hrs | Furnace allowed to cool naturally overnight after shut-down. |

After pyrolysis, the laminates were removed from the retort furnace and trimmed using a diamond saw. This trimming process consisted of grazing the saw blade along the outermost edge of the laminate, removing about 0.5 mm of material, in order to open up access to internal porosity, which otherwise tends to be sealed off by the outermost layer of pyrolysed matrix.

**Polymer Reinfiltration and Further Pyrolysis** As is normal for the PIP manufacturing route, the pyrolysed laminates were reinfiltrated with AHPCS polymer. As shown in Fig. 35, this reinfiltration was accomplished by submerging the laminates in AHPCS, then placing the bath in a vacuum chamber. Drawing vacuum pulls air out of the pores in the laminate, allowing AHPCS polymer to infiltrate, as it no longer needs to displace any gas, thus allowing it to access "dead end" pores. Once air is removed from the laminate, argon gas is fed into the vacuum chamber until it is equilibrated with atmospheric pressure. This reintroduction of external pressure forces additional polymer into the pores and speeds along the capillary action process [48]. The use of argon gas as a back-filler, instead of air, prevents the polymer from being oxidised. This oxidation process, although slow at room



**Distribution A: Approved for public release; distribution unlimited.**

temperature, increases the polymer's viscosity, which in turn makes it slower to infiltrate.[11]

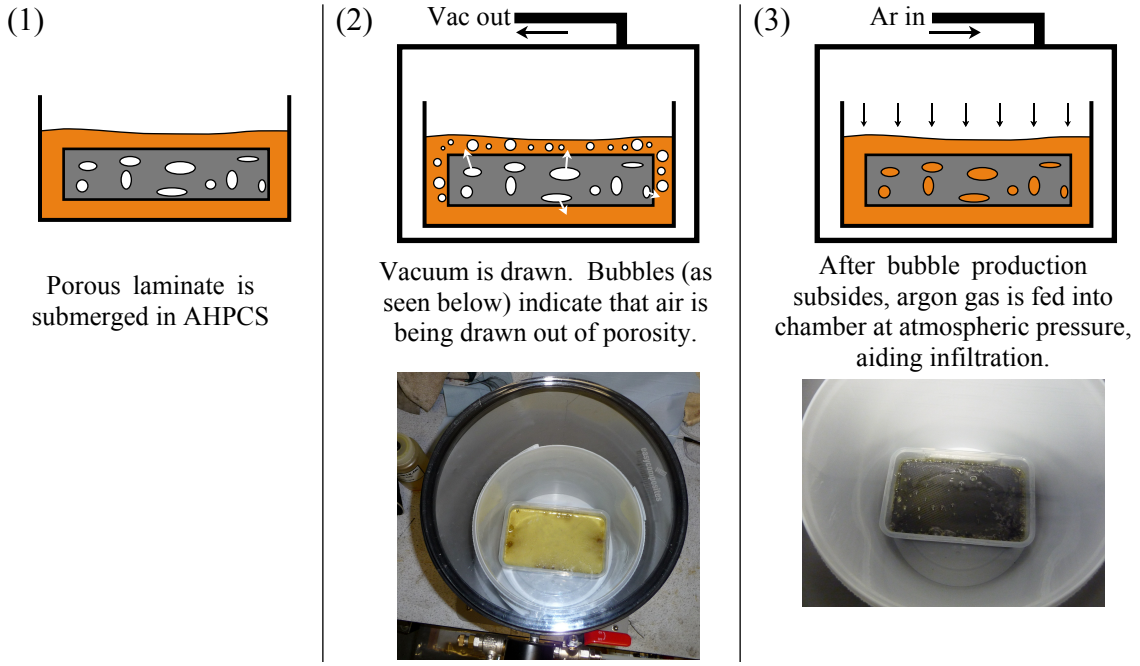



Figure 35: The polymer reinfiltration procedure. Photographs show the submerged laminates inside a vacuum chamber.

After the polymer has reinfiltrated the laminates, the panels are removed from the AHPCS bath and scraped with a spatula to remove excess polymer. The panels are then stacked and pyrolysed using the same temperature schedule as before. Typically, a thin layer of loose SiC particulate matter was present on the surface of the laminates after pyrolysis, as shown in Fig. 36. This particulate is likely the pyrolysed remains of excess AHPCS that was sitting on the surface of the laminates. It can be removed with a nylon brush, a procedure which was carried out after each pyrolysis cycle.

[11] In addition, the container in which the AHPCS is stored must be purged of oxygen to prevent oxidation of the polymer during long-term storage. Purging is accomplished with a simple gas tube and check-valve arrangement on the container lid which allows argon to be injected into the vessel. Keeping the polymer at $-20°$C also slows the oxidation process.



**Distribution A: Approved for public release; distribution unlimited.**

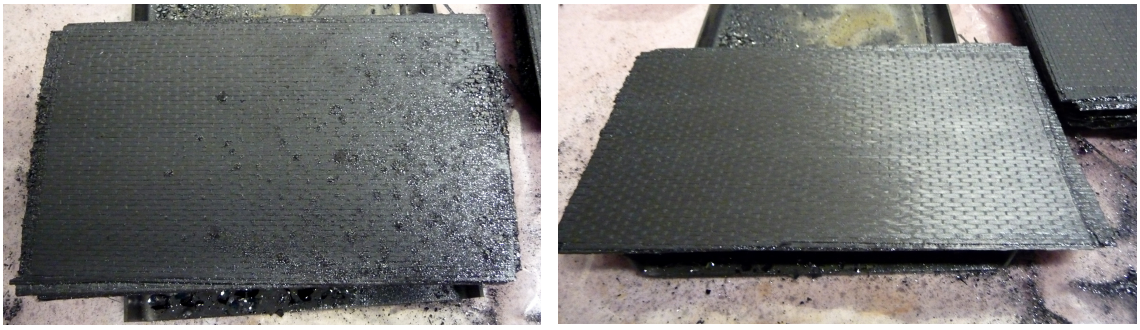


Figure 36: C/SiC panels immediately after pyrolysis (left), and after removal of SiC particulate matter (right).

**Flexural Strength Testing** CLT analysis indicated that in order to obtain meaningful displacements from a CMC-metal bimorph, a strain-to-failure of at least 0.2 % is required. Flexural 3-point tests were undertaken to assess the CMC's strain-to-failure. Nominal sample dimensions are given in Table. 8.

Table 8: Nominal sample dimensions for 3-point bend tests.

| Outer roller spacing | Thickness | Width |
|---|---|---|
| 90 mm | 3 mm | 20 mm |

Figure 37 shows flexural test results for CMCs with both the aforementioned PyC fibre coating, as well as uncoated fibres. Results showed that as long as the fiber coating was used, the flexural strength and strain to failure properties of our CMC are sufficient for use as thermal bimorph actuators.



**Distribution A: Approved for public release; distribution unlimited.**

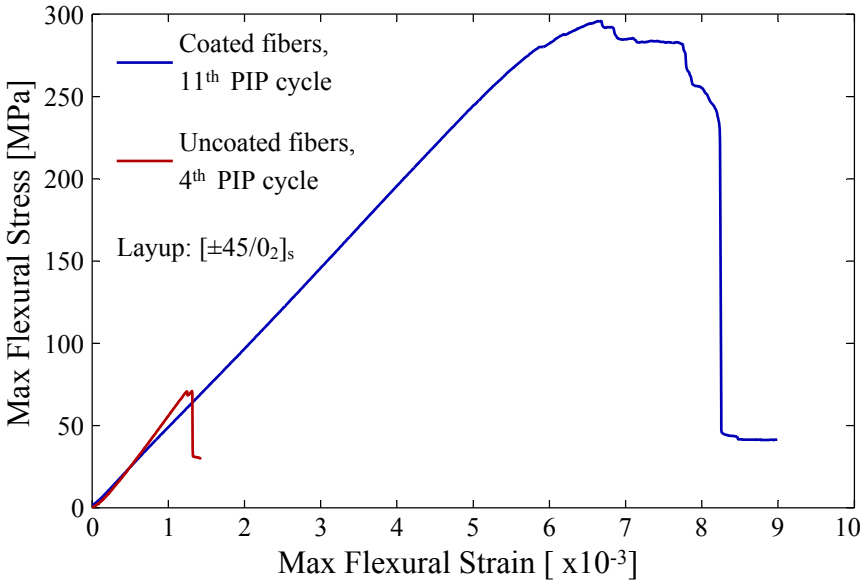



Figure 37: Stress-strain curve obtained by 3-point flexural testing of C/SiC composite with PyC-coated fibres. Results for uncoated fibres are also shown for comparison.

### 4.2.2 CMC-Metallic Bimorph Joining at NASA Glenn Research Centre

Along with manufacturing the CMC laminate, the chief challenge in fabricating CMC-metallic bimorphs lies in joining the metallic and composite layers in a manner suitable for high-temperature applications. Currently, ceramic composites and metals may be joined in such a manner using a process known as active metal brazing. Brazing is distinct from other joining methods (e.g. adhesives or soldering) in that the braze alloy diffuses into and penetrates the grain structure on the metallic side of the joint. Most brazes have difficulty wetting out chemically inert ceramics, thus a small proportion of a carbide-forming metal, typically titanium, is added to the braze alloy to promote reaction and consequently wetting-out of the ceramic side of the joint.

CMC-metal brazing trials were conducted at NASA Glenn Research centre, Cleveland OH. Cusil-ABA braze paste (Morgan Advanced Ceramics, Hayward, CA) was trialled for joining the University of Bristol CMC to Incoloy 800H coupons of 3.2 mm thickness. Cusil-ABA consists of a near-eutectic mixture of silver and copper, with a small portion of titanium to promote wetting of the SiC surface (63 wt% Ag, 35.25 wt% Cu, 1.75 wt% Ti). The braze is supplied in powder form. In order to apply it to a surface, the powder is mixed with glycerine to form a thick paste. The paste was applied using a spatula to the surfaces of the



**Distribution A: Approved for public release; distribution unlimited.**

CMC and Incoloy 800H substrates that were to be paired for joining, as shown in Fig. 38. Glycerine boils at 290°C, so it evaporates as the braze furnace is heated, leaving behind the appropriately distributed braze powder.

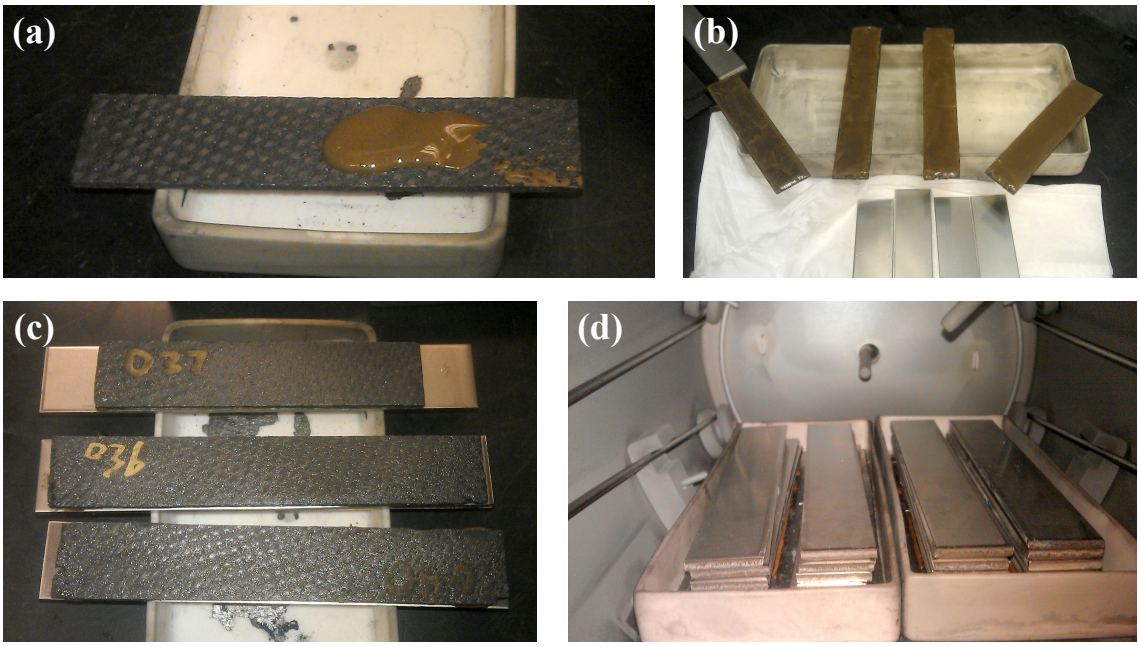



Figure 38: The braze application process.
a) Braze paste is deposited on CMC.
b) Braze paste is spread across entirety of CMC surface.
c) CMC specimens are placed on Inconel 625 strips.
d) The assembled laminates are placed in alumina boats in the braze furnace, and weights are stacked on them to squeeze out excess braze paste.

The assembly was loaded with a normal pressure of 0.2–0.4MPa using dead weight, and heated in a vacuum furnace to 830°C. The samples were held isothermally for 5 minutes, and slowly cooled to room temperature at a controlled rate, $\sim$ 5°C per minute down to 500° C, followed by free convective cooling under nitrogen atmosphere. The joined samples were mounted in epoxy and polished in preparation for metallurgical examination. The joint region was analysed using SEM and EDX techniques, with a well-bonded region shown in Fig. 39. Despite a bond-line that appeared continuous to the naked eye, microscopy revealed significant regions of debonding, with the failure occurring within the predominately SiC outer layer of the CMC.



**Distribution A: Approved for public release; distribution unlimited.**

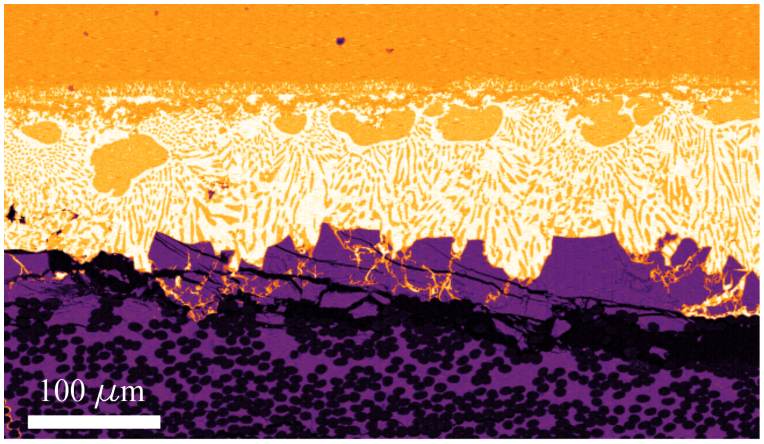



Figure 39: False colour SEM micrograph of C/SiC CMC (bottom) and Incoloy 800H (top) joined with a fully wetted brazed interface. The horizontal cracks visible in the outer SiC matrix layer were the site of debonding in failed specimens. The leopard-spot pattern in the braze layer is eutectic layering of the Cu-Ag braze. The efforts of Michael Halbig in obtaining this imagery are gratefully acknowledged.

Prior theoretical analysis of ceramic-metal joints indicates that stresses in the ceramic layer are reduced with the thickness of the metal layer is reduced [50], and when the CTE mismatch between layers is minimised. To that end, coupon trials were undertaken using Inconel 625 alloy of varying thickness between 0.8-3.0 mm. Inconel 625 is a nickel-based superalloy with a CTE approximately 20% less than Incoloy 800H. By lowering the CTE mismatch between high and low-expansion layers, it was hoped that a successful bond could be achieved without compromising high-temperature material properties.

Using identical braze cycle parameters as described previously with the thinnest gauge metal (0.8 mm), small coupon specimens of roughly 35 mm length could successfully be joined without gross interfacial debonding, as shown in Fig. 40. However, longer coupons or those using thicker gauges exhibited total debonding as also shown in Fig. 40. The length effect may be related to the fact that interfacial shear stresses increase with longer bond lengths [44]. However as the stress-relief effect is only significant for bond lengths less than roughly ten times the thickness of the laminate. The laminates had a minimum length of of roughly nine times their thickness. An alternative possibility is that larger laminates simply present a greater probability of containing a flaw in the braze joint of size greater than the critical crack length for the material.

Historically, successful CMC-metal brazing has been achieved by making efforts to reduce thermal mismatch stresses [51]. This runs counter to the typical bimorph strategy of max-



**Distribution A: Approved for public release; distribution unlimited.**

imizing mismatch stresses, however it is possible that a successful solution may lie in compromising bimorph actuation performance in favour of durability, perhaps through the use of an intermediate CTE interlayer. Regardless the present effort was not successful on a practical scale.



Figure 40: Photograph of debonded braze interface (left) and successfully joined laminate (right). Note the curvature that has developed in the joined laminate.

### 4.2.3 CMC-Metallic Flap Section

Although a bimorph laminate is perhaps the most structurally simple method of converting thermal strains into large displacements, other concepts exist, particularly those which do not require complete and continuous joining of the low and high expansion layers. Because a bimorph is normally a solid-core laminate (i.e., not hollow or sandwich construction), it has relatively poor bending stiffness for its weight. By separating the high and low-expansion skins, a higher specific bending stiffness can be attained, albeit at the cost of displacement amplitude. One such concept consists of a pair of skins, fastened to a root and joined along a common edge in a flap-like arrangement as shown in Fig. 41. In this concept, differential thermal expansion still acts to produce transverse displacement, however unlike the bimorph, the curvatures generated are non-constant across the chord. This concept has been previously investigated for variable-geometry nozzle chevrons, using an SMA skin joined to an opposing titanium skin [52]. This work aims to implement a similar concept which exploits the large thermal expansion mismatch between austenitic stainless steel and a ceramic matrix composite.



**Distribution A: Approved for public release; distribution unlimited.**

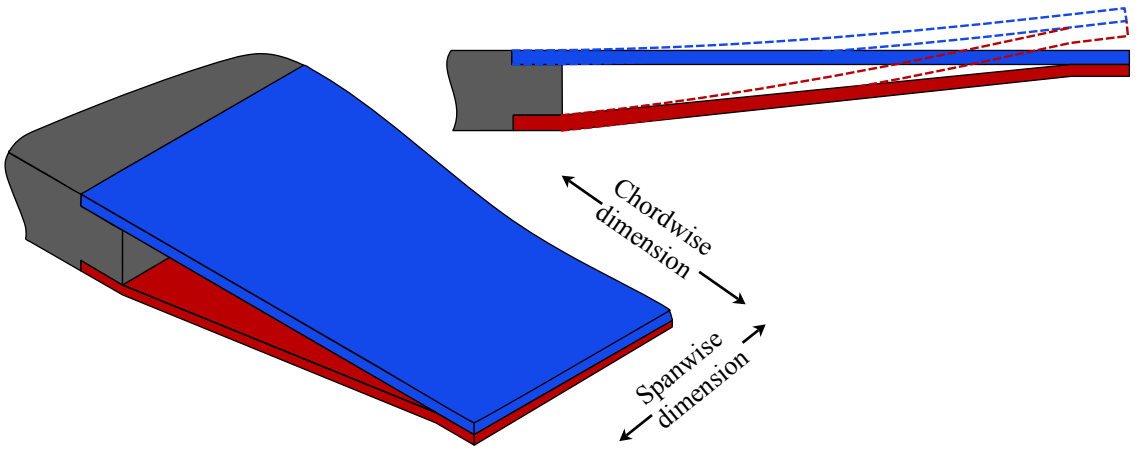



Figure 41: Drawing of the flap section thermal actuator concept. Dotted outlines show the approximate displacement field upon heating, assuming the red surface has a higher CTE than the blue.

Due to lack of success in manufacturing a CMC-metallic bimorph, attention was turned to this flap section concept as a method to achieve thermally driven morphing at high temperatures. The low expansion element is constructed from the same C/SiC laminate described in Section 4.2.1, while the high expansion element is fabricated from a sheet of AISI 310 stainless steel, a high-nickel austenitic alloy. The manufactured flap segments are relatively narrow, having a span of 20 mm for chord of 80 mm. While this beam-like geometry has the disadvantage of hindering observation of spanwise curvature and its effects, it was necessary due to the size limitations of the furnace. As shown in Fig. 42, the two elements are joined to each-other using a pair of 3.2 mm diameter pop-rivets, and mounted to a test fixture using a single M6 fastener. All fasteners and fixtures are of 304 stainless steel. Mechanical properties of the materials utilised for the flap section are shown in Table 9, while the layup and dimensions are given in Table 10.

Table 9: Thermoelastic material properties for the composites and metals used in the morphing flap section. Properties are given at room temperature unless otherwise stated.

| | $E_1$ or $E$ [GPa] | $E_2$ [GPa] | $\alpha_1$ or $\alpha$ $[\frac{10^{-6}}{°C}]$ | $\alpha_2$ $[\frac{10^{-6}}{°C}]$ |
|---|---|---|---|---|
| AISI Type 310 SS [53] | 200 | | 16.2 (0-315°C)<br>17.0 (0-538°C) | |
| C/SiC CMC [45] | 67.4 (flexural test by authors) | N/A | 2 (0-1000°C) | 5 (0-1000°C) |



**Distribution A: Approved for public release; distribution unlimited.**

Table 10: Manufacturing specifications for CMC-metallic flap sections.

| | |
|---|---|
| **Composite layup**<br>wv = woven T300<br>ud = unidirectional IM7 | $[45_1^{wv}/0_2^{ud}]_s$ |
| **Chord x span** [mm] | 80 x 20 |
| **CMC layer thickness** [mm] | 2.85 |
| **310SS layer thickness** [mm] | 1.50 |
| **Total section thickness at root** [mm] | 14.2 |

## 4.3 Experimental Procedures

The goal of this experiment is to measure the thermally induced displacements of the presently studied structures, as well as determine the approximate temperature at which each structure's thermal response fails to be repeatable. The experiment uses an optical target-tracking system to determine the displacement of painted-on targets. These targets are black dots located at the root and tip of each of the test articles, shown in Fig. 42. The figure also shows the 304 stainless steel fixture to which the test articles are bolted.

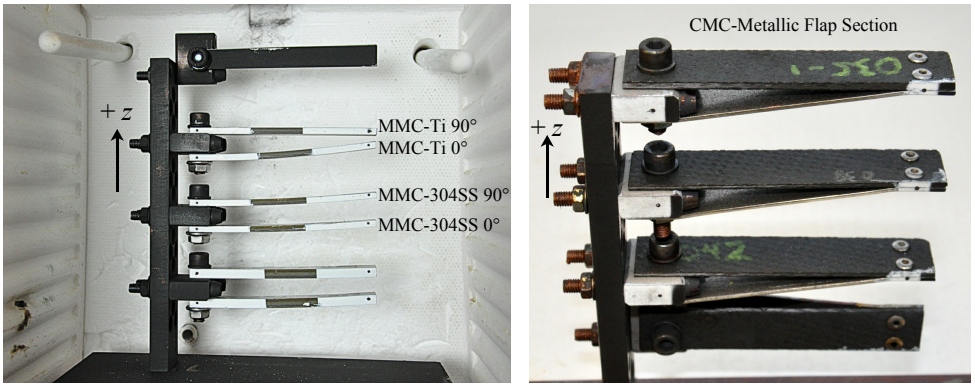



Figure 42: MMC bimorph (left) and CMC-metallic flap-section (right) test articles mounted on the test fixture with tracking targets painted on. In each image, one test article is turned 90° relative to the others in order to provide the thermal camera with a face-on view, thus providing a representative assessment of the temperature uniformity of the test articles. The lowest two test articles on each photo used alternate laminates and joining methods, their results are not presented in this work.



**Distribution A: Approved for public release; distribution unlimited.**

Our experimental setup is shown in Fig. 43. The test fixture assembly is placed in an electrically heated furnace, where it is viewed side-on by a thermal still camera (FLIR Systems, Wilsonville, OR) and an optical video camera (Imetrum, Bristol, United Kingdom). The furnace door is kept closed while it heats and stabilises at the desired measurement temperature. After a 30 minute hold to allow the test fixture and test articles to thermally equilibrate, the furnace door is opened for approximately 10 seconds, during which the optical and thermal cameras capture imagery. Displacements are extracted from video data using Imetrum VideoGauge software.

Being a somewhat unconventional high-temperature test technique, some problems had to be overcome. First, opening the door introduces a draft of cold air into the furnace, however the displacement data showed that the effect of this draft was negligible for roughly the first four seconds after door opening. Thus, the displacements are determined from the first two seconds of video. In addition, the mixing of cold and hot air causes a small degree of shimmering in the video data, in the same sense that the horizon over an asphalt road appears to shimmer on a sunny day. Despite this shimmering, consistent displacements could still be recorded by averaging the results of several consecutive video frames. This consistency was verified by using the video data to measure the thermal growth of the test fixture itself. When compared against the expected growth calculated from the fixture's known CTE, the displacement measurement error was 0.0336 mm, averaged across 20°C - 1000°C. An outlying maximum error of 0.224mm was observed at 824°C, which equates to a expected maximum relative error of 3.60 %, with respect to the curvature and displacement data presented in Section 4.3.1. Finally, an inversion of the video imagery greyscale values was observed at temperatures above roughly 800°C. Essentially, the imagery became a "negative" of its cooler self, which caused the tracking software to fail to lock onto the painted targets. This inversion was potentially due to the possibility that the video camera's sensor is sensitive to not just visible light, but also near-infrared (IR) radiation to some degree. Thus, black-painted areas would actually appear brighter than white areas at sufficiently high temperatures, due to a blackbody's greater IR emission intensity. This issue was resolved by using floodlights to drown out the IR emissions with reflected visible light. Consumer-grade digital SLR camera sensors do not seem to be susceptible to this greyscale inversion problem, at least at temperatures less than 1050°C.



**Distribution A: Approved for public release; distribution unlimited.**

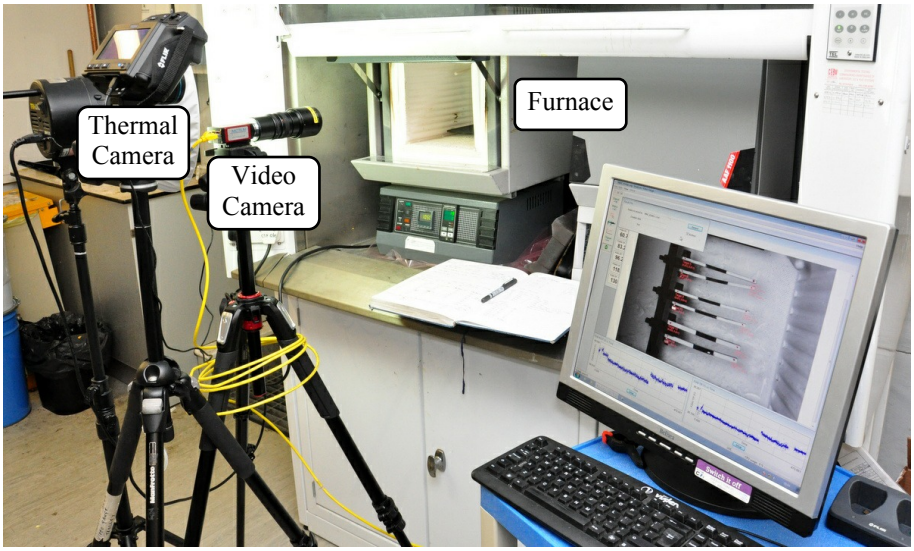



Figure 43: Experimental setup showing optical tracking and thermal cameras positioned in front of furnace.

Temperatures were measured using a FLIR Systems T650sc thermal camera, capturing still images as depicted in Fig. 44. Thermal imaging cameras convert measured radiation intensities to temperatures using an emissivity value set by the user, thus the emissivity of the object to be measured must be known. Heat-resistant black paint was applied to the test fixture so that its emissivity would approximate that of a blackbody emitter, thus enabling the temperature of the fixture to be computed correctly. The actual temperature of each test article was assumed to match that of the fixture at their respective mating surfaces, thus by observing the difference in computed temperature between the fixture and at test article where the two meet, a temperature correction factor could be computed to account for variations in emissivity.



**Distribution A: Approved for public release; distribution unlimited.**

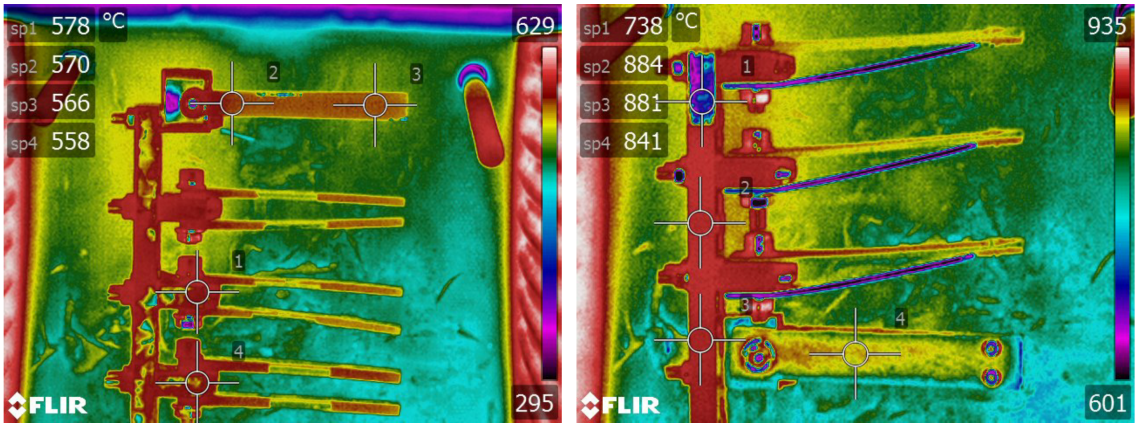



Figure 44: Thermal imagery data showing several MMC bimorph and CMC-metallic flap section thermal morphing test articles. The regions of locally lower apparent temperature are areas where bare metal is exposed, which due to its relatively low emissivity, appears cooler to the thermal camera.

The MMC bimorph test articles were subjected to three heating cycles, with peak temperatures of 394°C, 493°C, and 606°C, respective to each cycle. The CMC-metallic flap-section specimens were subjected to four heating cycles, with peak temperatures of 410°C, 608°C, 824°C, and 1035°C, respective to each cycle.

Curvature of the MMC bimorphs was determined by fitting the relative transverse displacement of the tip target $w_{\text{rel}}$ to a circular arc via: $\kappa = \frac{-2w_{\text{rel}}}{L^2+w_{\text{rel}}^2}$, where $L$ is the distance between root and tip targets. Relative displacement was determined by subtracting the root target displacement from the tip target displacement, whereby positive $w_{\text{rel}}$ is defined as the $+z$ direction in Fig. 42. Assuming curvature across the bimorph is constant, this procedure amounts to defining curvature according to the convention $\kappa = -\partial^2 w/\partial x^2$, thus positive curvature corresponds to a downward curl of the bimorphs as arranged in Fig. 42. The targets from which $w_{\text{rel}}$ is determined are the black dots shown in Fig. 42.

Up to 0.57° of rigid body rotation of the test fixture relative to the video camera was observed throughout the thermal cycling. While it is possible that the fixture experienced a degree of thermally induced distortion, it is more likely that the bulk of the rotation is due to distortion of the furnace chamber, camera tripod, or even the bench upon which the furnace sat. Regardless, the effect of this rotation was removed by rotating the camera's coordinate data to be square with the test fixture. As the CMC-metallic flap structures do no display constant curvature along their chord, results are instead presented simply in terms of transverse tip target displacement relative to the root target. As with the MMC bimorphs, rigid body rotation of the test fixture was accounted for in computing displacements.



**Distribution A: Approved for public release; distribution unlimited.**

### 4.3.1 Results and Discussion

### 4.3.2 MMC-Ti Bimorphs

The thermal response of the MMC-Ti bimorphs is shown in Fig. 45, along with curvatures predicted by CLT using the material data in Table 9. Some aspects of these bimorphs' thermal responses make intuitive sense, while others do not. This discussion starts with a description of the more intuitive features.

On the whole, we can see that the MMC-Ti bimorphs of both 0° and 90° fibre orientation show increasing curvature with increasing temperature. This result is expected, as the MMC layer has a lower CTE than the monolithic titanium layer in both 0° and 90° directions. The curvature rate (i.e., curvature change per unit temperature change) is indicated by the slope of the curves. From this result, we can see that curvature develops much faster for 0° fibre orientations vs. 90°, by a factor of about 2.1. This result is also expected, due to the fact that the CTE mismatch between monolithic and composite layers is maximised in the 0° direction.

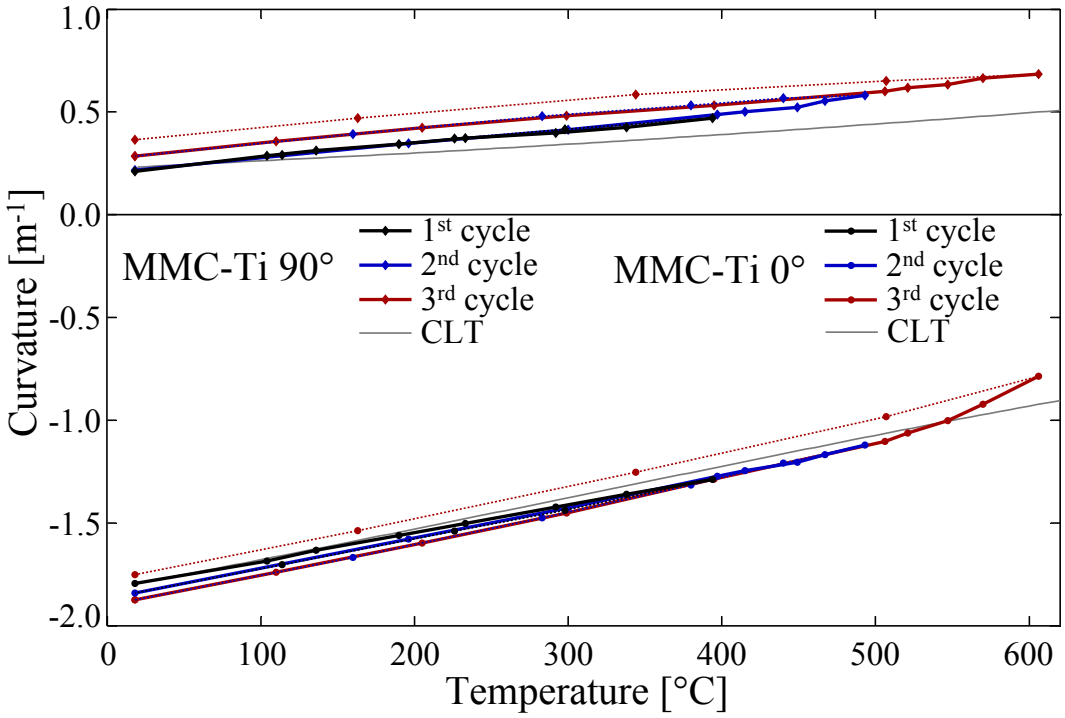



Figure 45: Thermally induced curvature of MMC-Ti bimorphs. Solid lines link data points measured during heating, dotted lines link cooling data points.



**Distribution A: Approved for public release; distribution unlimited.**

The first heating cycle reached 394°C, up to which a linear curvature temperature relationship was observed for both 0° and 90° fibre orientations. The second heating cycle reached 493°C. Like the first heating cycle, it also showed a predominately linear temperature-curvature relationship for both fibre orientations. The third heating cycle reached the test's maximum of 606°C. Up to 500°C, the thermal response again was predominately linear, however beyond this temperature, an increase in the rate of curvature generation with respect to temperature was observed for both fibre orientations. This behaviour could be due to the titanium alloy's greater CTE at high temperatures, however it is not clear why the nonlinearity is only observed above 500°C, as opposed to across a wider range of temperatures as would be suggested from known CTE data of this material system.

The curvatures observed upon cooling significantly differ from those measured during heating, indicating that some degree of non-recoverable strain has been induced above 500°C. This sort of hysteretic behaviour may be expected due to high temperatures yielding or creep effects. Analysis of the internal stress state of the laminate is made complicated by a number of competing factors. Recalling that the laminates were consolidated on a flat tool at approximately 900°C, we expect stresses to increase with departure from this temperature. Thus, we actually expect a reduction in thermally induced stresses as the bimorphs are heated, so long as the material stays within the elastic regime. However there are two factors which are likely to invalidate this elastic assumption:

1. When cooled from consolidation, the laminate is held restrained against its flat tool by both the isostatic pressure, and the stiffness of the conforming canister in which the laminate is encapsulated. While it is difficult to say whether the laminate is constrained to a perfectly flat shape during this manufacturing cool-down, it is certainly possible that the stresses induced by this restraint could be of sufficient magnitude to induce yielding in at least one of the layers.

2. The yield stress of Ti-3Al-2.5V is reduced with increasing temperature. At 300°C, for example, the yield stress of this alloy is reduced to 60 % of its room-temperature value [39]. Material data from similar alloys suggests that the reduction in yield stress becomes especially pronounced above 450°C, with results becoming time-dependent as well [32].

The first item mentioned above would suggest that we would expect yielding to take place at lower temperatures, as that is where thermal stresses are highest. On the other hand, the second item suggests that yielding could also take place at higher temperatures, as that is where the material's yield stress is minimal. Creep could also play a role in contributing to non-recoverable strain. Without a dedicated analysis, it would be quite difficult to determine



**Distribution A: Approved for public release; distribution unlimited.**

the exact nature of any non-recoverable strains, however the experimental data does provide us with some clues.

If all strains were elastic, we would expect the bimorphs to recover their flat shape when heated to the consolidation temperature ($\sim 900°$C). This response is clearly not the case for the 90° fibre bimorph. Its room-temperature curvature is positive-signed, which is the opposite of what we would expect based on the sign of the CTE mismatch between layers. The fact that it develops positive curvature with increasing temperature (as expected) rules out gross errors in the material data, thus the large discrepancy in room-temperature curvature is likely a result of non-recoverable strains developed upon cool-down from consolidation.

In particular, the results are consistent with a scenario whereby the strain developed upon cool-down from consolidation was predominately plastic in the 90° direction, and predominately elastic in the 0° direction. Thus, when the laminate was released from its constraints upon being de-tooled, the stored elastic strain caused the laminate to develop a large degree of curvature in the 0° direction. Meanwhile, the plastic strain in the 90° direction, being non-recoverable, did not contribute to development of curvature in the 90° direction. Instead, the curvature that was developed in the 90° direction was instead *anticlastic curvature*, that is, it was a result of elastic Poisson coupling with the 0° curvature that developed upon detooling.[12] This hypothesis is consistent with the observation that the 90° bimorph's curvatures were offset in the positive direction, relative to the shape that would have been attained from a purely elastic cool-down from consolidation temperature.

In the latter two cycles, the curvature-temperature relationship measured upon heating matched that measured from the previous cooling cycle. This lack of hysteretic behaviour at cooler temperatures suggests that the offset in curvatures between successive cycles is due to non-recoverable (e.g. plastic or creep) strains generated at higher temperatures. The coincident temperature-curvature relationship at lower temperatures also suggests that error due to thermal lag between the test specimens and thermal camera measurements is unlikely, otherwise we would see the hysteretic effects at low and high temperatures alike.

By observing trends in the cyclic data, we can draw preliminary conclusions regarding the maximum temperature that can be attained without significant loss of repeatability. These conclusions are somewhat under-conservative, as this test program only consisted of three thermal cycles. In other words, it is possible that a temperature-curvature relationship may appear repeatable because two consecutive cycles gave similar results, however there is still

[12] In general isotropic plates, unrestrained elastic curvatures are coupled via the relation $\kappa_x = -\nu\kappa_y$. Although the MMC specimens are not isotropic, the same trend applies, in that an elastic change of curvature in one direction leads to an opposite change in the orthogonal direction, albeit scaled down by Poisson's ratio.



**Distribution A: Approved for public release; distribution unlimited.**

the potential for long term drift in the measured curvatures, perhaps due to creep effects, for example.

The 0°-fibre MMC-Ti bimorph showed nearly coincident cyclic data up to 500°C, however the third cycle, which reached 606°C, exhibited non-recoverable deformations as evidenced by the observed hysteresis loop for that cycle. The 90°-fibre specimen, comparatively, showed onset of hysteretic behaviour during the second cycle, and thus temperatures above approximately 400°C cannot be considered to give repeatable curvatures for the case of 90° fibre orientation.

### 4.3.3 MMC-304SS Bimorphs

Results for the 0° and 90° fibre orientation MMC-304SS bimorphs are shown in Fig. 46 along with CLT analytical predictions. The idea behind using stainless steel as the high-expansion layer is to provide a greater CTE mismatch with the MMC layer compared to using monolithic titanium. A linear fit to the 0° MMC-304SS curvature data gives a curvature rate of $5.4 * 10^{-3}$ $(\mathrm{m} *^{\circ} \mathrm{C})^{-1}$, which represents a 3.6-fold increase in curvature rate over the 0° MMC-Ti bimorph. This factor of curvature rate improvement is nearly identical to the factor by which the CTE mismatch was increased in switching the high-expansion layer from titanium to stainless steel. This result is anticipated by Timoshenko's seminal bimorph model [11], as well as CLT, which both predict that curvature rate varies in direct proportion to the CTE mismatch between the high and low expansion layers.



**Distribution A: Approved for public release; distribution unlimited.**

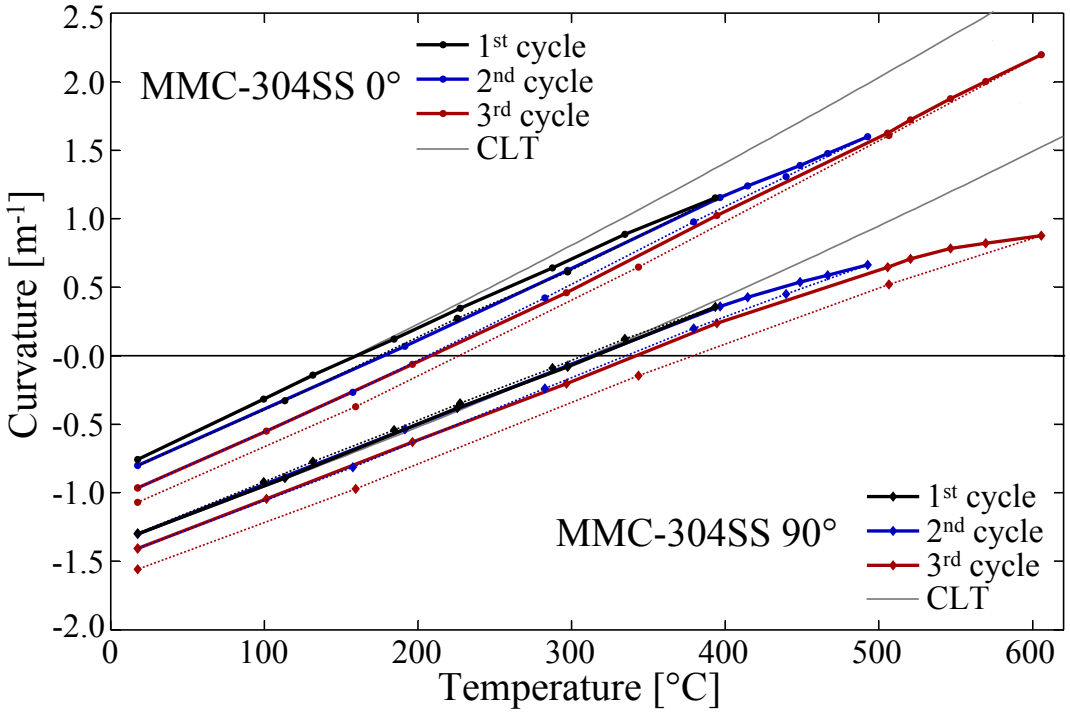



Figure 46: Thermally induced curvature of MMC-304SS bimorphs. Solid lines link data points measured during heating, dotted lines link cooling data points.

Both the 0° and 90° MMC-304SS bimorphs exhibit room temperature curvatures of much lesser magnitude than would be expected if the cool-down from consolidation induced only elastic strains. It is likely that the curvature restraint applied by the HIP process and tooling has induced a significant degree of non-recoverable strain in one or more layers of the laminate. This hypothesis is further supported by the fact that both bimorphs recover a state of zero curvature at temperatures well below their consolidation temperature.

Interestingly, the 0° bimorph's room temperature curvature is offset in the positive direction, though of lesser magnitude, from the 90° bimorph, which is opposite to what was observed with the two MMC-Ti bimorphs. This result is unexpected, as it suggests that upon detooling, the MMC-304SS laminate elastically recovered a lesser magnitude of curvature in the 0° direction relative to the 90° direction. Previous literature [38] indicates that the elastic limit strain of SiC/Ti MMCs is much greater parallel to the fibres vs. perpendicular, which would suggest that we would actually expect a greater degree of elastic curvature recovery in the 0° direction.

Both 0° and 90° bimorphs exhibited a nearly constant curvature rate and small degree of



**Distribution A: Approved for public release; distribution unlimited.**

hysteretic behaviour during its first thermal cycle. The second cycle showed a decrease in curvature rate above 400°C, and a larger degree of hysteresis upon cooling. The third cycle continued this trend. Notably, the curvatures measured at the peak temperatures of the first and second cycles were nearly identical to the curvatures measured while passing that same temperature during the following cycle. In other words, as each bimorph was heated beyond its previous peak temperature, the curvature "picked up where it had left off" during the previous cycle. This effect is most pronounced in the 90° bimorph, and is reminiscent of the plastic loading, elastic recovery behaviour of beams cycled through moments which induce maximum stress beyond their material's elastic limit. It appears that while the use of 304 stainless steel for the high expansion layer does give a great improvement in curvature rate, the additional thermal stresses induced are sufficient to lead to non-recoverable deformations at temperatures greater than about 400°C.

### 4.3.4 CMC-Metallic Flap Section

Results for displacement of the tip tracking target of the CMC-metallic flap section are presented in Fig. 47. Also presented are results from a finite element model (ABAQUS 6.12), using 160 S8R shell elements, with geometry and boundary conditions mimicking the experiment. Solutions were obtained using the software's iterative solver in order to account for geometric nonlinearity.

The flap section was put through four temperature cycles, each of progressively higher temperature, up to a maximum of 1035°C. The first cycle to 410°C showed a small degree of nonlinearly in the region of 250-300°C. It is possible that this nonlinearity in the displacement data is due to the CMC and/or 310SS layers slipping slightly at the bolted root joint or riveted tip joint, as there is some clearance between the fastener's outer diameter and holes in the CMC and 310SS layers.

During the second and third thermal cycles, the flap section exhibited a predominately linear displacement-temperature relationship. This result is in line with expectations, for reasons as follows. The assembly is essentially a pair of beam-columns, joined at their ends. As long as the axial loads in each beam-column are small relative to the Euler buckling load, we can expect the tip displacement of the assembly to vary approximately in proportion to the growth mismatch of the joined beam-columns. In fact, finite element results show that with sufficient growth mismatch (i.e., sufficient $\Delta T$), the compression member buckles in the Euler manner, and further increases in tip displacement are greatly restricted thereafter. For the current geometry, this buckling is not forecast to occur until well beyond the tested temperature range. However, note that this buckling action is sensitive to geometry. Naturally, flap sections of long chord and low thickness are more susceptible to buckling



**Distribution A: Approved for public release; distribution unlimited.**

than those of stouter proportions for a given pair of skin materials. Other workers have successfully addressed the buckling problem by joining the high and low-expansion skins with spanwise ribs, thus allowing the skin in compression to be supported by the adjacent, tension-stabilised skin [52].

The fourth thermal cycle also showed a predominately linear temperature-displacement relationship, however the displacement values were offset to lower values from the previous cycles. Bearing in mind that the assembly was joined in a stress-free state at room temperature, it is likely that this non-elastic behaviour was a result of the higher stresses at elevated temperatures, thermal degradation of material properties, or some combination thereof. There is of course the additional possibility that slip in the bolted or riveted joints is at least partly responsible, however the displacement measurement method does not allow us to separately analyse these potential sources of nonlinearity.

It is difficult to evaluate the maximum temperature that gives repeatable deformations. While the second and third cycles showed some degree of hysteretic behaviour, the fourth cycle exhibited almost completely recoverable deformation. This unexpected trend in the results lends more weight to the possibility that the prior cycle's non-recoverable deformations were due to slip in the joints.



**Distribution A: Approved for public release; distribution unlimited.**

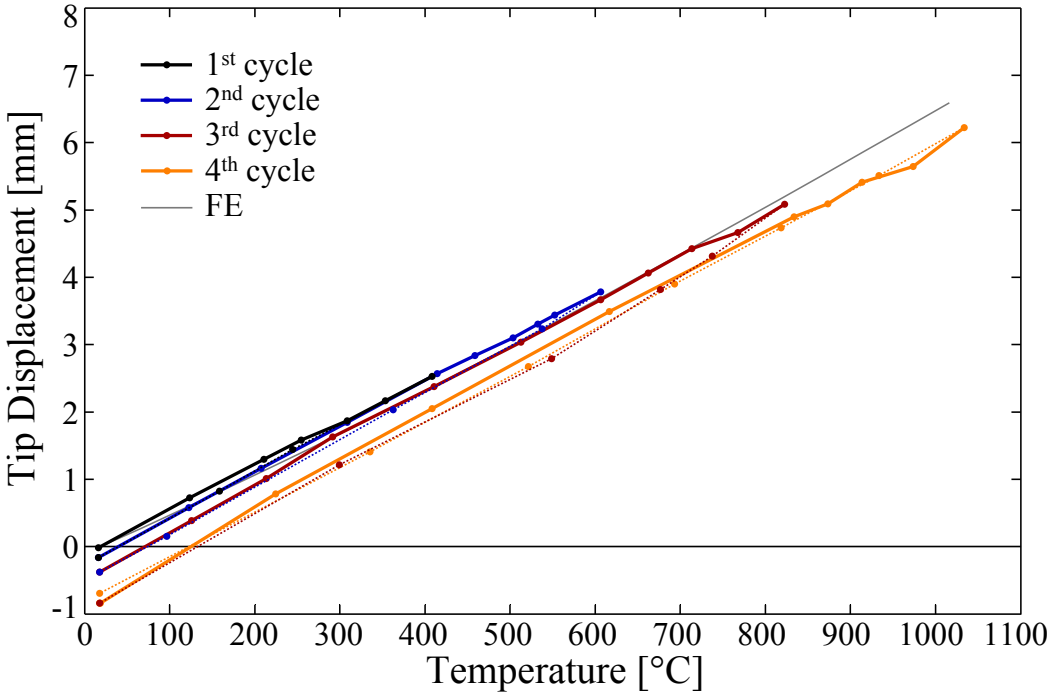



Figure 47: Experimentally measured and finite element (FE) results showing the thermally induced tip displacement of CMC-metallic flap section. Solid lines link data points measured during heating, dotted lines link cooling data points.

Figure 48 shows an image of the flap section near the maximum test temperature superimposed upon its room temperature shape. Note that the 310SS skin, which acts in compression, has a higher degree of curvature along its length than the tension-stabilised C/SiC skin, as we would expect based on a joined beam-column representation of the structure. Figure 49 shows the test rig in the furnace at approximately 1000°C. It is worthy to note that the heat given off by the intense IR radiation becomes quite uncomfortable after only a few seconds. The camera equipment is unlikely to tolerate the heat much better than its operator. Given that heat transfer rate by radiation scales with the fourth power of temperature, it is unlikely that the "open the door and take a picture" test method would be suitable for use at temperatures much more than 1100°C.



**Distribution A: Approved for public release; distribution unlimited.**

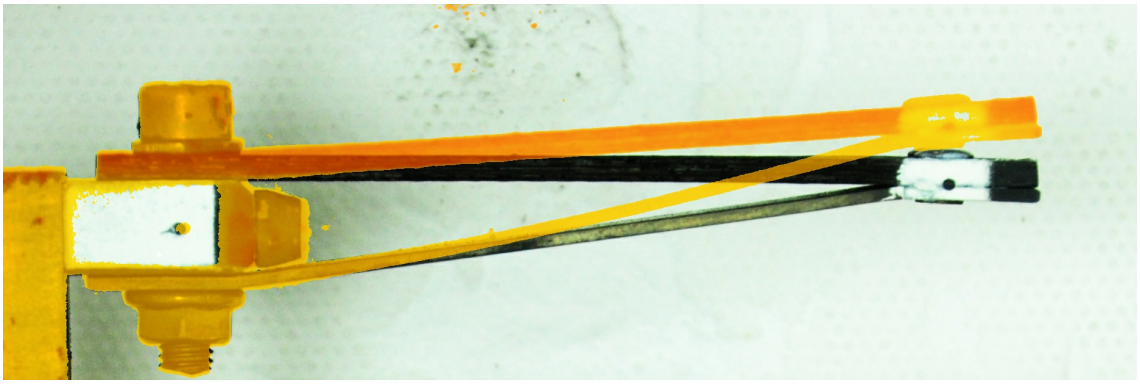


Figure 48: Image of the CMC-metallic flap section at $\sim$ 1000°C in its naturally occurring orange glow, overlaid upon an image of the same structure at room temperature.

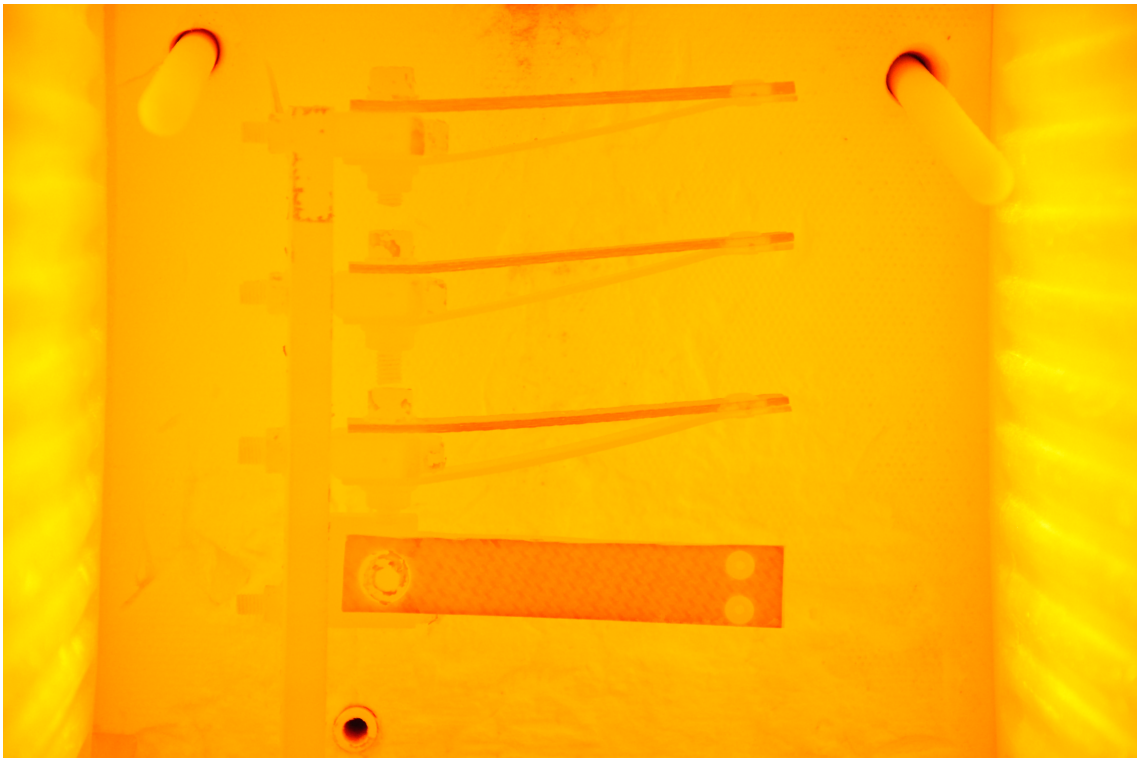


Figure 49: The camera and experimenter's view of the furnace at roughly 1000°C.



**Distribution A: Approved for public release; distribution unlimited.**

# 5 Outcomes

The present study was enacted in order to develop modelling tools and structural concepts that apply to thermally driven morphing structures in high-temperature environments. The outcomes of are summarised below.

## 5.1 Outcome 1: Improved Modelling of the Nonlinear Thermo-structural Response of Composite Bimorph Shells

An energy-based multistability model was developed to predict the nonlinear curvature-temperature relationship of composite bimorph shells. This model is intended to serve as initial design and analysis tools for thermally driven bimorph laminates. Its ability to rapidly find the possible stability states of a thermally loaded bimorph allows the designer to identify promising geometries and materials to conduct further, more detailed analysis with numerical tools such as commercial FE codes. Although the accuracy of this low-order model is poor relative to finite elements and higher-order analytical models, its relative simplicity makes it easier for the analyst to gain fundamental insight. The novelty of the model can be summarised as follows:

### Limitations of the Model

The analytical model developed in this work assumes that the laminate has free-free boundary conditions. While these assumptions allows fairly generic results to be presented, it ignores the practical issues of attachment and integration into a broader structure. In general, the constraint of pinned or clamped edges tends to reduce the tendency of a laminate to display multistable properties. As a result, we can consider the modelling results to give a rather liberal prediction of the degree of nonlinearity that can be introduced into composite bimorphs.

Additionally, the analytical model only considers square and rectangular laminates. In many applications, such as nozzle chevron morphing, other planforms such as trapezoids or triangles would be utilised instead. Experience in using the present analytical model for such design exercises shows that the behaviour of trapezoidal laminates can be approximated by a rectangular laminate of similar "average" dimensions, and thus would still be suitable as an initial design tool. Following initial design, other more complex models designed to handle general geometries (e.g. FE or Lamacchia *et al.* [33]) could be brought to bear on the problem.



**Distribution A: Approved for public release; distribution unlimited.**

In addition, the analytical model assumes linear-elastic material properties. While this case is generally an accurate representation of reality at low to moderate temperatures, high-temperature experiments revealed that some inelastic mechanism, either creep or plastic yielding, had a significant impact on the bimorph's thermostructural behaviour. This problem is inherently difficult to address with elastic energy-based models, as their very nature makes no account of any non-conservative effects such as plasticity. Given that inelastic deformations are generally be considered undesirable in morphing applications to begin with, this modelling limitation is not considered to be critical.

Furthermore, the analytical model considers only uniform curvature. While this case seems to qualitatively cover the known range of multistable plate behaviour, it is certainly possible that new phenomena, such as penta-stability, can be realised using shells of non-uniform curvature.

Finally, it is worth noting that experimental verification efforts focused on the single-curvature case only. Therefore, it cannot be said with full confidence that the model can accurately capture the behaviour of doubly curved shells.

## 5.2 Outcome 2: Demonstrate Thermally Driven Snap-Through With a Composite Bimorph

Work conducted under our prior EOARD grant predicted that thermally driven snap-through could be achieved through the combined use of initial curvature and a laminate which developed highly asymmetric thermal moments. Based on this prediction, low-expansion CFRP composites were laminated with high-expansion aluminium alloys. When constructed with appropriate fibre orientations and initial curvature, these laminates displayed a snap-through transition between stable states when heated and cooled. The snap-through process consists of a transition from one stable shape to another, and occurs when a bistable shell in one shape reverts to a state of monostability characterised by the alternate stable shape. Although a similar response has been achieved using bimetal beams compressed between end-constraints, this is the first instance of a cylindrically curved bimorph demonstrating such behaviour as far as the author is aware. The snap-through temperature for heating was higher than for cooling, indicating that the structure behaved in a hysteretic manner. This hysteresis was not due to material nonlinearity, but rather due to geometric nonlinearity.

A material selection study was conducted to investigate the optimum pairings of low and high-expansion layers for generating maximum thermal moment. The best material pairs exhibited high CTE mismatch, high stiffness, and low density, with CFRP/Mg and CFRP/Al alloy pairings performing best. The use of shallow angle-ply stacking sequences allowed



**Distribution A: Approved for public release; distribution unlimited.**

bimorph performance to be improved further still, and may also provide an improvement in durability compared to unidirectional composite layups.

### Limitations

Snap-through behaviour was achieved using free-free boundary conditions. As noted in Section 5.1, practical implementations of snap-through structures would require some sort of boundary condition which would likely change, and likely restrict the laminate's tendency to display such behaviour. However, there are practical implementations which would not significantly violate the free-free boundary condition assumption, as proposed in Section 7.

The bimorph laminates exhibited very low stiffness near their snap-through temperatures on account of the impending loss of stability. In practical applications, this marginal stability means that any external loads would likely have a large effect on the actual snap-through temperature of such a structure. Other potential issues such as fatigue and repeatability remain unanswered as they were outside the scope of this work.

## 5.3 Outcome 3: Develop and Demonstrate Composite Bimorphs Suitable for High-Temperature Use

Two types of metal matrix composite bimorphs were developed in the course of this work. The first consists of a low-expansion layer of silicon carbide fibre, titanium alloy matrix composite, joined via diffusion-bonding to a high-expansion layer of monolithic titanium alloy. This construction, referred to as MMC-Ti, exhibited recoverable deformations when cycled between room temperature and up to 500°C. Its as-manufactured shape at room temperature was difficult to predict, as the stresses developed upon cool-down from the 900°C hot-pressing temperature were high enough to induce plastic deformation. The existing fibre-foil approach to MMC manufacturing was found to be suitable for fabrication of this laminate.

The second MMC-based bimorph consists of the same low-expansion MMC layer, now diffusion-bonded to a monolithic layer of AISI type 304 stainless steel. This construction, referred to as MMC-304SS, has a CTE mismatch between layers 3.6 times greater than the MMC-Ti bimorph concept. Accordingly, it developed 3.6 times the curvature as the MMC-Ti bimorph, for the same temperature change. However, on account of the greater thermal stresses resulting from this pairing of materials, the MMC-304SS bimorph only exhibited recoverable deformation up to 400°C, compared to the 500°C attainable by MMC-Ti bimorphs.



**Distribution A: Approved for public release; distribution unlimited.**

Seeking a low-expansion material with high strength and low creep at high temperatures, capability was developed within the University of Bristol to manufacture CMC material using the polymer infiltration and pyrolysis method. This composite consisted of commercially available carbon fibres encased in a polymer-derived silicon carbide matrix. The first batches of material were weak and brittle due to overly strong fibre-matrix bonding. Later batches incorporated a pyrolytic carbon fibre coating which reduced the interfacial bond strength. Consequently, the strength and strain-to-failure of the composite was greatly improved, to the point where it made a suitable candidate as the low-expansion element in a thermal bimorph.

The in-house manufactured CMC was intended to be brazed to Inconel 625 nickel alloy, however the two layers consistently debonded during cool-down from the brazing temperature. Failure of the joint took place in the outer-most layer of silicon carbide matrix, indicating that CMC-metallic bimorphs may yet still be feasible if the strength of the matrix can be improved.

With the failure of the brazed CMC-metal bimorph, a morphing flap was trialled instead. This device consisted of a layer of CMC joined mechanically to an AISI 310 high-nickel stainless steel sheet, and successfully demonstrated thermally driven morphing at temperatures up to 1030°C. Although this concept lacks the inherent simplicity of the bimorph, it successfully demonstrated that the CTE mismatch between CMC and nickel alloys can be exploited to create morphing hot structures.

### Limitations

The experiments on the MMC and CMC-based thermal morphing structures were intended to evaluate their suitability for high-temperature morphing applications, however most applications would entail special requirements for which a single general experiment cannot provide fully conclusive results. Thus, the results presented here are better thought of as being demonstrative of the potential of high-temperature morphing, rather than to be used as strict design data. Nonetheless, a discussion of the experimental program's limitations is still warranted.

Perhaps the most significant limitation of the results is that the experiment did not impose any mechanical loads upon the bimorphs. It is likely that the maximum-use temperature of a thermal bimorph is reduced when some external load is imposed upon it, on account of the additional stresses induced by that load. Another significant limitation is the fact that the morphing structures were only thermally cycled 3-4 times in total, and only once up to the maximum test temperature. Thus, the experiment is unlikely to capture any creep or fatigue effects. Stress-corrosion cracking was of course not considered either, and given



**Distribution A: Approved for public release; distribution unlimited.**

that these structures are meant to operate in hostile environments, this factor could prove to have a significant effect on the durability of thermal morphing structures.

# 6 Impact

This work encompassed a variety of modelling and experimental developments, each with their own potential utility. The following sections discusses the potential impact of the main outcomes of the work.

## 6.1 Impact of Modelling Developments

The models developed in this work are relatively simple, yet still capture the scope of known behaviour in multistable plates and shells. As such, they will likely find their place as initial design tools, fitting between back-of-the-envelope hand calculations and detailed FE analysis.

The success of a given model is measured not only by its speed and accuracy, but also by the ease of adoption at the hands of other users. A multitude of multistability models have been published in recent years, however many of these models are so complex that it is difficult for other workers to reproduce them, or for that matter improve upon them. The relative simplicity of the models developed herein will hopefully allow other workers to not only fully understand them, but also facilitate further development.

Computer-coded implementations of the models developed under this contract have been made publicly available [54].

## 6.2 Impact of Snap-Action Bimorph Development

### Morphing Chevrons for Noise and Drag Reduction on Aero-Engines

Thermally driven snap-through has long since been exploited for use in thermostats and circuit breakers. However, these prior implementations, would not be practical to implement in most deployment and aerodynamic control applications on account of their required geometrical boundary conditions. The presently developed snap-action bimorph could have a number of valuable applications. Perhaps the most promising concerns noise abatement in civil aero-engines. The Boeing Company currently employs static “chevron” devices on the trailing edge of fan nacelles on certain aircraft types. These chevrons impinge upon the fan exhaust flow, shedding vortices which contribute to a reduction in perceived jet noise [55].



**Distribution A: Approved for public release; distribution unlimited.**

This vortex generation results in additional drag, and thus ideally, they would only impinge upon the fan flow during takeoff and landing, otherwise remaining parallel to the flow to reduce drag.

If these chevrons were constructed as thermal bimorphs, perhaps from the CFRP-Al laminates described in Section 2, the natural reduction of air temperature at high altitudes could be used as the driving thermal load.[13] In other words, the chevrons would deflect into or out of the fan flow when triggered to do so by change in ambient temperature, as illustrated in Fig. 50. The resulting system would be completely passive, requiring no sensors or control system, and would likely add only a very small amount of weight beyond the present design.

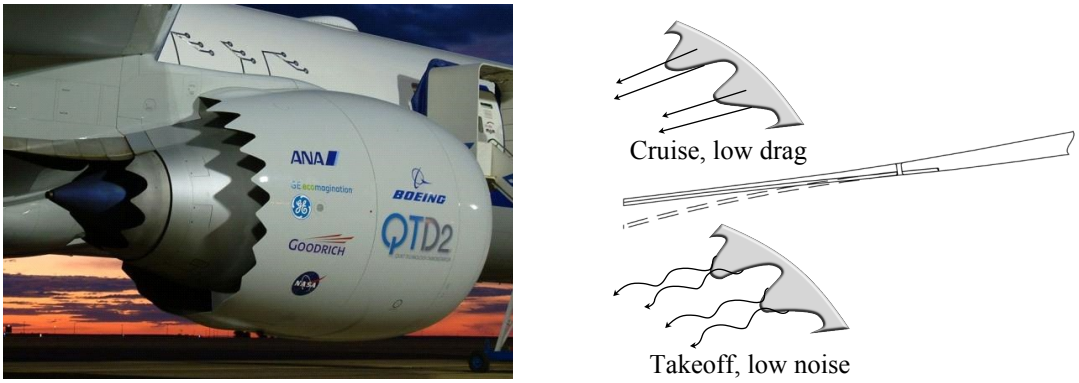



Figure 50: Fan and core exhaust chevrons present opportunities for thermally driven morphing structures.

A potential issue is that not all takeoffs and landings occur at the same ambient temperature. If the aircraft were operating out of a particularly cold airport, $-20°$C for example, the chevrons may not fully deploy to their "warm" $+20°$C state, instead exhibiting a curvature between the takeoff and cruise shapes. This undesirable behaviour could be mended with the use of snap-action bimorphs. The nonlinear temperature-displacement relationship that can be tailored into these sorts of bimorphs allows the designer to set the shape change to occur at say, $-30°$C, with negligible shape change occurring above this temperature. The result would be a chevron which could be guaranteed to be in the noise-reducing shape for nearly every conceivable airport climate, yet still morph to the drag-reducing shape during cruise, which consistently entails ambient temperatures of below $-40°$C. Fortuitously, the initial

[13]This concept is similar to a NASA/Boeing collaboration, which designed and flight-tested SMA-actuated chevrons during their Quiet Technology Demonstrator 2 program. To the author's knowledge, this effort represents the closest a genuine morphing technology has come to aerospace adoption, however Boeing ultimately choose not to implement the technology, at least for the time being.



**Distribution A: Approved for public release; distribution unlimited.**

curvature required to obtain snap-through behaviour is already provided by the existing circumferential curvature of the nacelle, thus there would be minimal impact on the overall nacelle design. It is also worth noting that if snap-action is undesirable, perhaps it frightens the passengers, then it is also feasible to tailor the temperature-displacement response such that the shape change takes places smoothly across a small temperature window.

#### Self-Deploying Booms

Bistable reeled composite booms, shown in Fig. 51, have found applications in deployment systems. Current designs must be deployed by some external actuation mechanism, however if the reel were to be constructed from a hybrid fibre-metal laminate, it could be made to self-deploy and stow when a certain temperature threshold was crossed. The applications would be of course limited to cases where passive deployment was acceptable, but for these situations, snap-acting laminates bring a new capability to the field of deployable structures. The boom could stow and deploy in a reversible fashion, or could be designed with such a large difference between the heating and cooling snap-through temperatures that it effectively functions as a one-time-use device. This sort of design could be useful in space deployment applications, where the designer could use the cold of shaded space to trigger deployment, without the risk of solar heating unintentionally re-stowing the boom. Nonlinear bimorphs may also be useful on smaller scales, including micro-fluidic controls and nanoscale electrical switches [56, 57].



Figure 51: Bistable reeled composite in partially deployed state. Although these booms are bistable, current designs require an external actuator to stow and deploy.

## 6.3 Impact of High-Temperature Bimorphs

High-temperature bimorphs can allow morphing structures to function in environments too hot for conventional variable-geometry systems. Ideally they would be used in a passive manner, thereby negating the need for any sort of control system. Passive operation requires that the desired shape of the structure be related to its temperature. This situation is naturally



**Distribution A: Approved for public release; distribution unlimited.**

the case in thermal control applications such as thermostats and spacecraft radiators, however such cases also apply to a number of gas-turbine propulsion applications. This coupling of temperature and desired shape is due to the fact that gas temperatures throughout such an engine are dependent upon the engine's operating state, and likewise, the ideal shapes of aerodynamic components also depends on the engine's operating state. Full-thrust operation, for example, entails higher turbine temperatures, and favours a larger stator nozzle throat area [58]. Likewise, part-thrust operation entails lower turbine temperatures, and favours a smaller stator nozzle throat area. A turbine nozzle cascade which could vary its throat area, as shown in Fig. 52, would allow the engine to operate more efficiently across a wider range of conditions than present fixed turbine nozzles. Early theoretical work on the subject quoted an off-design thrust-specific fuel consumption benefit of 5-8 % [59], a significant benefit by modern propulsion standards. This capability has been sought since the early days of gas turbine engines [60], however the difficulty of implementing variable-geometry turbine nozzles has stymied efforts. Thermal bimorphs integrated into the trailing edge of each turbine stator blade may represent a solution to the challenge of variable-geometry turbine nozzles.

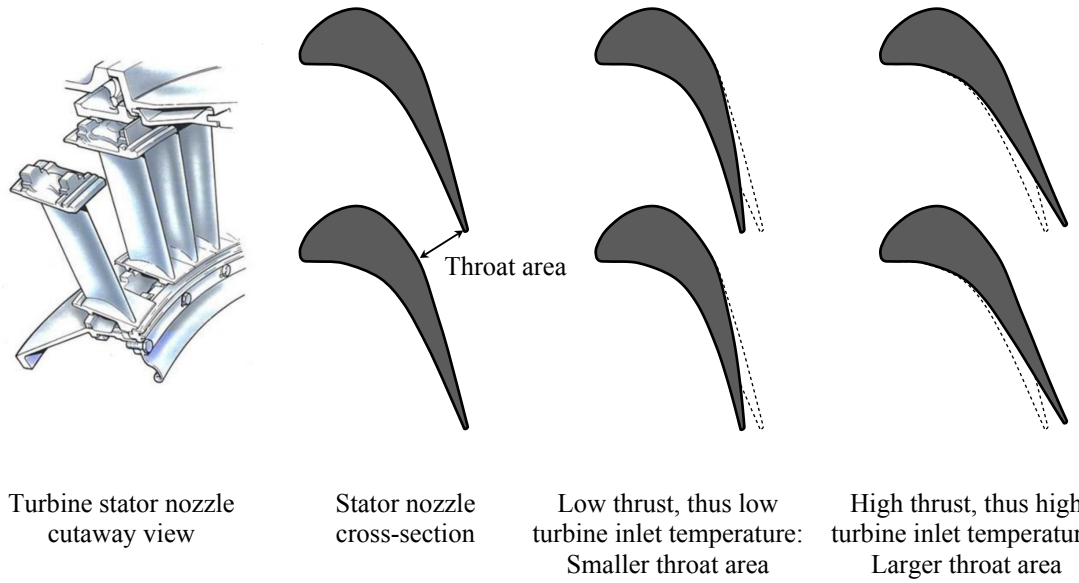



Figure 52: Turbine stator nozzle morphing allows their throat area to be varied according to the engine's operating state. Morphing could be facilitated by constructing the trailing edge of each blade in the fashion of a thermal bimorph, or adopting the flap-section concept discussed in Section 4.2.3.

Several other gas turbine applications are ripe for exploitation, including, but certainly not



**Distribution A: Approved for public release; distribution unlimited.**

limited to:

**Variable Cooling Flow**

A large portion of the air injected into the combustor is not used for combustion, but rather to dilute the combustion products such that they are cool enough not to damage the downstream turbine blades. Likewise, turbines and stator nozzles must be actively cooled to stay within material temperature limits. The engine's cooling requirements are designed for the worst case scenario of full-thrust operation on a hot day, however most of the engine's life is spent at cruise, where cooling needs are reduced. Overcooling the engine reduces efficiency. This inefficiency arises because cooling air can only be delivered to the high-pressure sections of the engine if it is first pressurised in the compressor. Because compressors and turbines are not perfectly isentropic,[14] the work of compressing the cooling air cannot all be recovered by expansion through the turbine. There are a multitude of ways in which a thermally driven morphing structure could control cooling flow, but the general idea would be to use the morphing structure as a combined aerodynamic control surface and thermostat, which varies its geometry to admit additional cooling air as needed.

**Core Exhaust Chevrons**

Consider Fig. 50. One can see that chevrons are not only built into the fan nozzle (in white), but also in the core exhaust nozzle. No attempts at core nozzle morphing have been tried, to the author's knowledge, however this technology would be an appealing application of high-temperature thermal bimorphs. Core exhaust temperatures are typically $300 - 600°C$, depending on engine operating state. These temperatures are out of reach of SMA-based actuators, however thermal bimorphs may still survive in such an environment. Present work with MMC bimorphs suggest that such a laminate would be hard-pressed to operate above $500°C$, however these efforts are of course "first iteration" quality. Perhaps the use of more different materials or more cleverly designed laminates (see Section 7.3) could yield a solution.

# 7 Future Research Opportunities

Several new research opportunities were identified in the course of this work. This section describes the three of the most potent to pursue.

[14] Isentropic compression and expansion denotes a condition of constant entropy. In this scenario, the external work required to compress a volume of gas can be entirely recovered by expansion of that gas. Real-world compression and expansion in turbomachinery is not perfectly isentropic, and thus some work is lost to entropy, manifested by heat.



**Distribution A: Approved for public release; distribution unlimited.**

## 7.1 Collapsible Stiffeners for Lockable Morphing Structures

Morphing structures must undergo large displacements, however doing so while maintaining an acceptably stiff structure has proven to be a major obstacle to adoption. A stiffener which could vary its second moment of area when attached to a panel, would allow the panel to undergo large displacements, then lock into a particular shape as desired. The basic idea, shown in Fig. 53, is to choose a stiffener shape which is capable of collapsing towards the neutral axis of the structure. Stiffener collapse can be driven passively by brazier loads arising from externally forced panel curvature, or may be thermally triggered by constructing the stiffener from a bimorph laminate which flattens with temperature change. Likewise, temperature change could also be used to trigger stiffener deployment.

One advantage of collapsible stiffeners over previous nonlinear concepts such as tape-measure-like beams and bistable shells is that they can be joined to the inner skin of an aerodynamic surface, and thus, are able to lend nonlinear behaviour to airfoil skins without requiring changes to the outer aerodynamic shape. Additionally, the ability to arrange the stiffeners in a repeating pattern allows panels of arbitrary shape and size to be given geometrically nonlinear properties, whereas the multistable structures described previously in this document were sensitive to planform size effects.

A simple metallic demonstrator model was fabricated from tape-measure sections riveted to an aluminium skin. As shown in Fig. 53, this panel could become bistable with suitable pre-curving of the skin by plastic deformation.



**Distribution A: Approved for public release; distribution unlimited.**

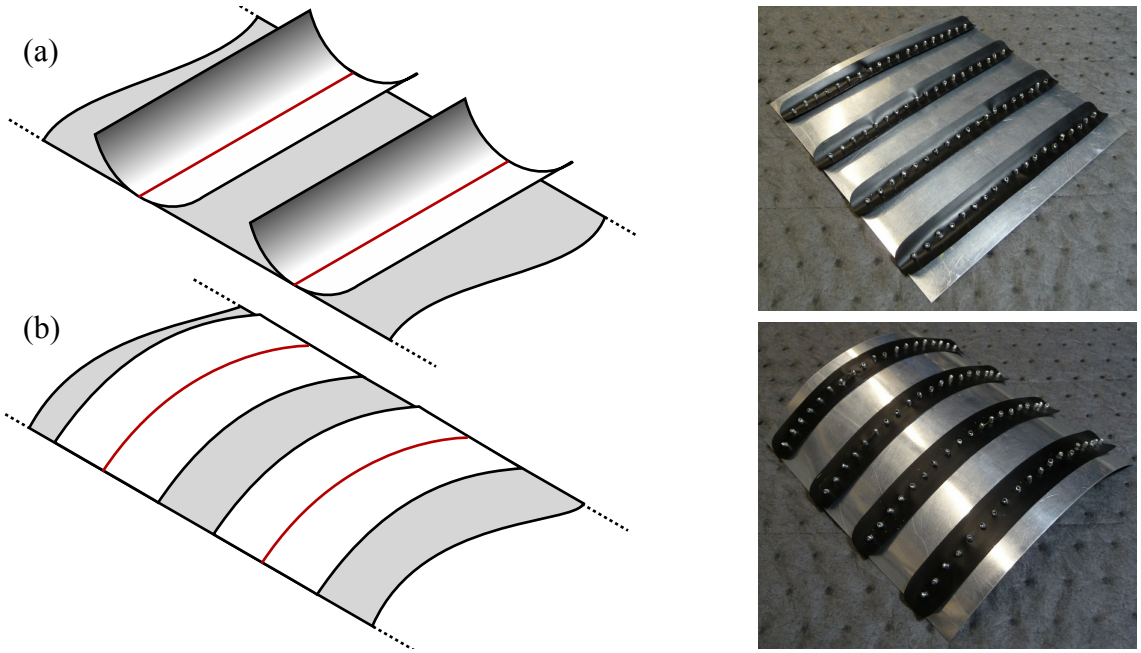



Figure 53: Collapsible stiffeners joined to a skin. The right-side images show a bistable demonstrator model.
a) Stiffeners in their deployed state stiffen the skin.
b) With the stiffeners collapsed, the skin is free to develop curvature.

## 7.2 Geometrically Linear Behaviour For Arbitrary Planforms Despite Large Displacements

In Section 2.4, the potential advantages of using shallow angle-ply fibre orientations in fibre-metal bimorphs were discussed. This brief theoretical study showed that there was potential to improve upon the performance and durability of unidirectional fibre-metal bimorphs. In addition to improvements in weight-specific thermal moments, the proper selection of fibre orientations could yield a bimorph which develops thermal moments in one direction only. This feature has yet to be demonstrated in literature, and to the author's knowledge, represents a novel development in bimorph actuation. As shown in Fig. 54, the main result of applying moments along one direction only is that large bimorphs of arbitrary planform size and shape can be made to develop uniform curvature in a linear manner across all temperatures for which the material behaves linearly. This behaviour stands in contrast to current bimorphs, which apply bidirectional moments to varying degrees. These bidirectional moments seek to generate bidirectional curvature. If the bimorph is initially a developable



**Distribution A: Approved for public release; distribution unlimited.**

surface, then at least one of the curvatures under development is geometrically constrained, due to the fact that thin plates and shells tend to conserve their initial Gaussian curvature. This constraint of curvature generation not only leads to a build-up of potentially detrimental internal stresses, but also induces a geometrically nonlinear structural response to thermal loads.

While the present work has focused on exploiting this nonlinearity, there are certainly cases where the designer would want a completely linear response. With current bimorphs, this behaviour can only be achieved by shaping the bimorph into a long, thin strip, such that bend-stretch coupling is all but eliminated. Supposing the design called for a planform shape that was not strip-shaped, a linear response could only be produced by ensuring that the bimorph developed thermal curvature in one direction only, which can be obtained with proper matching of an angle-ply low-expansion layer to a metallic high-expansion layer. It is possible that the correct matching condition occurs when the CTEs of each layer are matched in one direction, however Poisson coupling, i.e., the tendency to generate anticlastic curvature, may require a small orthogonal thermal moment to cancel the anticlastic curvature.

In general, achieving a linear curvature response to any strain-based loads, thermal or otherwise, boils down to ensuring that the membrane strains remain completely compatible with the curvatures. This hypothesis raises the question of whether one can design a doubly curved surface which still maintains a linear response to internal moments over large displacements. A brief thought experiment may give us some clues. Suppose we take a tennis ball and cut it in half. Now pinch the hemisphere by the edges, deforming the shape into an ellipsoidal dome as illustrated in Fig. 54. If we approximate the surface as inextensible, the original Gaussian curvature of the hemisphere is conserved, thus the increase in curvature along one principle axis is met with a decrease in curvature along the perpendicular axis, such that the product of the two curvatures is conserved. Because there is no change in Gaussian curvature, strain energy will only be stored in bending. From this observation, we may hypothesise that a linear response to internal moments would be achieved if the internal moments were not only nonzero, but also of opposite sign between the two principle directions, such that they acted in the same sign and relative magnitude as the principle curvatures. Whether this behaviour has practical applications is not known, but it represents an unexplored aspect of the field of morphing structures.



**Distribution A: Approved for public release; distribution unlimited.**

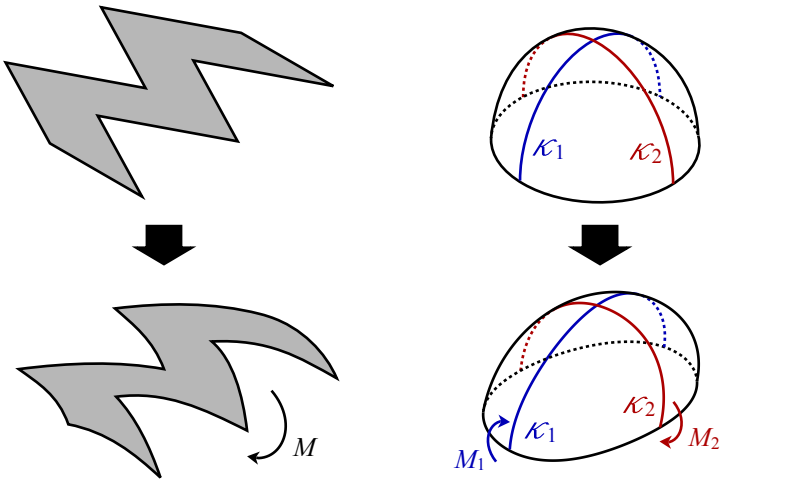



Figure 54: Two hypothesised methods of achieving a linear curvature response to internal moments for both developable and doubly curved surfaces.

## 7.3 Beyond Bimorphs: More Efficient Thermal Morphing Structures

A thermal bimorph may be a simple and elegant concept, however it actually does not make very efficient use of its constituent material's thermal stresses. Consider the bimorph in Fig. 55, and its associated thermal stresses $\sigma_{\mathrm{T}}$. The thermal moment contributed by each infinitesimal layer-wise slice is the product of the thermal stress and distance from the neutral axis. For the same reason that beams are more structurally efficient if their material is removed from the neutral axis, a thermal morphing laminate makes more efficient use of its thermal stress if the high and low expansion layers are separated using some core layer. This separation of high and low CTE layers could be facilitated by the trimorph concept, in which the core layer is made of an intermediate CTE material. This approach also reduces the interfacial stresses between layers, which scale in proportion to the CTE mismatch at the interface. Alternately, the core could be constructed from a predominately hollow multicellular structure such as a honeycomb or a truss-core. The goal of such a core is to transmit shear loads between the high and low expansion layers while being as lightweight as possible. Although this concept probably represents a very structurally efficient solution,



**Distribution A: Approved for public release; distribution unlimited.**

there are certainly greater manufacturing challenges in this design compared to a bimorph or trimorph.

One further possibility is a functionally graded laminate, which features a linearly varying CTE between top and bottom surfaces. The main advantage of this concept is that it has theoretically zero interfacial stresses, as the CTE mismatch at each layer-wise slice is infinitesimally small. Since these interfacial stresses are responsible for delamination as observed in Section 4.2.2, their absence in this case bodes well for the durability of this laminate. Fabrication of such a laminate could be accomplished by smoothly varying the fibre-volume fraction of a composite in the thickness direction. Achieving this volume fraction variation would actually be a relatively straightforward procedure with titanium-matrix composite and thermoplastic-matrix composite fabrication methods, which allow fibre locations and volume fractions to be mostly "locked in" during layup due to the fact that the matrix remains in the semi-solid state throughout the consolidation process. A CTE gradient could also be achieved by varying the proportions of fibre types, e.g. carbon vs. glass, through the thickness.

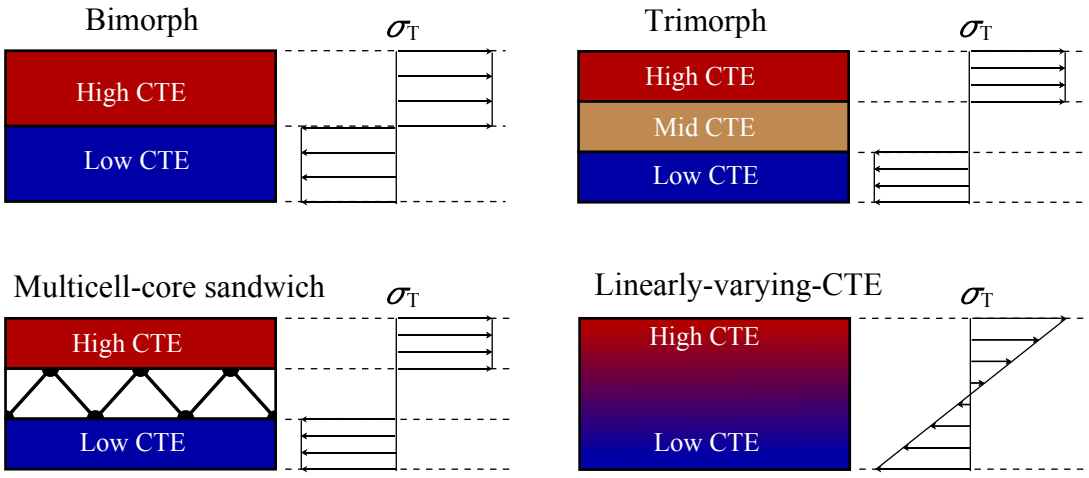



Figure 55: A bimorph generates much of its thermal stress $\sigma_T$ near the neutral axis, however there are other thermal morphing laminates that make more efficient use of their thermal stresses. A trimorph is a three-layer laminate in which the middle layer possesses an intermediate CTE. A sandwich laminate is a variation of the trimorph, in which the middle layer is a hollow multicellular core capable of transmitting shear loads between the high and low CTE layers. Finally, a functionally graded layer with linearly varying CTE is also illustrated.



**Distribution A: Approved for public release; distribution unlimited.**

# 8 Dissemination

Work carried out under this contract contributed to the following research outputs.

**PhD Thesis**

E. Eckstein. *The Nonlinear Thermostructural Behaviour of Composite Bimorphs at Elevated Temperatures.* PhD Thesis submitted and pending examination board review. University of Bristol, March 2016. *Available upon request.*

**Conference Publications**

E. Eckstein, E. Lamacchia, A. Pirrera, P.M. Weaver. *Thermally-driven snap-through and multistability using laminated fibre-metal shells.* 16th European Conference on Composite Materials, June 2014.

E. Eckstein, A. Pirrera, P.M. Weaver. *Thermally Driven Morphing with Hybrid Laminates and Metal Matrix Composites.* 56th AIAA/ASCE/AHS/ASC Structures, Structural Dynamics, and Materials Conference, Jan 2015.

E. Eckstein, M. Halbig, P.M. Weaver. *Thermally Driven Morphing with High Temperature Composites.* 57th AIAA/ASCE/AHS/ASC Structures, Structural Dynamics, and Materials Conference, Jan 2016.

**Journal Publications**

E. Eckstein, A. Pirrera, P.M. Weaver *Thermally Driven Morphing and Snap-Through Behavior of Hybrid Laminate Shells.* Accepted for publication in AIAA Journal.

**Awards**

Jefferson Goblet Award for best student paper, 7th AIAA/ASCE/AHS/ASC Structures, Structural Dynamics, and Materials Conference, Jan 2016.

**Other Outputs**

*Thermally-Actuated, high temperature morphing composites.* Window on Science visit to WPAFB, June 4th, 2015. WPAFB contact: Craig Pryzbyla.

*Thermally-Actuated, high temperature morphing composites.* Presentation delivered to NASA Glenn Research Center, Materials Directorate, June 11th, 2015.



**Distribution A: Approved for public release; distribution unlimited.**

*INCPAMM: Initially Curved Plate Multistability Modelling Package.* A coded implementation of the multistability model described in Section 3. Available online via dx.doi.org/10.5523/bris.aqgn00zib77n10kxh192ozkc0. November 2014.



**Distribution A: Approved for public release; distribution unlimited.**

# References


[1] Dennis Culley, Sanjay Garg, S. J. Hiller, Wolfgang Horn, Aditya Kumar, H. K. Mathews, Hany Moustapha, Hugo Pfoertner, Taylor Rosenfeld, Pavol Rybarik, Klaus Schadow, Ion Stiharu, Daniel E. Viassolo, and John Webster. More Intelligent Gas Turbine Engines. Technical Report RTO-TR-AVT-128, NATO RTO, April 2009.

[2] Carolyn R. Mercer, William J. Haller, and Michael T. Tong. Adaptive Engine Technologies for Aviation CO2 Emissions Reduction. Technical Report NASA/TM-2006-214392, August 2006.

[3] Thomas Fox. Actuation Challanges of Future Aero Engines. In *Smart Actuation Applications Conference*. Institution of Mechanical Engineers, September 2014.

[4] A nozzle on a McDonnell Douglas F-15 Eagle at the Evergreen Aviation and Space Museum in McMinville, OR. *Photo available at* http://imgur.com/QGtxD4a.

[5] Gary Brossett. P&W J-58 VIGV. *Photo available at* www.enginehistory.org/G&jJBrossett/Hill%20Field/P&w%20j-58%20vigv.jpg, 2003.

[6] Sanjay Acharya. General Electric J85. *Photo available at* https://en.wikipedia.org/w/index.php?title=General_Electric_J85&oldid=709702364, March 2016.

[7] Scott B. Lattime and Bruce M. Steinetz. High-pressure-turbine clearance control systems: current practices and future directions. *Journal of Propulsion and Power*, 20(2):302–311, 2004.

[8] J. E. Huber, N. A. Fleck, and M. F. Ashby. The selection of mechanical actuators based on performance indices. *Proceedings of the Royal Society of London. Series A: Mathematical, Physical and Engineering Sciences*, 453(1965):2185–2205, October 1997.

[9] E. H Mansfield. Bending, Buckling and Curling of a Heated Elliptical Plate. *Proceedings of the Royal Society of London. Series A. Mathematical and Physical Sciences*, 288(1414):396–417, November 1965.

[10] Marco Gigliotti, Michael R. Wisnom, and Kevin D. Potter. Loss of bifurcation and multiple shapes of thin [0/90] unsymmetric composite plates subject to thermal stress. *Composites Science and Technology*, 64(1):109–128, January 2004.

[11] S. Timoshenko. Analysis of bi-metal thermostats. *J. Opt. Soc. Am*, 11(3), 1925.




**Distribution A: Approved for public release; distribution unlimited.**

[12] E. H Mansfield. Bending, Buckling and Curling of a Heated Thin Plate. *Proceedings of the Royal Society of London. Series A. Mathematical and Physical Sciences*, 268(1334):316–327, July 1962.

[13] Michael Hyer. Some Observations on the Cured Shape of Thin Unsymmetric Laminates. *Journal of Composite Materials*, 15(2):175 –194, March 1981.

[14] S. Prasanna and S.M. Spearing. Materials Selection and Design of Microelectrothermal Bimaterial Actuators. *Journal of Microelectromechanical Systems*, 16(2):248–259, 2007.

[15] M. F. Ashby. *Materials Selection in Mechanical Design*. Butterworth-Heinemann, 4th edition, 2011.

[16] J. C. Halpin and N. J. Pagano. Consequences of environmentally induced dilatation in solids. Technical Report AD-701-725, United States Air Force Research Laboratory, December 1969.

[17] M. W. Hyer and P. C. Bhavani. Suppression of anticlastic curvature in isotropic and composite plates. *International Journal of Solids and Structures*, 20(6):553–570, 1984.

[18] L. G. Brazier. On the flexure of thin cylindrical shells and other thin sections. *Proceedings of the Royal Society of London. Series A*, 116(773):104–114, 1927.

[19] Libo Ren, Azar Parvizi-Majidi, and Zhengneng Li. Cured Shape of Cross-Ply Composite Thin Shells. *Journal of Composite Materials*, 37(20):1801–1820, October 2003.

[20] S. Pellegrino. Large retractable appendages in spacecraft. *Journal of Spacecraft and Rockets*, 32(6):1006–1014, 1995.

[21] E. Eckstein, A. Pirrera, and P.M. Weaver. Multi-mode morphing using initially curved composite plates. *Composite Structures*, 109:240–245, March 2014.

[22] Michael Hyer. Calculations of the Room-Temperature Shapes of Unsymmetric Laminates. *J Composite Materials*, 15:296, January 1981.

[23] Amancio Fernandes, Corrado Maurini, and Stefano Vidoli. Multiparameter actuation for shape control of bistable composite plates. *International Journal of Solids and Structures*, 47(10):1449–1458, May 2010.

[24] Marie-Laure Dano and Michael W. Hyer. Thermally-induced deformation behavior of unsymmetric laminates. *International Journal of Solids and Structures*, 35(17):2101–2120, June 1998.



**Distribution A: Approved for public release; distribution unlimited.**

[25] A. Pirrera, D. Avitabile, and P. M. Weaver. Bistable plates for morphing structures: A refined analytical approach with high-order polynomials. *International Journal of Solids and Structures*, 47(25-26):3412–3425, December 2010.

[26] A. Pirrera, D. Avitabile, and P. M. Weaver. On the thermally induced bistability of composite cylindrical shells for morphing structures. *International Journal of Solids and Structures*, 49(5):685–700, March 2012.

[27] Stephen Daynes and Paul M. Weaver. Analysis of unsymmetric CFRP-metal hybrid laminates for use in adaptive structures. *Composites Part A: Applied Science and Manufacturing*, 41(11):1712–1718, November 2010.

[28] D. W. Radford and T. S. Rennick. Separating Sources of Manufacturing Distortion in Laminated Composites. *Journal of Reinforced Plastics and Composites*, 19(8):621–641, May 2000.

[29] Keith A. Seffen and Corrado Maurini. Growth and shape control of disks by bending and extension. *Journal of the Mechanics and Physics of Solids*, 61(1):190–204, January 2013.

[30] S. Vidoli and C. Maurini. Tristability of thin orthotropic shells with uniform initial curvature. *Proceedings of the Royal Society of London A: Mathematical, Physical and Engineering Sciences*, 464(2099):2949–2966, November 2008.

[31] Craig S. Collier. Stiffness, thermal expansion, and thermal bending formulation of stiffened, fiber-reinforced composite panels. In *34th AIAA/ASCE/AHS/ASC Structures, Structural Dynamics, and Materials Conference.*, April 1993.

[32] *ESDU Metallic Materials Data Handbook*. Supplement 47. IHS ESDU, July 2012.

[33] E. Lamacchia, A. Pirrera, I. V. Chenchiah, and P. M. Weaver. Morphing shell structures: A generalised modelling approach. *Composite Structures*, 131:1017–1027, November 2015.

[34] *Kanthal Thermostatic Bimetal Handbook*. Kanthal AB, 2012.

[35] P. D. Mangalgiri. Polymer-matrix composites for high-temperature applications. *Defence Science Journal*, 55(2):175–193, 2005.

[36] T. W. Clyne and P. J. Withers. *An Introduction to Metal Matrix Composites*. Cambridge University Press, June 1993.



**Distribution A: Approved for public release; distribution unlimited.**

[37] J. G. Robertson. Manufacture and Properties of Sigma Fibre Reinforced Titanium. Technical Report AGARD-R-796, NATO Advisory Group for Aerospace Reserach and Development, February 1994.

[38] M. P. Thomas and M. R. Winstone. Effect of the angle between fibres and tensile axis on static properties of unidirectional reinforced titanium MMC. In *8th European Conference on Composite Materials*, 1998.

[39] Gerhard Welsch, Rodney Boyer, and E. W. Collings. *Materials Properties Handbook: Titanium Alloys*. ASM International, December 1993.

[40] P. Feillard. The high temperature behaviour of long fibre reinforced titanium under transverse loading. *Acta Materialia*, 44(2):643–656, February 1996.

[41] M Ghosh and S Chatterjee. Characterization of transition joints of commercially pure titanium to 304 stainless steel. *Materials Characterization*, 48(5):393–399, July 2002.

[42] Swarup K. Ghosh and S. Chatterjee. On the Direct Diffusion Bonding of Titanium Alloy to Stainless Steel. *Materials and Manufacturing Processes*, 25(11):1317–1323, 2010.

[43] S. Kundu, M. Ghosh, A. Laik, K. Bhanumurthy, G. B. Kale, and S. Chatterjee. Diffusion bonding of commercially pure titanium to 304 stainless steel using copper interlayer. *Materials Science and Engineering: A*, 407(1–2):154–160, October 2005.

[44] Milton S. Hess. The End Problem for a Laminated Elastic Strip: II Differential Expansion Stresses. *Journal of Composite Materials*, 3(4):630–641, October 1969.

[45] Walter Krenkel, editor. *Ceramic Matrix Composites: Fiber Reinforced Ceramics and Their Applications*. Wiley VCH, Weinheim, 1st edition, May 2008.

[46] Email conversation with Dr. Thomas Behnisch, TU Dresden. *Available upon request to author*, February 2014.

[47] David Glass. Ceramic Matrix Composite (CMC) Thermal Protection Systems (TPS) and Hot Structures for Hypersonic Vehicles. In *15th AIAA International Space Planes and Hypersonic Systems and Technologies Conference*. American Institute of Aeronautics and Astronautics, April 2008.

[48] Randy Lee. Carbon and Ceramic Matrix Composites for Space Telescope Platforms, NASA Internal Communications. *Available online at* http://materialchemistry.com/DreamHC/Download/CMC%20Telescope%20Memo1.pdf, August 2011.



**Distribution A: Approved for public release; distribution unlimited.**

[49] Ke Jian, Z. H. Chen, Q. S. Ma, H. F. Hu, and W. W. Zheng. Processing and properties of 2d-Cf/SiC composites incorporating SiC fillers. *Materials Science and Engineering: A*, 408(1):330–335, November 2005.

[50] C. H. Hsueh and A. G. Evans. Residual Stresses in Metal/Ceramic Bonded Strips. *Journal of the American Ceramic Society*, 68(5):241–248, May 1985.

[51] M. Singh, Tarah Shpargel, Gregory N. Morscher, Michael H. Halbig, and Rajiv Asthana. Robust Joining and Integration Technologies for Advanced Metallic, Ceramic, and Composite Systems. In *30th International Conference on Advanced Ceramics and Composites*, Cocoa Beach, FL, United States, January 2006.

[52] Eric Chau. *A Comparative study of Joining Methods for a SMART Aerospace Application*. PhD thesis, Cranfield University School of Applied Sciences, April 2007.

[53] *Metals Handbook*. American Society for Metals, 9th edition, 1980.

[54] Eric Eckstein. INCPAMM: Initially Curved Plate Multistability Model. *Available via* dx.doi.org/10.5523/bris.aqgn00zib77n10kxh192ozkc0, November 2014.

[55] James Bridges, Mark Wernet, and Cliff Brown. Control of Jet Noise Through Mixing Enhancement. Technical Report NASA/TM-2003-212335, National Aeronautics and Space Administration, June 2003.

[56] Norman Schaeffler, Timothy Hepner, Gregory Jones, and Michael Kegerise. Overview of Active Flow Control Actuator Development at NASA Langley Research Center. In *1st Flow Control Conference*. American Institute of Aeronautics and Astronautics, June 2002.

[57] V. Pott, H. Cohen, R. Nathanael, J. Jeon, E Alon, and T.J.K. Liu. Mechanical Computing Redux: Relays for Integrated Circuit Applications. *Proceedings of the IEEE*, 98(12):2076–2094, December 2010.

[58] Carl R. Peterson. *Mechanics and Thermodynamics of Propulsion*. Addison-Wesley, 1970.

[59] David H. Silvern and William R. Slivka. Analytical investigation of turbines with adjustable stator blades and effect of these turbines on jet-engine performance. Technical Report NACA-RM-E50E05, July 1950.

[60] Robert E. English and Richard H. Cavicchi. One-dimensional analysis of choked-flow turbines. Technical Report NACA-TR-1127, Lewis Flight Propulsion Laboratory, National Advisory Committee for Aeronautics, 1952.



**Distribution A: Approved for public release; distribution unlimited.**